Coupled Electrochemo-Mechanical Phenomena at the Anode/Electrolyte Interface in Solid-State Batteries

by

Michael J. Wang

A dissertation submitted in partial fulfillment
of the requirements for the degree of
Doctor of Philosophy
(Materials Science and Engineering)
in the University of Michigan
2020

Doctoral Committee:

Associate Professor Jeff S. Sakamoto, Chair
Associate Professor Neil P. Dasgupta
Professor Katsuyo S. Thornton
Professor Michael Thouless

Michael J. Wang

micwan@umich.edu

ORCID iD: 0000-0002-9980-3828

Dedication

This dissertation is dedicated to my family, my biggest supporters.

Acknowledgements

First and foremost, I would like to sincerely thank my advisor, Professor Jeff Sakamoto, for the constant support, enthusiasm, and mentorship over the past few years. It has been an absolute privilege to learn from you and I am deeply appreciative of your non-stop commitment to my personal and professional success. I would also like to thank all of the members of the Sakamoto group, both past and present, not only for being a great community of researchers, but also for the many great memories both in and out of the lab. In particular, I would like to thank Regina, Arushi, and Angelica for being endless sources of advice, encouragement, and fun times, Al and Nate for all of their words of wisdom, and finally Rishav and Rita for all of their hard-work and for being amazing mentees.

I would also like to thank my committee members for all of their insight and feedback. I would like to especially thank Professor Neil Dasgupta, who has acted as my secondary mentor here in Michigan, providing valuable and unique insights on my work and constantly supporting my development as a researcher. In addition, I would like to extend my gratitude to all of the people whom I have had the privilege of collaborating with and learning from, including: Dr. Jeff Wolfenstine, Dr. Marie-Claude Bay, Dr. Corsin Battaglia, Professor Paul Albertus, Eric Carmona, Dr. Eric Kazyak, and Dr. Tim Chambers.

I would also like to extend my deep appreciation for those who kept me grounded outside of the lab and were crucial to shaping my Michigan experience. Huge shout-outs to Vincent, Eric, Nick, Reuben, Jae, George, Emma, Brian, and Erica.

There are many others who have greatly impacted my time here in Michigan who I have not listed here, but to those people, thank you as well.

Finally, I would like to thank my parents and my sister for their unconditional support in all of my endeavors.

Table of Contents

Dedication ii

Acknowledgements iii

List of Tables x

List of Figures xi

Abstract xxi

Chapter 1 Introduction 1

  1.1 Fundamentals of Battery Operation 2

  1.2 Lithium-Ion Batteries 5

  1.3 Solid-State Batteries 5

    1.3.1 Solid-State Electrolytes 7

      1.3.1.1 High total ionic conductivity 8

      1.3.1.2 Electrochemical and mechanical stability 8

      1.3.1.3 Low electronic conductivity 9

      1.3.1.4 Operation within a wide temperature range 9

      1.3.1.5 Low-cost manufacturability at relevant thicknesses (~10-100 µm to compete with traditional separators) 9

      1.3.1.6 The electrolyte and manufacturing process must be environmentally benign 10

    1.3.2 Alkali Metal Anodes 14

  1.4 Challenges Facing Solid-State Batteries 16

Chapter 2 Experimental Methods 20

  2.1 Electrolyte Synthesis and Processing 20

2.2 Assembly of Symmetric Cells 23

2.3 Electrochemical Impedance Spectroscopy 25

Chapter 3 Effects of Temperature on Alkali Metal Plating 28

3.1 Temperature Dependent Flux Balance of the Li/$Li_7La_3Zr_2O_{12}$ Interface 30

3.1.1 Introduction 30

3.1.2 Experimental 32

3.1.2.1 LLZO synthesis and cell assembly 32

3.1.2.2 Electrochemical characterization 33

3.1.3 Results and Discussion 34

3.1.3.1 Materials and electrochemical characterization 34

3.1.3.2 Relationship between CCD and temperature 38

3.1.3.3 Comparison of reported CCDs 42

3.1.4 Conclusions 44

3.2 Sodium Plating from Na-β″-Alumina Ceramics at Room Temperature, Paving the Way for Fast-Charging All-Solid-State Batteries 45

3.2.1 Introduction 45

3.2.2 Experimental Section 46

3.2.3 Results and Discussion 48

3.2.3.1 Impact of heat treatment temperature on interfacial resistance and interface chemistry 48

3.2.3.2 Temperature-dependent transport properties 53

3.2.3.3 Critical current densities in Na-β”-alumina ceramics as function of charge and R_{int} 54

3.2.3.4 Temperature-dependent CCD and comparison with literature 58

3.2.4 Conclusion 61

3.3 A Comparison of the Mechanics and Electroplating Behavior of Li and Na at the Electrode/Electrolyte Interface 62

3.3.1 Introduction 62

3.3.2 Mechanisms of Mode I Fracture 65

3.3.2.1 Conditions for fracture of the ceramic electrolyte 65

3.3.2.2 Stress distribution within the surface defect 68

3.3.2.3 Model and assumptions 71

3.3.3 Results & Discussion 77

3.3.3.1 Comparison between the theoretical and experimental CCDs 77

3.3.3.2 Implications for solid-state battery design 80

3.3.4 Conclusions 81

Chapter 4 Effects of External Pressure on Alkali Metal Stripping 83

4.1 Characterizing the Li-Solid-Electrolyte Interface Dynamics as a Function of Stack Pressure and Current Density 84

4.1.1 Introduction 84

4.1.2 Experimental 87

4.1.2.1 Materials synthesis and cell assembly 87

4.1.2.2 Mechanical testing 88

4.1.2.3 Electrochemical testing 89

4.1.3 Results & Discussion 89

4.1.3.1 Galvanostatic cycling under dynamic stack pressure conditions 89

4.1.3.2 Reversibility of void-induced polarization 92

4.1.3.3 Decoupling Li stripping from plating 94

4.1.3.4 Electrochemical void formation mechanism and prevention 97

4.1.4 Conclusion 105

4.2 Investigating the Effects of Stack Pressure on the Na-Metal/Solid-Electrolyte Interface 106

4.2.1 Introduction 106

4.2.2 Experimental Methods.. 108

4.2.2.1 Cell assembly 108

4.2.2.2 Mechanical and electrochemical methods 109

4.2.3 Results & Discussion.. 110

4.2.3.1 Potential response to decreasing stack pressure... 110

4.2.3.2 Void closure and reversibility at low stack pressure 111

4.2.3.3 Effects and reversibility at high stack pressure.. 113

4.2.3.4 Identifying interface morphology at the anode/electrolyte interface under stripping currents 115

4.2.3.5 Implications for analyzing solid-state batteries 121

4.2.4 Conclusions 123

Chapter 5 Li Electrodeposition at a Solid-Solid Interface 125

5.1 Enabling “Li-free” Manufacturing of Pure Li Metal Solid-State Batteries Through *in situ* Plating... 126

5.1.1 Introduction 126

5.1.2 Methods 129

5.1.2.1 Cell assembly 129

5.1.2.2 Electrochemical methods 130

5.1.2.3 Materials characterization.. 131

5.1.3 Results & Discussion.. 133

5.1.3.1 Demonstration of in situ plating of Li.. 133

5.1.3.2 Mechanics and nucleation of Li at the CC/LLZO interface 138

5.1.3.3 Performance of an in situ plated Li metal anode 148

5.1.4 Conclusion.. 153

Chapter 6 Conclusions and Future Work.. 155

6.1 Summary 155

6.2 Future Directions 158

6.2.1 Modeling of Electrochemo-Mechanical Phenomena for Optimizing Battery Design 158

6.2.2 Alkali Metal Stripping and Plating Behavior at the Thin Film Scale 159

6.2.3 Effects of Prolonged Cycling on Interface Morphology 161

6.2.4 Effects of Plating Current Density and Relaxation Times on Interface Evolution 162

6.3 Conclusions 164

Bibliography 166

List of Tables

Table 1.1: An overview of common solid-electrolyte materials in the literature[6–13] 11

Table 3.1: Fitting results of room temperature interfacial resistance (R_{int}) and capacitance (CPE_{int}) for the various heat-treatment (HT) conditions.. 50

Table 3.2: XPS quantification data for the Na-β"-alumina samples before and after heat treatment at Ar atmosphere at 400, 700 and 900 °C. 51

Table 3.3: List of electrolyte fracture properties for LLZO (as reported by Han *et al.*[79]) and for NBA (as reported by Bay *et al.*[80]) 67

Table 3.4: List of mechanical and electrochemical properties and their values for the Li/LLZO and Na/NBA system (*indicates value calculated from reference data). 76

Table 4.1: List of parameters and values for calculating strain rates in Figure 4.10 101

List of Figures

Figure 1.1: Schematic of an electrochemical cell while a) discharging and b) charging. Adapted with permission from Ref. [4]. 3

Figure 1.2: Schematic of a Li-ion battery, solid-state battery, and a Li metal solid-state battery. Adapted with permission from Ref. [100]. 7

Figure 1.3: Schematic of the morphological changes that occur during cycling at the alkali metal electrode/solid-electrolyte interface. 18

Figure 2.1: Processing of solid-electrolyte materials beginning from solid-state synthesis to densification. 21

Figure 2.2: Assembly of an electrochemical cell consisting of a ceramic solid-electrolyte and alkali metal electrodes 24

Figure 2.3: Relevant equivalent circuit models and corresponding Nyquist plots. a) Equivalent circuit model for a polycrystalline solid-electrolyte with blocking electrodes. b) Equivalent circuit model for a polycrystalline solid-electrolyte with non-blocking electrodes. c) A representative Nyquist plot for the circuit model in (a). d) A representative Nyquist plot for the circuit model in (b) 26

Figure 3.1: XRD spectra for the hot-pressed LLZO pellet. A reference for cubic garnet is provided. 34

Figure 3.2: Conductivity as a function of a temperature calculated from the bulk, grain boundary, and interface resistances of the Li/LLZO/Li cell. The resistance value of each component was obtained by equivalent circuit modeling of the measured Nyquist plot at each temperature. 35

Figure 3.3: a) Representative potential response of a Li/LLZO/Li cell undergoing a CCD measurement and b) representative EIS spectra before and after the shorting condition. c) Potential response near the CCD. Arrows indicate the drop in potential corresponding to the short circuit and the erratic behavior following the short. d) Polarization of the cell tends to increase as the magnitude of the applied current increases. 36

Figure 3.4: a) CCD as a function of temperature and b) Arrhenius plot of CCD. Reported CCDs from the literature are plotted for comparison[4,6–9]. c) Averages and standard deviations for CCDs as a function of temperature. 38

Figure 3.5: The calculated diffusivity of Li in LLZO calculated from the Nernst-Einstein equation. The self diffusivity of Li is shown for comparison[51]. 40

Figure 3.6: a) Schematic of Li^+ plating in a vacant surface site at the Li/LLZO interface. b) Near the CCD, diffusivity is insufficiently fast enough to maintain an adequate number of vacant sites at the surface c) At high current densities, Li^+ is forced to plate on already occupied sites leading to “hot-spots” with increased electron density. d) Hydrostatic compression in the Li metal as suggested by Masias *et al.*[52] may impede Li transport and expedite “hot-spot” formation....... 42

Figure 3.7 Impact of heat-treatment (HT) temperature on interfacial resistance at room temperature. (a) Schematic of the symmetric Na/Na-β”-alumina/Na cell and equivalent circuit for fitting the impedance spectra. (b) Representative Nyquist plots for the different heat-treatment temperatures. Markers represent experimental data and lines represent the fitted data. (c) Interfacial resistance as a function of heat-treatment temperature. 49

Figure 3.8: XPS analysis of Na-β"-alumina surfaces before and after heat treatment. XPS spectra of C 1s, O 1s and Al 2p-Na 2s core levels of the Na-β"-alumina before heat treatment (a-c), and after heat treatment under argon atmosphere at 400 °C (d-f), at 700 °C (g-i), and at 900 °C (j-l), respectively. Summary of surface chemical composition, estimated by XPS, for all Na-β"-alumina samples (m). 50

Figure 3.9: (a) Representative Nyquist plots as a function of temperature on samples heat treated at 900 °C. Temperature-dependent (b) interfacial resistance and ionic conductivity, (c) electronic conductivity, and (d) ionic transference number t plotted as 1-t for readability.......................... 54

Figure 3.10: (a) Representative potential response of a Na/Na-β”-alumina/Na cell undergoing CCD measurement at room temperature and charge of 0.25 mAh cm^{-2} per half cycle. (b) Nyquist plots before and after short-circuit. Closer view on the potential response during CCD measurement (c) at low current densities (d) at medium current densities, and (e) close to short circuit, showing an increase of the polarization... 56

Figure 3.11: Representative potential responses of Na/Na-β”-alumina/Na cells undergoing CCD measurements at total transferred charge Q per half cycle of (a) Q = 0.25 mAh cm^{-2} and (b) Q = 3 mAh cm^{-2} for Na-β”-alumina samples heat treated at 900 °C (while the potential response of the two last cycles before failure reached a limit of 4.5 V, the maximum value of the y axis scale bar is 1 V for better readability). (c) CCD as a function of interfacial resistance. 58

Figure 3.12: Temperature-dependent CCD and comparison with literature (a) in Arrhenius representation (b) as a function of homologous temperature ($T/T_{melting}$). 61

Figure 3.13: Temperature-dependent diffusivity of Na^+ in Na-β”-alumina and Na self-diffusivity compared to the diffusivity of Li^+ in LLZO and Li self-diffusivity (see manuscript for details). 61

Figure 3.14: Illustration of the electrodeposition of Li at a surface flaw at the Li/LLZO interface under a stack pressure of P_0. It is assumed that the Li^+ are plated at the interface at a current density of i_0 near a surface flaw with length L and radius r_0. In order to accommodate the continued deposition of Li, the existing Li within the flaw must flow into the bulk with a velocity u.. 66

Figure 3.15: Illustration of the physical processes that occur during Li electrodeposition within the surface flaw. a) Li is electrodeposited at the Li/LLZO boundary (illustrated in red), exerting a pressure on the pre-existing Li within the flaw. The pressure induces flow of the Li out of the flaw and exerts a hydrostatic pressure on the walls of the flaw. b) Modeling the deformation of Li as creeping flow, the velocity profile of Li within the flaw can be determined from the Li^+ flux in the electrolyte. As proposed by Barroso-Luque *et al.*[77], the flux of Li^+ in the electrolyte is affected by electro-plastic effects. Based on this hypothesis, at regions of low pressures c) electrodeposition is dominated by electrostatic gradients. At regions of high pressure d) the electrochemical potential is reduced which redirects ion flux toward areas of lower pressure.... 70

Figure 3.16: The dependence of the viscosity on the strain-rate for Li and Na metal at room temperature. The viscosities are calculated from Equation 3.17, using stress and strain-rate data taken from LePage *et al.*[76] and Wang *et al.*[83]... 74

Figure 3.17: The resulting stress intensity factor (SIF) as a function of crack tip radius. a) The stress intensity factor resulting from both the electrostatic and the electroplastic equations, while plating Li into a 15μm crack in LLZO at 1 mA cm^{-2}. b) A comparison of an example SIF curve against the Mode I fracture toughness (K_{1c}). If the crack tip radius is sufficiently small, the generated SIF exceeds K_{1c} and thus that flaw becomes critical. These critical flaws thus act as initiation sites for alkali metal filaments... 77

Figure 3.18: Calculated CCDs based on the fracture criterion illustrated in Figure 3.17b. a) The calculated CCD for LLZO as a function of crack tip radius. b) The range of calculated CCDs for LLZO accounting for variations in local current densities and accounting for differences in the effective fracture toughness. c) A comparison of the calculated CCDs for LLZO as a function of temperature with the data from Chapter 3.1. d) A comparison of the calculated CCDs for NBA as a function of temperature with the data from Chapter 3.2. 78

Figure 4.1: Schematic of a symmetric Li-LLZO cell with Li metal as both the working and counter electrode. The cell is cycling within a mechanical testing unit that controls the applied stack pressure. 91

Figure 4.2: The potential response to a constant current density at varying stack pressures. The potential is normalized to the initial potential at the beginning of the constant current cycling. The potential responses for four different current densities are shown. 91

Figure 4.3: A comparison of the potential response to a constant current density of 0.2 mA cm^{-2} for Ta-stabilized LLZO ($Li_{6.5}La_3Zr_{1.5}Ta_{0.5}O_{12}$) and Al-stabilized LLZO ($Li_{6.25}Al_{0.25}La_3Zr_2O_{12}$). The same polarization behavior is observed for both compositions at the same stack pressures. 92

Figure 4.4: a) The potential response under a constant current of 0.1mA cm^{-2} while increasing and decreasing the stack pressure above the "critical stack pressure". Artifacts of the AC signal superimposed onto the DC signal are noticeable at the end of each pressure step. b) Representative EIS spectra at high (2.4MPa) and low (1.2MPa) stack pressure: inset highlights low frequency electrochemical reaction (ECR) behavior. c) The R_{int} calculated from the EIS taken at the end of each pressure step for each cycle. 94

Figure 4.5: a) Schematic of the three-electrode setup with a Ni reference electrode. b) Top-view illustrating the geometry of the LLZO billet with a third face cut perpendicular to the billet face.

c) EIS between the three different electrodes, showing blocking behavior for the Li-Ni configurations and non-blocking behavior for the Li-Li configurations. 95

Figure 4.6: Potential response under a constant current density of 0.2mA cm^{-2} and decreasing stack pressures. The usage of the Ni reference electrode allows for the decoupling of the Li stripping electrode (WE) and the Li plating electrode (CE). 96

Figure 4.7: The potential response near the open-circuit voltage (2.78V measured for Li vs Ni) in Figure 4.5, highlighting the polarization on the WE and the lack of change on the CE. 97

Figure 4.8: The potential response to both Li stripping and plating at a constant current density of 0.2mA cm^{-2} at a representative high stack pressure and representative low stack pressure. 0.35mA cm^{-2} of Li is stripped/plated each cycle. 99

Figure 4.9: a) The proposed microstructure of the Li/electrolyte interface above the "critical stack pressure" where the magnitude of the applied pressure is sufficient to maintain contact between Li and electrolyte. b) The proposed microstructure of the interface below the "critical stack pressure" where the applied pressure is insufficient to replenish the Li at the interface, resulting in void formation at the interface and a subsequent reduction in the contact area. 100

Figure 4.10: Comparison of the pressure-induced strain rate and the current-induced strain rate for cycling at 0.1mA cm^{-2}. The point at which the current-induced strain rate exceeds the pressure-induced strain rate is likely the point at which unstable void growth occurs, as evidenced by a decrease in the contact area, resulting in dramatic polarization. 103

Figure 4.11: The potential response as a function of stack pressure at constant current density. The potential response for the Na/NBA is shown in comparison to the potential response for Li/LLZO, reproduced from Figure 4.2. 111

Figure 4.12: The potential response after voids begin to form and then the stack pressure is significantly increased in attempts to re-wet the Na to the NBA surface. 112

Figure 4.13: The potential behavior at high stack pressures. a) The potential response while cycling the stack pressure at high values under a constant current density of 0.1 mA cm^{-2}. A curve smoothed using a 100-point moving average is shown in black while the original data is shown in grey. b) The impedance spectra measured *in operando* at the end of the first, sixteenth, and thirty-first pressure step in (a). c) The values of the individual components of the cell resistance measured at each pressure step in (a). d) The resulting potential response from (a) with a linear baseline subtracted out. 115

Figure 4.14: A basic model for understanding different features in the potential response to changing stack pressure. a) Potential response to changing stack pressures of Na/NBA at 0.4 mA cm^{-2}, reproduced from Figure 4.12, highlighting key features in the potential response. b) Schematic of void with radius r at the electrode/electrolyte interface 117

Figure 4.15: Examples of the predicted changes in area associated with Na metal stripping and its reciprocal for each of the features identified in Figure 4.12, corresponding to the following phenomena: a) current dominated void growth, b) creep dominated void closure, c) current and creep balancing, and d) impurity trapping 120

Figure 5.1: Schematic of a “Li-free” cell configuration and analysis of electrodeposition of Li onto a current collector at a constant current of 0.05 mA cm^{-2} at 25°C. (a) Schematic of a discharged “Li-free” configuration in comparison to state-of-the-art Li-ion and a solid-state Li metal battery with pre-deposited Li metal. Here, the current collector material is assumed to be Cu. (b) The potential response upon the initial application of a constant cathodic current, plating

Li metal onto a Ni current collector. (c) The impedance spectra at several points upon the Li plating process. 135

Figure 5.2: Electrochemical behavior upon Li plating and stripping at 25°C. (a) Potential response upon plating 5 mAh cm^{-2} of Li onto a Cu current collector at 0.05 mA cm^{-2} and then subsequently stripping at 0.05 mA cm^{-2}. (b) The Coulombic efficiency of Li plating and stripping of 3 mAh cm^{-2} of Li as a function of cycle number. The potential profiles are shown in Figure 5.3. (c) A comparison of the impedance spectra before and after the first Li plating and stripping cycle. 137

Figure 5.3: Potential profiles over several plating and stripping cycles at different current densities corresponding to the data plotted in Figure 5.2b. 138

Figure 5.4: Cross-sectional SEM-FIB analysis of the LLZO and the current collector interface. SEM (a) as assembled, (b) after plating 5 mAh cm^{-2} of Li, and (c) after plating and then stripping of 5 mAh cm^{-2} of Li. Elemental maps for Cu and Zr at the interface (d) as assembled, (e) after plating, and (f) after plating and stripping. Metallic Li is observed under secondary electrons in between the Cu and LLZO layer in (b) but cannot be detected since the characteristic x-ray energy falls outside of the detection range of EDS.. 139

Figure 5.5: Low magnification SEM of FIB-milled Cross-Sections from Figure 5.4. (a) Cu current collector as laminated onto LLZO, (b) after 5 mAh cm^{-2} of Li is plated, and (c) after 5 mAh cm^{-2} of Li is plated and stripped. The intermediate Li layer in between the Cu and the LLZO in (b) more clearly shows textural features at lower magnifications which indicates the presence of an intermediate phase rather than empty space, despite the high color contrast. Not all regions of the interface after stripping 5 mAh cm^{-2} of the plated Li exhibit such a prominent separation between Cu and LLZO that is observed in (c). One such region of a less pronounced

separation is shown in (d), which exhibits a smaller gap between Cu and LLZO but is still more pronounced than in (a) and shows a similar residue between Cu and LLZO that is also observed in (c). 140

Figure 5.6: *ex situ* SEM of the LLZO surface after removal of the current collector. LLZO surface after plating (a) 4 μAh cm^{-2}, (b) 30 μAh cm^{-2}, (c) 200 μAh cm^{-2}, (d) 620 μAh cm^{-2}, (e) 1.0 mAh cm^{-2}and (f) 1.6 mAh cm^{-2} of Li. The SEM images are correlated to a typical potential profile upon plating, showing three distinct regimes: 1) Li nucleation, 2) lateral growth of the Li nuclei, and 3) coalescence of the nuclei and subsequent vertical growth of the coalesced Li film. 142

Figure 5.7: Schematic of nucleation and growth process. (a) shows the layers present and Li nucleates (treated as spherical in the nucleation model) and (b) shows the critical nucleate radius as a function of nucleation overpotential. c-e show three possible mechanisms for nucleate growth, including (c) deposition on the nucleate leading to vertical growth and separation of the adjacent CC/LLZO interface, (d) continued deposition at the nucleate center, with mechanical forces at the interfaces and Li's low yield strength leading to horizontal plastic flow of Li, or (e) deposition at the nucleate edges. 146

Figure 5.8: Peel Tests for Measuring Macro-scale Work of Adhesion. 90° Peel tests to measure the work of adhesion of the laminated current collectors on the LLZO surface. The dashed lines indicate the average peel force for each current collector type for three different samples each. The average peel force is measured from the average force over the steady-state region (~0.4 – 1.0 peel strains). The average work of adhesions for Cu and Ni are estimated to be within the range of 1-10 J m^{-2}. 147

Figure 5.9: Critical Current Density Measurement of 25 μm *in situ* Plated Li 149

Figure 5.10: Cycling behavior of a Li metal battery composed of an NCA/PEO composite cathode, LLZO, and *in situ* plated Li metal anode cycling at 60°C. (a) Representative charge/discharge curves cycling at a C/10 rate. (b) The areal capacity and Coulombic efficiency as a function of cycle number. (c) The impedance spectra measured after every ten cycles. ... 151

Figure 5.11: Cycling behavior of a Li metal battery composed of an NCA/PEO composite cathode, LLZO, and *in situ* plated Li metal anode cycling at 80°C... 152

Figure 5.12: Cycling behavior of a Li metal battery composed of a Li metal foil, LLZO, and *in situ* plated Li metal anode cycling under identical conditions as in Figure 6. The *in situ* anode is formed with a capacity of 2.7 mAh cm^{-2} with 0.85 mAh cm^{-2} (corresponding to the maximum capacity value in Figure 6b) being cycled at 60°C . (a) Representative charge/discharge curves cycling at a C/10 rate. (b) The areal capacity and Coulombic efficiency as a function of cycle number. (c) The impedance spectra measured after every ten cycles....................................... 153

Figure 6.1: Schematic of the different mechanical environments at the interface between the alkali metal anode and a thick (~1 mm) ceramic electrolyte and a thin (≤100 µm) ceramic electrolyte. The effects of bending moments on defects in the ceramic electrolyte is shown for a) thick and b) thin membranes. The effects of voids in the alkali metal electrode is shown for c) thick and b) thin membranes.. 161

Figure 6.2: The possible evolution of electroplated Li metal under two different current schemes. The hypothetical interface evolution of Li plating onto a blocking electrode under a) a DC current and b) a pulsed current, allowing for relaxation of the plated Li............................ 164

Abstract

With the ever-increasing demands for safe, reliable energy storage, solid-state batteries have emerged as a potential candidate to accelerate widespread adoption of electrified technology. While lithium-ion batteries currently dominate the rechargeable battery market, it is becoming apparent that these systems cannot provide the energy and power densities, lifetime, safety, and costs for electric vehicles requiring large format cells. However, by replacing the conventional liquid electrolyte with a solid-state electrolyte, advanced electrodes like alkali metal anodes could be enabled, which would provide significant advances in energy density, safety, and lifetime. However, despite the tremendous progress made in the field of solid-state batteries in the past decade, current solid-state battery performance generally remain inferior to that of incumbent technology.

In an effort to better understand the limitations of solid-state batteries, this dissertation explores the coupled electrochemical and mechanical interactions between ceramic solid-electrolytes and alkali metal anodes. Two relevant model electrolyte systems, the $Li_7La_3Zr_2O_{12}$ garnet and the Na-β”-alumina electrolytes, are studied when coupled with Li metal and Na metal anodes, respectively. First, the effect of temperature on short-circuiting caused by penetration of the electroplated metal through the solid-electrolyte is explored. It is observed that both systems exhibit an increase in critical current density with increasing temperature. While both systems behave similarly qualitatively, the critical current densities of the Na-based system are significantly higher (12 mA cm^{-2} at room temperature) than that of the Li-based system (1 mA cm^{-2}). The differences between the two systems are then correlated to differences in the mechanical properties and conductivities of the electrolytes using a fracture mechanics based model. Second, the effect of external stack pressure on unstable metal depletion at the anode/electrolyte interface is examined. It is demonstrated that at low stack pressures and/or high current densities, significant increases in cell resistance are observed in both systems. These increases in cell resistance are shown to be isolated to the metal stripping reaction, suggesting that the formation of voids at the electrode/electrolyte interface results in significant contact loss. The evolution of these voids is then analytically modeled to correlate morphological changes of the interface with distinct features in the cell cycling behavior. Lastly, Li metal electrodeposition onto a blocking electrode is explored for the enabling of "Li-free" battery manufacturing. It is observed that significant capacities (>5 mAh cm^{-2}) of Li metal could be reversibly plated and stripped onto/from a current collector over several cycles with high efficiencies and the nucleation behavior onto the current collector is examined. To demonstrate proof-of-concept, prototypical all-solid-state batteries are manufactured with the "Li-free" approach exhibiting high efficiency. These designs introduce a novel approach toward improving the energy density and low-cost manufacturability of solid-state batteries. Overall, this dissertation explores the fundamental coupling between electrochemistry and mechanics at the anode/electrolyte interface in these systems and provides practical guidelines for the design, manufacturing, and operation of next-generation solid-state batteries.

Chapter 1 Introduction

With the ever-increasing consumption of energy on a global scale, the past decade has witnessed a substantial increase in carbon dioxide emissions that highlights the unsustainability of society's reliance on fossil fuels. While recent reports show that 80% of energy produced in the United States in 2019 was in the form of fossil fuels, the question of energy storage continues to impede the growth of renewable energy sources[1]. Because of the intermittency of renewable energy sources like wind, solar, and tidal, there exists a vital need for reliable forms of energy storage. A prime example of the impact energy storage could have on the global energy landscape lies within the transportation sector, where 28% of our energy was consumed in the last year according to recent reports[1,2]. Given that the vast majority of the energy consumed in the transportation sector comes from fossil fuels, replacement of those fuels with electric energy from renewable sources would have major impacts on environmental sustainability. In recent years, the transportation sector has witnessed remarkable progress in the area of vehicle electrification, however, widespread adoption of electric vehicles still remains severely limited. One of the biggest challenges impeding the growth of electric vehicles is the limitation of current battery technology. While lithium-ion batteries are currently the industry standard for electric and hybrid electric vehicles, their shortcomings in terms of specific energy, specific power, safety, and cost are becoming a major roadblock toward the widespread electrification of the transportation sector[3]. Compared to fossil fuels, the energy densities of current batteries are extremely low, requiring significantly higher volumes of batteries to provide comparable driving ranges. With shorter driving ranges, the time needed to recharge the car battery also becomes important and currently pales in comparison to the few minutes needed to fill a gas tank. The safety of the battery also plays an important role, as incidents involving lithium-ion battery fires and explosions in consumer devices, are a major factor in public reception and widespread adoption. Finally, the cost of current battery technologies remains too high to be widely cost-effective, which is exacerbated by the shorter lifetimes of batteries in comparison to internal combustion engines.

Many challenges still remain toward rapid electrification of the transportation sector, but the environmental impact that vehicle electrification can have is tremendous. While the path may be arduous, luckily there are many approaches towards addressing these issues. This dissertation will present a combined materials science and solid-state electrochemistry approach toward the development of new battery technologies, particularly solid-state batteries. Overall, this dissertation presents solid-state batteries as a viable candidate for use in next-generation electric vehicles and explores different aspects of the electrochemistry and mechanics at internal interfaces of the battery.

The following sections provide background on the fundamental principles behind battery operation, the current state of battery technologies, and the prospects of solid-state batteries.

1.1 Fundamentals of Battery Operation

At the heart of the technology, a battery is a device that converts the energy stored within chemical bonds into electrical energy. This device consists of two electrochemical half cells which undergo a coupled reduction-oxidation (redox) reaction that forces electrons to flow through an external circuit. In one half cell, an oxidation reaction occurs, releasing an electron from the electrode material into the external circuit. This electrode is the negative electrode, commonly referred to as the anode. In the opposite half cell, the electrode material receives an electron from the external circuit, thus undergoing a reduction reaction. This electrode is the positive electrode, commonly referred to as the cathode. This is illustrated by the following equations in which one electron is transferred in the redox reaction:

$$Anode\colon\ A \rightarrow A^{+} + e^{-} \tag{1.1}$$

$$Cathode\colon\ C^{+} + e^{-} \rightarrow C \tag{1.2}$$

where A is the anode material and C is the cathode material. In order to maintain electroneutrality while electrons flow in the external circuit, positive ions must flow in between the anode and cathode. This necessitates a third material separating the anode and cathode, known as the electrolyte, which allows for the flow of positive ions between anode and cathode. This configuration is illustrated in Figure 1.1a.

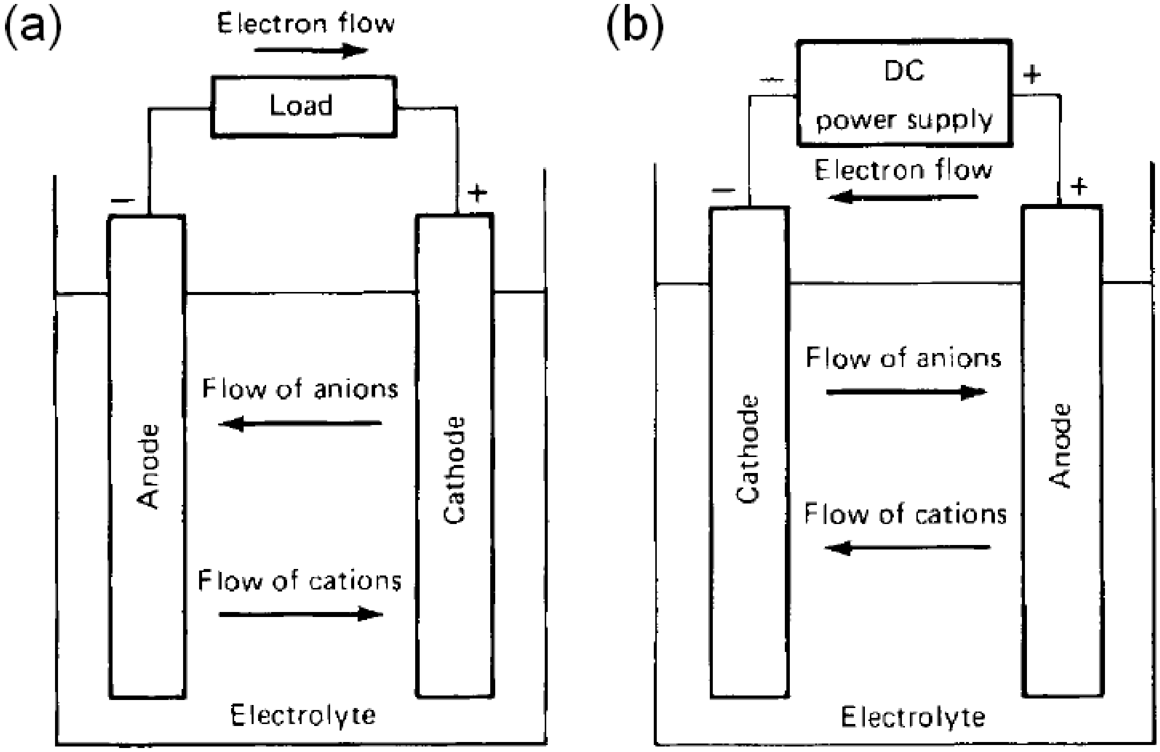

Figure 1.1: Schematic of an electrochemical cell while a) discharging and b) charging. Adapted with permission from Ref. [4].

The chemical energy associated with these redox reactions is expressed as ΔG_r^0, the standard Gibbs free energy change per mole of reaction. At open-circuit, when no electrons can flow externally, this chemical driving force is balanced by an equal and opposite electrostatic driving force. The balance between these two forces can be expressed by the equation:

$$E^0 = -\frac{\Delta G_r^0}{nF} \tag{1.3}$$

where n is the number of electrons transferred, F is Faraday's constant, and E^0 is the standard potential. The difference between the standard potential of each electrode gives the overall electrochemical cell potential given by:

$$E = E_+^0 - E_-^0 \tag{1.4}$$

where E is the overall cell potential, and E_+ and E_- are the standard potentials for the positive and negative electrodes respectively. If the cell is then electrically connected, this cell potential is converted into an externally measured voltage which can then be used to perform useful electrical work, although in practice, the measured voltage will vary from this value due to ohmic losses or activation overpotentials.

In principle, if a sufficiently large external voltage is applied to the cell, the flow of ions and electrons can be reversed, thus increasing the internal chemical energy by consuming external electrical energy. In this process, by reversing the anode and cathode reactions, the cell is recharged, which is illustrated in Figure 1.1b. This creates a distinction between primary batteries, which are designed for only a single discharge, and secondary batteries, which are designed to be charged and recharged multiple times. The ability to recharge the system depends on a number of factors, which affect the reversibility of the individual electrode reactions.

1.2 Lithium-Ion Batteries

In the past few decades, alongside the rise of ubiquitous electronics also came the rise of rechargeable batteries. Out of the many candidates, the lithium-ion battery (Li-ion) has dominantly become the most common type of secondary battery. While many different electrode couples fall under the category of Li-ion, the typical Li-ion battery is comprised of a graphitic carbon anode, a layered transition metal oxide cathode, and a Li-salt dissolved in an organic solvent as an electrolyte. Both the graphitic carbon anode and layered metal oxide cathode are known as insertion, or intercalation, compounds. For this class of materials, the redox reaction associated with charge/discharge involves the intercalation (insertion) and de-intercalation (extraction) of a Li^+ into or out of an interstitial site in the host structure. The reaction between a graphitic carbon and a metal oxide $LiMO_2$ is given by the following:

$$Negative\text{:}\ \ C + xLi^+ + xe^- \leftrightarrow Li_xC \tag{1.5}$$

$$Positive\text{:}\ \ LiMO_2 \leftrightarrow Li_{1-x}MO_2 + xLi^+ + xe^- \tag{1.6}$$

$$Overall\ cell\text{:}\ \ LiMO_2 + C \leftrightarrow Li_xC + Li_{1-x}MO_2 \tag{1.7}$$

As seen in these reactions, during charging/discharging of the battery, the Li^+ are simply shuttling back and forth between the two electrodes, giving rise to the term “rocking-chair battery”. The highly reversible nature and facile kinetics of these intercalation reactions along with the low reduction potential and low atomic mass of Li give an unprecedented combination of high gravimetric and volumetric energy density, high rate capabilities, and long cycle life that make Li-ion batteries suitable for a myriad of different applications[4,5].

1.3 Solid-State Batteries

Although the qualities of Li-ion batteries have made them suitable for a wide variety of technologies in the small-scale electronics sector, their limitations on the larger scale are becoming increasingly apparent, which has motivated a movement in the scientific community to go “beyond Li-ion”. One of the potential solutions to enable batteries that meet the projected energy and power density needs of emerging technologies is the solid-state battery. As mentioned in Chapter 1.2, the electrolyte in a typical battery is a salt dissolved in a liquid solvent. In the case of Li-ion batteries, this is typically $LiPF_6$ dissolved in a mixture of organic solvents like ethylene carbonate, dimethyl carbonate, diethyl carbonate, and/or propylene carbonate. Due to issues of chemical and thermal stability, the usage of these organic electrolytes limits the potential windows, current densities, and temperatures at which these batteries can operate at without degradation of the electrolyte. Furthermore, the flammability and risk of thermal runaway of these organic electrolytes has become a major safety concern. As the name suggests, a solid-state battery circumvents many of these issues by replacing the liquid electrolyte with a fast-ion-conducting solid material. The solid-electrolyte is a material that can conduct ions through the solid-state, thereby acting as both the electrolyte and separator between anode and cathode. A schematic of a solid-state battery is illustrated in Figure 1.2. In principle, because of the improved chemical, electrochemical, mechanical, and thermal stability of many of these solid-electrolytes, solid-state batteries offer a number of benefits over conventional liquid-based batteries. To list a few, solid state electrolytes can be coupled with more advanced electrode materials which can offer dramatically higher energy densities, eliminate the safety risks of thermal runaway, reduce chemical cross-talk between electrodes, and reduce cycling inefficiencies related to electrolyte decomposition.

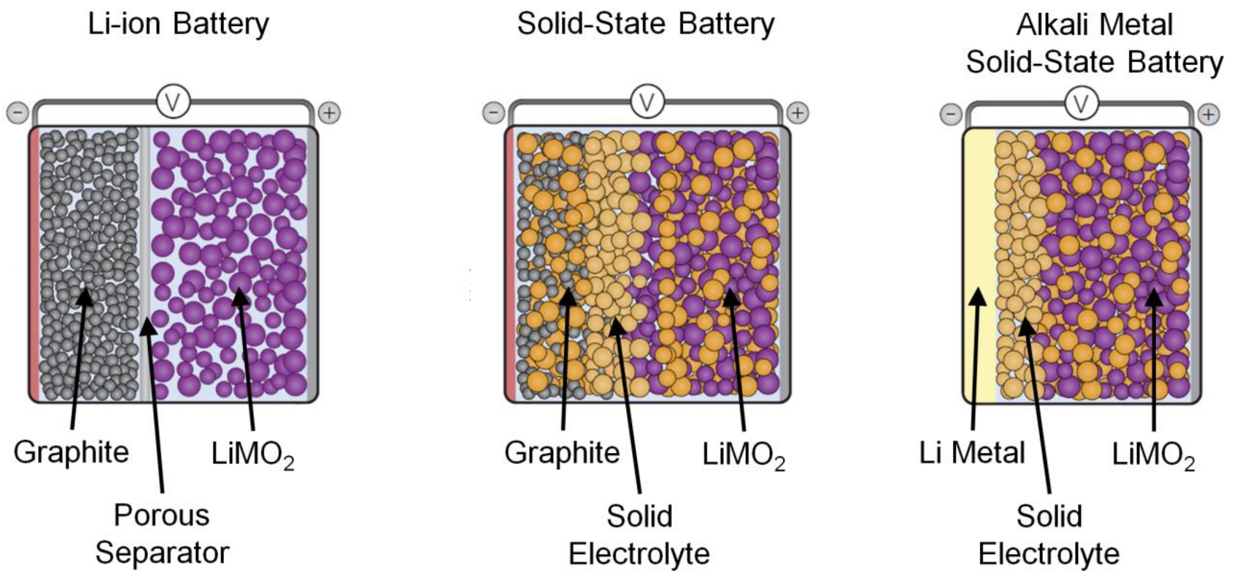

Figure 1.2: Schematic of a Li-ion battery, solid-state battery, and a Li metal solid-state battery. Adapted with permission from Ref. [100].

1.3.1 Solid-State Electrolytes

The mechanisms of ion transport in the solid-state have been recognized for almost two centuries and have served as a key contribution to the development of solid-oxide fuel cells. However, until the discovery of the silver iodide and the β-alumina families of fast ion-conductors several decades ago, no known materials could conduct ions at relatively low temperatures. The discovery of these low temperature ion-conductors led to the possibility of solid-state electrochemical devices, including batteries, sensors, fuel cells, and transducers. Since then, catalyzed by the discovery of the first fast Li-ion conductor and immense popularity of Li-based chemistries, the field of solid-state ionics and the development of solid-state electrolytes has progressed at dramatic rates, to the point where currently several families of fast ion conductors that rival (or even exceed) the conductivities of liquid electrolytes have been discovered.

Currently, several classes of solid-electrolytes, both organic and inorganic, have been developed for application in solid-state batteries. Regardless of material, any solid-electrolyte for a solid-state battery must ideally satisfy the following requirements.

1.3.1.1 High total ionic conductivity

High total ionic conductivities ($\geq$ 1 mS cm^{-1} in order to rival Li-ion liquid electrolytes) are necessary to minimize internal Ohmic losses. In the realm of fast Li-ion conductors, typical room temperature ionic conductivities range from 10^{-6}-10^{-2} S cm^{-1} [6]. For many crystalline ceramic electrolytes, despite high bulk conductivity, ion transport is severely limited by transport across grain boundaries, which can drop the total ionic conductivity several orders of magnitude. This is notable in many electrolytes including the perovskite family and NaSICON family, while having less of an effect on other electrolytes, like the garnet family and the β-alumina family. Meanwhile sulfide materials are less limited by grain boundary resistance, like the thio-LiSICONs and argyrodites, giving total conductivities on the order of 10^{-3}-10^{-2} S cm^{-1}, with the notable $Li_{10}GeP_2S_{12}$ sulfide having the highest known conductivity of 10^{-2} S cm^{-1} [6]. In comparison to inorganic electrolytes, organic polymer electrolytes typically have lower conductivities ~10^{-7}-10^{-5} S cm^{-1} at room temperature and therefore require elevated temperatures to operate[7].

1.3.1.2 Electrochemical and mechanical stability

Stability against the desired electrode materials is critical to minimize parasitic side reactions and electrolyte degradation. When coupled against alkali metal anodes, which have low reduction potentials, many of the known solid-electrolytes suffer from electrochemical instability against the anode, which results in electrolyte degradation. This is the case of many of the sulfide materials, the perovskite family of oxides, and some of the NaSICON type of electrolytes. Meanwhile, the lithium phosphorous oxide nitride (LiPON), the garnets, and many polymer electrolytes exhibit good stability against the alkali metal anode[6,7].

1.3.1.3 Low electronic conductivity

In order to minimize self-discharge, the electrolyte must have low electronic conductivities (electronic transference numbers $< 10^{-8}$). While high electronic conductivity is not an issue in a majority of the known solid-electrolytes as prepared, decomposition products of the electrolyte can have high electronic conductivity that internally short the battery. Many of these decomposition products are a direct result of spontaneous reduction when placed in contact with an alkali metal anode. Therefore, the issue of electronic conductivity is a concern for many of the unstable electrolytes within the sulfide, perovskite, and NaSICON categories.

1.3.1.4 Operation within a wide temperature range

One of the advantages of solid-electrolytes materials is that their conductivity is improved at elevated temperatures, which lessens the need for thermal management systems that may be necessary when dealing with liquid electrolytes. Therefore, inorganic electrolytes can typically operate within wider temperature ranges. Organic polymer electrolytes, however, are typically much less thermally stable than their inorganic counterparts and therefore can only operate in narrow temperature ranges, due to low conductivities at lower temperatures and thermal instability at higher temperatures.

1.3.1.5 Low-cost manufacturability at relevant thicknesses (~10-100 µm to compete with traditional separators)

One of the biggest benefits of organic polymer electrolytes is the ability to manufacture them with scalable, low-cost methods, given that the manufacturing processes are very comparable to the manufacturing of traditional polymer separators. For inorganic electrolytes, manufacturing becomes a major challenge. For oxide materials, high temperatures and high pressures are required for manufacturing which becomes costly and energy intensive. Sulfides, due to their higher ductility, require less temperature and pressure compared to oxides and also can be more easily formed into thin films and handled without fracturing. However, due to the high reactivity of sulfide materials with moisture in the air, very controlled manufacturing atmospheres are necessary, which adds additional costs. Although LiPON is typically synthesized on the thin film scale, microns thick, it is limited by the scalability of the deposition/sputtering processes that are required to manufacture it.

1.3.1.6 The electrolyte and manufacturing process must be environmentally benign

While most of the inorganic and organic solid electrolytes are environmentally benign, as far as it is currently known, reactions between sulfide electrolytes and ambient air can result in the generation of toxic gases which is a significant limitation of these materials.

An overview of these solid-electrolyte properties is listed in Table 1.1. As to be expected, there currently is no single “perfect” solid-electrolyte material that satisfies all of the ideal requirements. However, in order to achieve the high energy densities required by applications like electric vehicles, the usage of an alkali metal anode is necessary. This constraint emphasizes the requirement for the electrolyte in an alkali metal battery to be electrochemically stable at low reduction potentials. Of the many electrolyte types listed, the oxides prove to be very promising given that this family contains the few electrolytes that are stable at these low potentials. In particular are the garnet-structured family of Li-ion conductors and the β-alumina family of Na-ion conductors, which will be the focus of this dissertation.

Table 1.1: An overview of common solid-electrolyte materials in the literature[6–13]

Common Compositions	Typical Ionic Conductivities (S cm^{-1})	Typical Electrochemical Stability Windows	Advantages/Disadvantages
		Fast Li$^+$ Conductors	
Oxides			
Garnets $Li_7La_3M_2O_{12}$ M = Nb, Ta, Zr	~10^{-5}-10^{-3}	~ 0 – 6 V	Advantages: High ionic conductivity, stable against Li metal Disadvantages: High temperature manufacturing, brittle
Perovskites $Li_{3x}La_{2/3-x}TiO_3$ (0.04 < x < 0.17)	~10^{-6}-10^{-3}	> ~1.8 V	Advantages: High bulk conductivity Disadvantages: High temperature manufacturing, high grain boundary resistance, unstable against Li metal, brittle
Phosphates			
NaSICON $LiM_2(PO_4)_3$ M = Zr, Ti, Hf, Ge, Sn	~10^{-5}-10^{-3}	~0.8 – 7 V	Advantages: High ionic conductivity, good chemical stability Disadvantages: Unstable against Li metal
LiPON Li_3PO_4 (target)	~10^{-6}	~0 – 5.5 V	Advantages: Stable against Li metal Disadvantages: Low ionic conductivities, can only manufacture on thin film scale
Sulfides			
Thio-LiSICON $Li_xM_{1-y}M'_yS_4$ M = Si, Ge M' = P, Al, Zn, Ga, Sb	10^{-5}-10^{-2}	~1.7 – 2.3 V	Advantages: High ionic conductivity, ductile & manufacturable as thin films, low grain boundary resistance Disadvantages: Unstable against Li metal, unstable in ambient air
Argyrodite Li_6PS_5X X = Cl, Br, I	~10^{-3}	~0 – 7 V	Advantages: High ionic conductivity, ductile & manufacturable as thin films, low grain boundary resistance Disadvantages: Unstable in ambient air
Polymers			
Poly(ethylene oxide) Poly(methyl methacrylate) Polyacrylonitrile Poly(vinylidene difluoride)	~10^{-4}-10^{-3} (at 60-80°C)	~0 – 4 V	Advantages: Low-cost & easy to manufacture as thin films, flexibility Disadvantages: Low ionic conductivities at room temperature, thermal stability
		Fast Na$^+$ Conductors	

Oxides			
Na-β”-alumina Na-Al_2O_3	10^{-3}	~0 – 3.5 V	Advantages: High ionic conductivity, stable against Na metal Disadvantages: High temperature manufacturing, brittle
Phosphates			
NaSICON $Na_{1+x}Zr_2Si_xP_{3-x}O_{12}$ $0 \leq x \leq 3$	10^{-3}	~0.5 – 4.5 V	Advantages: High ionic conductivity, good chemical stability Disadvantages: Unstable against Na metal
Sulfides			
Thio-NaSICON Na_3PX_4 X = S, Se $Na_{10}M_{1-y}P_2S_{12}$ M = Si, Ge, Sn	10^{-4}-10^{-2}	~1.3 – 2.3 V	Advantages: High ionic conductivity, ductile & manufacturable as thin films, low grain boundary resistance Disadvantages: Unstable against Na metal, unstable in ambient air
Hydrides			
$Na_2B_xH_x$ x = 10, 12	10^{-4}-10^{-2}	~0 – 3 V	Advantages: High ionic conductivity, ductile & manufacturable as thin films Disadvantages: Low oxidation voltage

Although there exist a variety of different compositions of garnet electrolytes, currently the most notable and most popular composition is the Li-stuffed garnet, $Li_7La_3Zr_2O_{12}$ (LLZO). In the LLZO, a framework structure is formed by a combination of LaO_8 dodecahedra and ZrO_6 octahedra, while Li atoms randomly and partially occupy the interstitials of the framework structure. This interstitial sublattice becomes a three-dimensional network of conduction pathways for the Li^+ to move through, allowing for the fast ion conduction. However, the magnitude of the Li^+ conductivity through the interstitial network is dependent on the crystal structure. The LLZO adopts two different crystal structures, a cubic structure and a tetragonal structure. Due to differences in the Li ion ordering and availability of Li vacancies in the interstitial sublattice, it was discovered that the cubic polymorph of LLZO has a significantly higher ionic conductivity (10^{-4}-10^{-3} S cm^{-1}) compared to the tetragonal polymorph (10^{-6}-10^{-5} S cm^{-1} [14]. Therefore, due to the high ionic conductivity, cubic LLZO has become the desired polymorph. However, because the tetragonal polymorph is actually the stable structure at room temperature, it is necessary to stabilize the cubic phase. This is typically done by the introduction of Li vacancies via doping of supervalent cations such as Al^{3+}, Ta^{5+}, and Ga^{3+}. With continued development over the past decade, cubic LLZO has become a popular solid electrolyte material because of its high ionic conductivity >10^{-4} S cm^{-1} (including grain boundary resistance), excellent chemical stability against metallic Li, wide electrochemical window (up to 9 V vs Li/Li^+), ability to achieve low interfacial resistances (<10 Ω cm^2) against metallic Li without the need for interfacial coatings, and relative inertness in ambient air. However, currently LLZO is limited by the difficulty of manufacturing, which requires high temperatures (>1000°C) and/or high pressures to densify and is extremely brittle in thin film geometries.

The β-alumina family of oxides was one of the original fast ion conductors discovered and is known to conduct a variety of different ions, including both Li^+ and Na^+, although it has found the most success as the Na^+ conductor, known as Na-β-Al_2O_3 (NBA). The β-alumina materials are characterized by their layered structure, which is composed of alternating closely-packed slabs and loosely-packed layers. The closely-packed slabs are comprised of alumina spinel blocks while the Na^+ is contained and free to move through the loosely-packed layers, also known as the conduction planes. The spinel blocks are bonded to adjacent spinel blocks via the conduction planes. The β-alumina materials also adopt two distinct crystal structures, known as the β-alumina (β-Al_2O_3), which has a hexagonal lattice, and the β”-alumina (β”-Al_2O_3), which has a rhombohedral lattice. The distinction between the two structures originates from a difference in the stacking order of spinel blocks and conduction planes. Because the stacking of layers in the β”-alumina can accommodate larger amounts of mobile ions, the β”-alumina phase exhibits an order of magnitude higher ionic conductivity (~10^{-2} S cm^{-1}) at room temperature over the β-alumina phase. Because of the high conductivity, the β”-alumina phase has become the preferred phase for battery applications. While it is challenging to prepare exclusively β”-alumina, the β”-alumina can be stabilized by doping of mono or divalent ions such as Li^+ or Mg^{2+}. Therefore, going forward, any references to NBA will refer to the β”-alumina phase. Due to its high ionic conductivity (>10^{-3} S cm^{-1}) (including grain boundary resistance), excellent stability against Na metal, relative inertness in ambient air, and chemical abundance, NBA has become a promising solid-electrolyte material for Na metal batteries. However, due to the high temperatures (>1500°C) required to sinter NBA, manufacturing remains a challenge. Furthermore, interfacial resistance between NBA and Na metal can be very high, dropping the total conductivity by orders of magnitude. While this is typically circumvented by coupling NBA with molten Na at high temperatures (>200°C), as will be discussed in subsequent chapters, it has recently been demonstrated that low interfacial resistances (<10 Ω cm^2) can be achieved at room temperature without the use of interfacial layers.

1.3.2 Alkali Metal Anodes

One of the most desirable advantages of using a solid-state electrolyte, is the potential to enable the alkali metal anode. Currently graphitic carbons are the most commonly used anode material in a Li-ion battery. As described in Chapter 1.2, the Li-ion battery operates off of a “rocking chair” concept, with Li^+ shuttling in between two intercalation electrodes. The usage of two intercalation electrodes presents a trade-off. The advantage is the long cycle life that can be achieved due to the highly reversible nature of intercalation reactions. However, this comes at the cost of compromised energy density, which comes in the form of excess mass and volume associated with the host structure[15]. In comparison, if the Li in the system is in the form of pure metallic Li instead of a Li-C alloy, the lack of excess mass gives rise to an order of magnitude difference between the theoretical capacities between Li metal (3860 mAh g^{-1}, 2061 mAh cm^{-3}) and conventional graphite anodes (372 mAh g^{-1}, 818 mAh cm^{-3}). This high theoretical capacity coupled with the strongest reducing potential of all the elements (-3.04 V vs SHE) make Li metal one of the most desirable anode materials for Li-based battery chemistries. However, although its strong reducing potential is highly desirable to make high voltage batteries, it is simultaneously one of its biggest disadvantages. Due to the extreme chemical and electrochemical reactivity that accompanies the extremely low reduction potential, it is a major challenge to find compatible electrolytes that are thermodynamically stable against metallic Li. Any chemical or electrochemical instability against the electrolyte will cause parasitic side reactions between the electrolyte and Li metal during battery operation, which typically leads to low cycling efficiencies and therefore a low cycle life. Furthermore, electrodeposition and depletion of metals at higher current densities is typically inhomogeneous, which is only worsened by the constant formation and pulverization of these interphases. This not only limits the applicable current densities, but also severely limits the cycle life. In the most extreme cases, the build-up of passivated ("dead") Li or the growth of Li dendrites due to morphological instabilities can bridge the gap between anode and cathode resulting in an internal short-circuit, leading to a battery fire caused by thermal runaway. Because of these issues, the usage of Li metal until now has been limited to the laboratory scale or for usage in primary batteries. However, with the advent and rapid progress in the area of advanced electrolytes, the possibility for usage of Li metal as a secondary battery anode material is once again being explored.

Although Li metal has garnered the most attention in recent years because of the popularity of Li-based chemistries, the progress of advanced electrolytes may also enable the usage of other alkali metal anodes that suffer from similar limitations. Most notably is Na metal, which has comparable reducing potential (-2.71 V vs SHE) and theoretical capacities (1166 mAh g^{-1}, 1129 mAh cm^{-3}) which make them good candidates for similar high energy density applications. While the energy density and potentials of Na-based chemistries are lower than Li-based chemistries, the natural abundance of Na-containing compounds compared to Li-containing compounds make Na-based chemistries significantly more attractive in terms of costs and sustainability. However, similar to Li metal, Na metal anodes have not seen widespread adoption due to similar issues of stability. Na metal anodes are commercially used in the molten state, in high temperature batteries using solid-electrolytes, like the Na-S and $Na\text{-}NiCl_2$ (ZEBRA) systems. While these systems can be used for stationary grid scale storage, the need to operate at temperatures ≥300°C severely limit their application in other technologies, including electric vehicles. Following closely behind the revived interest of Li metal, interest in Na metal anodes have also experienced a revival in the scientific community as a cost-efficient solution to meet the high energy density demands of emerging technology. Similar to the case of Li metal, with recent advances in electrolyte development, the ability to utilize Na metal anodes at room temperature is once again a possibility.

1.4 Challenges Facing Solid-State Batteries

Because of the maturity of the technology and their dominance over the secondary battery market, solid-state batteries are still far from being a viable competitor to current Li-ion batteries. While solid-state batteries offer drastic improvements in several key performance metrics of Li-ion batteries, practical demonstration of these advantages in realistic systems has yet to be achieved.

While the cost of solid-state batteries will heavily depend on the preferred battery architecture, advances in manufacturing, and the economic and political inertia to drive the battery market, battery performance is still hindered by our limited understanding of these systems. Since the energy density of the battery is simply dependent on the cell geometry and the battery electrodes, the achievable energy densities are also highly dependent on the preferred battery architecture and the technological viability to manufacture these architectures. However, the power density remains one of the biggest challenges in solid-state batteries because of our lack of understanding of many of the kinetic phenomena that occur during battery operation. Because these phenomena are inherent to the cell chemistry and therefore cannot easily be circumvented, understanding the mechanisms controlling the rate capabilities of solid-state batteries is currently a topic of immense interest in the battery community.

Although tremendous progress has been made to improve the rate capabilities in recent years, the rate capabilities of solid-state batteries are still far below that of Li-ion batteries. Unlike with conventional liquid electrolytes, where the anode/electrolyte is a solid/liquid interface, the anode/electrolyte interface in a solid-state system is a solid/solid one. This means that any morphological changes on the anode side by either charging or discharging of the battery, is constantly changing the electrochemical and physical landscape of the interface. This creates a complex, dynamic interplay between electrochemistry and solid mechanics that is constantly occurring at the electrode/electrolyte interface in a solid-state battery, illustrated in Figure 1.3. Given that these morphological changes are time-dependent and can potentially result in detrimental or irreversible changes of the interface, both the rate capabilities and the long-term stability of solid-state batteries are effectively limited by these interface phenomena. Therefore, in order to further improve both the rate capabilities and stability of solid-state systems, a deeper understanding of the coupled electrochemo-mechanical phenomena at these internal interfaces is crucial.

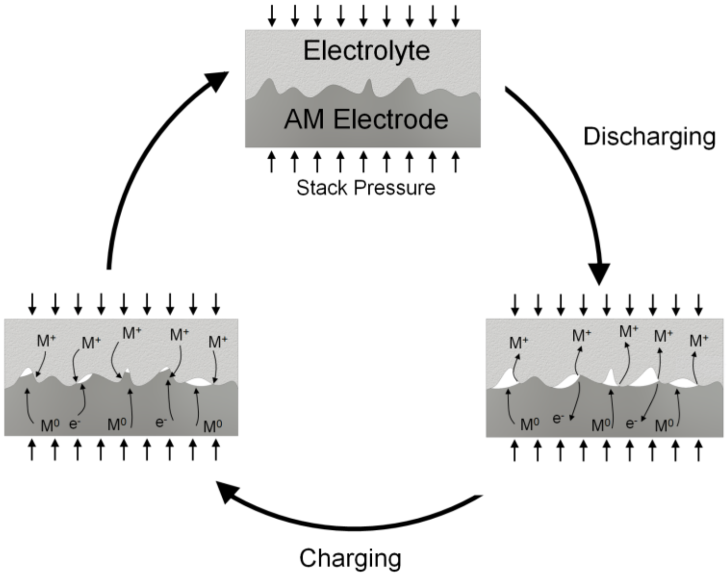

Figure 1.3: Schematic of the morphological changes that occur during cycling at the alkali metal electrode/solid-electrolyte interface.

This dissertation looks to provide further insight into these interface phenomena in Li and Na metal solid-state batteries. Using two model systems, Li metal coupled with the garnet LLZO electrolyte and Na metal coupled with the Na-β”-alumina electrolyte, the behavior of the internal interfaces is studied under a variety of conditions. First, Chapter 3 will look to further understand the initiation and propagation of metal filaments in oxide electrolytes by studying and comparing the effects of temperature on the critical current density in both the Li/LLZO and Na/NBA systems. Second, Chapter 4 will discuss the effects of external stack pressure on the total cell resistance, which is one of the first works to identify a rate-limiting mechanism that occurs at the anode/electrolyte interface upon discharging (stripping). The results from Chapter

3 and Chapter 4 not only provide mechanistic insight into the rate-limiting phenomena at these interfaces, but also suggest methods to improve both the charging and discharging rates of solid-state batteries. Finally, in Chapter 5, the nucleation behavior at a blocking-electrode/LLZO interface upon electrodeposition is investigated. The results not only provide a new perspective on nucleation behavior at solid-solid interfaces, but also demonstrate the feasibility of a low-cost method of manufacturing novel solid-state battery architectures.

Together, this dissertation highlights unique electrochemical and mechanical couplings that play a critical role in how these systems operate, providing new perspectives on the continued development of solid-state battery technology.

Chapter 2 Experimental Methods

This chapter will present an overview of the common experimental procedures that act as the foundation for the work presented in subsequent chapters. This includes solid-electrolyte synthesis and processing, assembly of electrochemical cells consisting of alkali metal electrodes and solid-electrolyte, and electrochemical characterization using impedance spectroscopy.

2.1 Electrolyte Synthesis and Processing

Because of its desirable electrochemical properties, relevance in the literature, and relative maturity among the Li^+ fast-ion conductors, the LLZO garnets were used throughout this dissertation. To fabricate LLZO membranes for use in an electrochemical cell, the LLZO is first synthesized via a solid-state synthesis reaction, densified under the simultaneous application of high temperatures and high pressures, and finally the resulting LLZO membranes are polished to create smooth surfaces. LLZO of two different compositions were used. The first composition of LLZO, which is used in Chapters 3 and 4, is stabilized by the addition of Al^{3+} dopants with a nominal composition of $Li_{6.25}La_3Zr_2Al_{0.25}O_{12}$. The second composition, which is used in Chapters 4 and 5, is stabilized by the addition of a Ta^{5+} dopant with nominal composition of $Li_{6.5}La_3Zr_{1.5}Ta_{0.5}O_{12}$. For both compositions, the starting precursors, Li_2CO_3, La_2O_3, and ZrO_2 are combined with the stabilizing dopant in the form of Al_2O_3 or Ta_2O_5 in stoichiometric amounts. A 5 wt% excess amount of Li is added to the nominal compositions in order to account for Li volatilization during the high temperature processes. The combined powders are then mixed for 20 hrs in ethanol on a roller mill with zirconia grinding media and then dried for at least 6 hrs. The dried powder mixture is then compacted in 10 g batches in a stainless-steel die under a pressure of 35 MPa. The compacted powder disks are then loaded on a MgO furnace-boat and calcined in a tube furnace under a 1.5 L min^{-1} flow of dry air. The tube furnace is heated at a rate of 1.7 °C min^{-1} to a temperature of 1000°C and held for 4 hrs before cooling to room temperature at a rate of 4.0 °C min^{-1}. The resulting powder is then ground in an agate mortar and pestle and sieved through a stainless-steel sieve with 75 µm pores. X-ray diffraction is used to check the phase purity of the calcined powder. Typical powders synthesized with this method contains at least ~80 wt% of cubic LLZO, less than 5 wt% of impurity phases, and the remaining fraction of tetragonal LLZO. Additional heating during densification typically converts the remaining tetragonal phase, after the initial calcination, into the cubic phase, while the impurity phases, typically $La_2Zr_2O_7$ (pyrochlore) and/or Li_2ZrO_3, remain (< 5 wt%) after densification.

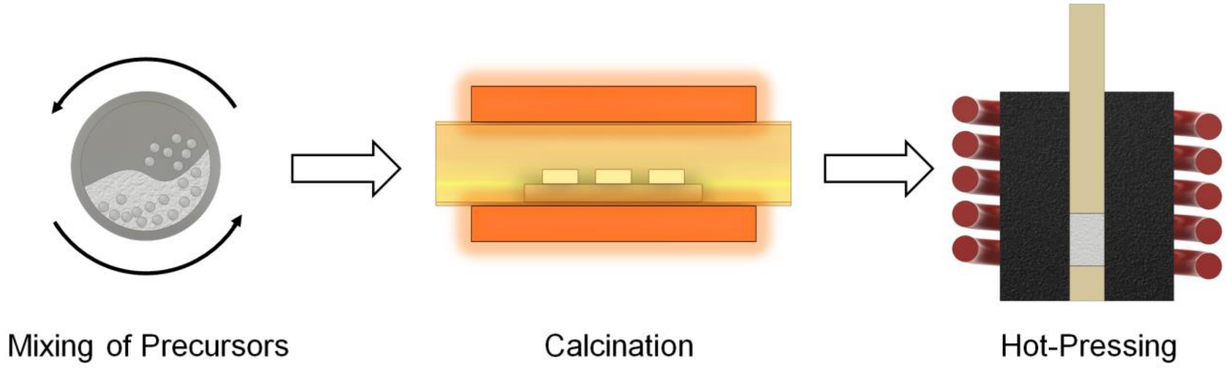

Figure 2.1: Processing of solid-electrolyte materials beginning from solid-state synthesis to densification.

In order to densify the LLZO powder, a rapid-induction hot-pressing technique is used, which utilizes a simultaneous application of high pressures at high temperatures to sinter the material, which allows for the densified materials to have relative densities >95%. The LLZO powder is first compacted in a stainless-steel die under a pressure of 140 MPa and extracted.

The green pellet is then loaded into a graphite die with an alumina anvil and plunger. The LLZO is separated from the alumina by graphite foils, which prevents interdiffusion of Al^{3+}. The die is then loaded to 47 MPa and then rapidly heated at a rate of 225°C min^{-1} by induction heating to a temperature of 1225°C. The die is held at 1225°C and 47 MPa for 40 min before cooling to room temperature at a rate of 41°C min^{-1}. The densified LLZO billet is then cut on a diamond saw to the desired thickness, typically between 1.3 mm and 2.0 mm. The resulting LLZO pellets are then polished beginning with silicon carbide sandpapers between 400 and 1200 grit. After dry-polishing with sandpaper, an automated polisher using a series of diamond pastes is used to achieve a mirror-like surface finish. The pellets are polished using diamond pastes with particle sizes ranging from 15 µm to 0.1 µm using a mineral oil-based polishing fluid and cleaned with ethanol and acetone. The entire synthesis process is illustrated in Figure 2.1.

Na-β”-alumina (NBA) was also used as a model Na^+ fast-ion conductor in this dissertation due to its relative maturity compared to most other solid-electrolytes as well as its desirable electrochemical properties. The NBA electrolytes were provided by our collaborators at the Empa Swiss Federal Laboratories, who synthesized and densified all NBA materials for this dissertation. Spray-dried NBA powder with a Li-stabilized β” phase are prepared by a similar solid-state reaction, using boehmite AlO(OH), LiOH, and Na_2CO_3 precursors. The resulting mixture of powders is then compacted into a green body and loaded into a furnace, using green buffer discs composed of the mother powder to mitigate Na and Li loss and to facilitate shrinkage during sintering. The samples and buffer discs are also encapsulated with a dense magnesium spinel dome and support disk with a constant ratio of NBA mass to encapsulated volume of 0.14 g cm^{-3}. The resulting sintered pellets exhibit relative densities of 97.6% and then are ground and polished using an identical method for that of LLZO.

2.2 Assembly of Symmetric Cells

With the exception of Chapter 5, the majority of this dissertation utilizes a symmetric electrochemical cell, which is composed of two identical electrodes separated by the solid-electrolyte. Given the two electrolytes available, the two configurations would be a Li-LLZO-Li configuration and a Na-NBA-Na configuration. In a symmetric cell, because the electrodes are identical, the cell is essentially a 0 V battery, which has no practical application. However, for studying interface behavior between electrode and electrolyte, the symmetric configuration is a simple method for decoupling anode and cathode behavior. Since only the alkali metal anode is being used, any and all interface phenomena that occurs, can be attributed to the alkali-metal/solid-electrolyte interface.

Before constructing Li/LLZO symmetric cells, the LLZO pellets undergo a heat-treatment which has been demonstrated both experimentally and computationally to decompose Li_2CO_3 and LiOH contamination layers that form on the LLZO surface due to spontaneous reaction with moisture in ambient air. After polishing and cleaning the pellets, the LLZO is loaded into a MgO furnace boat into a muffle furnace housed within an argon-filled glovebox. The heat-treatment consists of heating to 400°C for 3 hrs with heating and cooling rates of 4.2°C min^{-1}. After the heat-treatment, the Li electrodes in the form of 500-750 µm thick foils, are scraped with stainless-steel spatulas to remove native oxides and pressed onto the surface under a pressure of 3.4 MPa. In Chapter 3, 10 µm of Li metal is deposited via thermal evaporation on each side of the LLZO pellet before attaching the foil, in order to maximize the Li/LLZO interfacial contact. After attaching the Li foils, 35 µm Ni foils are used as current collectors and the entire stack is heated at ~170°C under a load of ~1 MPa for ~10-15 hrs, which allows the Li to wet the LLZO surface, improving the interfacial contact. Adhesive polymer masks are also typically used to not only maintain a constant area at the Li/LLZO interface, but also to avoid any variability in microstructure near the electrolyte edges. The assembly process is illustrated in Figure 2.2.

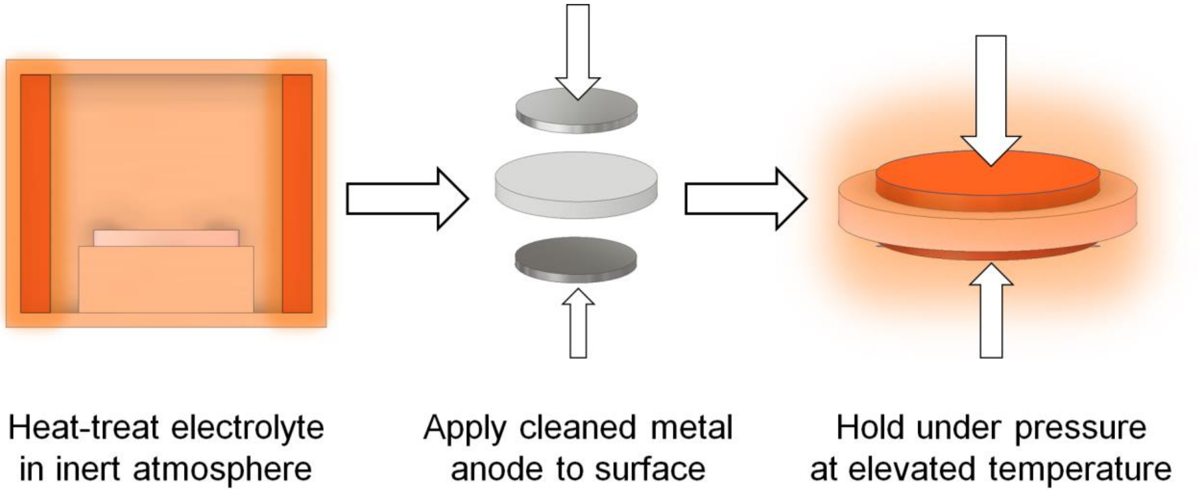

Figure 2.2: Assembly of an electrochemical cell consisting of a ceramic solid-electrolyte and alkali metal electrodes

A similar assembly process is used to construct symmetric Na/NBA cells. Previously, the ability to achieve low interfacial resistances between Na metal and NBA at room temperature has never been reported in the literature. However, using our experience with controlling the LLZO surface chemistry, it has been demonstrated here that a similar heat-treatment method can be used for the NBA electrolyte, resulting in low interfacial resistances at room temperature. This process will be described in detail in Chapter 4. After conducting the described heat-treatment at 900°C for 3 hrs at identical heating and cooling rates as described for LLZO, Na foils 200-500 µm thick are scraped and pressed onto the NBA surface at an identical pressure of 3.4 MPa However, unlike with Li/LLZO, where temperatures near the melting temperature of Li are required for the Li to wet the LLZO surface, it was observed that the Na seems to sufficiently wet the NBA surface at room temperature after the application of 3.4 MPa. Ni foils 35 µm thick are used as current collectors.

2.3 Electrochemical Impedance Spectroscopy

Electrochemical impedance spectroscopy (EIS) is an extremely versatile technique for analyzing solid-state electrochemical systems and is frequently used throughout this dissertation. Within a solid-state electrolyte, there can be several sources of resistance to charge transport. In many cases, ions must move not only through the crystal structure of the electrolyte material, but may need to also traverse grain boundaries, secondary phases, and external interfaces or participate in electrochemical or charge-transfer reactions. All of these phenomena each contribute to the total resistance. However, because the time scales at which the charge transport associated with each of these individual phenomena can occur are distinct and can differ by several orders of magnitude, the resistance associated by individual phenomena can actually be decoupled by measuring the frequency-dependence of the resistance. This is the main advantage of EIS when dealing with solid-state devices.

The preferred method of EIS in this dissertation is potentiostatic electrochemical impedance spectroscopy (PEIS), which uses an AC potential as the input signal. Galvanostatic electrochemical impedance spectroscopy (GEIS) is an analogous technique where the input is an AC current as opposed to an AC potential. A PEIS measurement operates by applying an AC potential signal with constant frequency of the form:

$$V(t) = |V_0|\sin(\omega t)) \tag{2.1}$$

where V is the potential, V_0 is the perturbation voltage, ω is the frequency, and t is the time. Because of the reactance associated with each individual charge transport phenomenon, the resulting current response will have the form:

$$I(t) = |I_0|\sin(\omega t + \varphi) \tag{2.2}$$

where I is the current, I_0 is the current amplitude, and φ is the phase shift. The resulting impedance is then given by the following equation and can be rearranged into the following form:

$$Z = \frac{V(t)}{I(t)} \tag{2.3}$$

By taking advantage of Euler's formula, the impedance Z can then be written in the form:

$$Z = |Z|e^{j\varphi} = Re(Z) + Im(Z) \tag{2.4}$$

where j is the imaginary unit. Measuring the impedance over a range of different frequencies, produces the impedance spectra. Plotting the real and imaginary parts of the impedance at each frequency gives the common form of the Nyquist plot, which will be used throughout this dissertation.

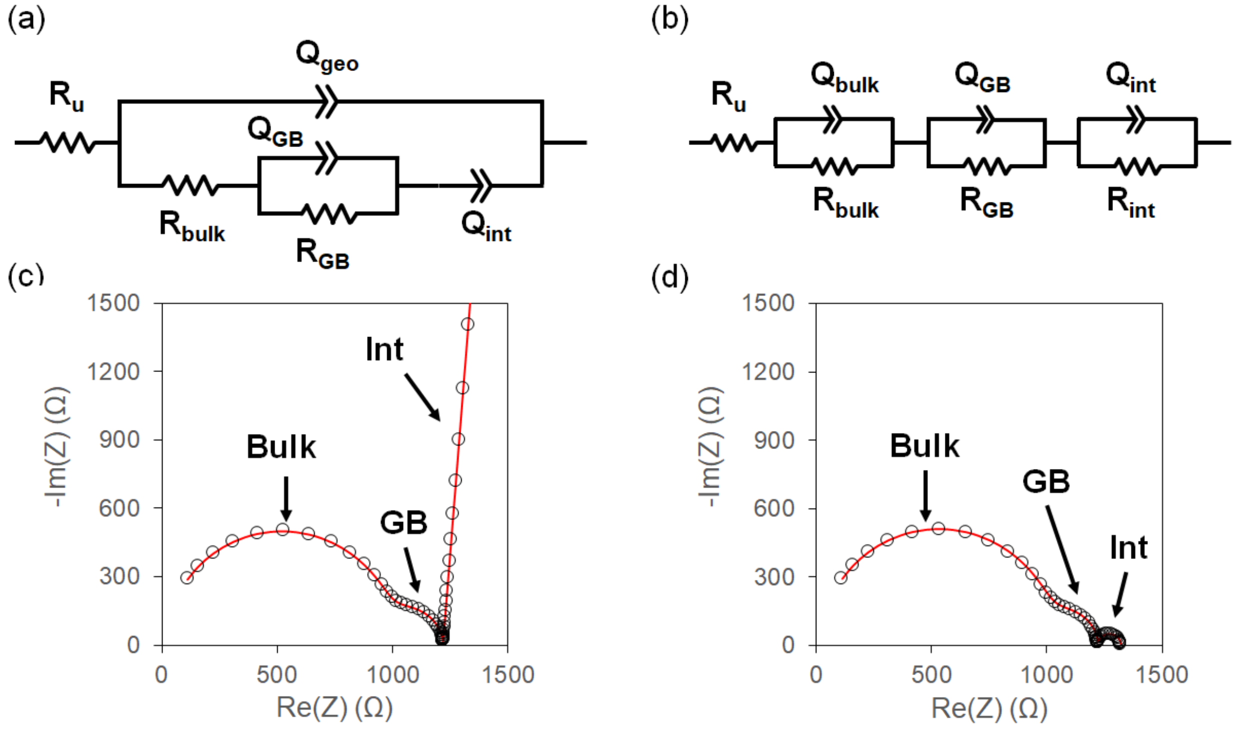

Figure 2.3: Relevant equivalent circuit models and corresponding Nyquist plots. a) Equivalent circuit model for a polycrystalline solid-electrolyte with blocking electrodes. b) Equivalent circuit model for a polycrystalline solid-electrolyte with non-blocking electrodes. c) A representative Nyquist plot for the circuit model in (a). d) A representative Nyquist plot for the circuit model in (b)

For the experiments in this dissertation, EIS is typically conducted at frequencies beginning at 7 MHz and ending at frequencies between 0.1-1 Hz with a perturbation voltage of 10 mV for LLZO and 20 mV for NBA. For polycrystalline oxides, there are two dominant sources of ionic resistance: bulk resistance and grain boundary resistance. Depending on the type of electrodes used, either blocking or non-blocking, the low frequency regime will change. For non-blocking electrodes, there is a third source of resistance which is interfacial, or charge-transfer, resistance. For blocking electrodes, the low frequency regime is dominated by capacitive behavior. In either case, the contribution of each resistance can be decoupled by equivalent circuit modeling. For a blocking configuration, the impedance response is modeled using the circuit model shown in Figure 2.3a, which contains a resistor-capacitor (RC) pair to represent bulk resistance, a second RC element to represent grain boundary resistance, and a capacitor which represents the interfacial capacitance. For a non-blocking configuration, the impedance response is modeled as in Figure 2.3b, which contains three RC elements in series, representing bulk resistance, grain boundary resistance, and interface resistance. In all cases, constant phase elements are used instead of capacitors, which allows for slight variations in time-constants. The resulting Nyquist plots for both circuit models are shown in Figure 2.3c-d. Using these circuit models, the bulk, grain boundary, and interfacial resistances can be measured. Each source of resistance is identifiable by the characteristic capacitance of that particular phenomena, which is 10^{-10}-10^{-12} F, 10^{-8}-10^{-9} F, and 10^{-5}-10^{-6} F for bulk, grain boundary, and interface conduction respectively, according to Irvine *et al*[16]. Resistance associated with experimental hardware is also included by a single resistor, representing the uncompensated resistance.

Chapter 3 Effects of Temperature on Alkali Metal Plating

One of the most challenges significant currently facing solid-state batteries is the ability to achieve charge and discharge rates comparable to Li-ion batteries. As described in Section 1.3.2, one of the challenges of using alkali metal anodes is achieving homogeneous electrodeposition and depletion of the metal, especially at higher current densities. Ostensibly, it has been assumed that a solid-electrolyte should alleviate this issue, as a ceramic electrolyte should act as a rigid boundary, mechanically forcing a dense, uniform electrodeposition growth front of a soft alkali metal. However, while this was originally thought to be one of the key enablers of alkali metal anodes, it has been widely observed that electrodeposition onto an alkali metal anode from a rigid inorganic solid-electrolyte can still be inhomogeneous, and can even cause fracture of the solid-electrolyte[17–19]. This has been widely observed in a number of solid-electrolytes of different compositions, including oxides, sulfides, and polymers[19–26]. Although it is hypothesized that the mechanisms are fundamentally different, this behavior has been likened to the formation of dendrites in classical liquid-based electrodeposition. Once the “dendrite” has formed in the solid-electrolyte, the growth is typically unstable and continues to propagate the “dendrite” across the electrolyte until it reaches the opposite electrode, forming an internal short-circuit. It is still unclear as to what mechanisms govern the initiation and propagation of these metal “dendrites”, however, while the term “dendrite” typically describes a broad range of branched metal morphologies, it is believed that the mechanisms for “dendrite” growth in solid-electrolytes is fundamentally different than the dendrites seen in electrodeposition at liquid/solid interfaces. Therefore, the observed morphologies in solid systems are now referred to as filaments, which generally describes a high aspect ratio electrodeposit. A key observation that was made[27] is that the initiation of metal filaments only occurs when plating above a given current density, now commonly referred to as the critical current density (CCD), although many experimental variables have been demonstrated to affect the CCD of a particular system. These include but are not limited to surface chemistry, charge-transfer kinetics, interface morphology, external operating environment, and electrolyte microstructure[22,27–36]. Because of this phenomenon, the power density and the cycle life of the solid-state battery is fundamentally limited by the CCD of the system and the tendency to irreversibility short-circuit.

In this chapter, the effects of temperature on the CCD is investigated in both the Li/LLZO[29] and the Na/NBA[37] system. Since the first CCD measurement in the Li/LLZO system[27], consistently low CCD values with large variances, in the range of 0.01-1 mA cm^{-2}, have been reported across the literature. It was later hypothesized that the low values and high variance is largely in part due to inhomogeneities in the surface chemistry and subsequent interface resistance and kinetics. The work presented in this chapter leverages recently reported methods of removing resistive surface contaminants on the LLZO surface and vapor deposited pure Li electrodes to reduce and control interface resistance to revisit the correlation between temperature and CCD in Li/LLZO. Additionally, the knowledge gained with the Li/LLZO system enabled CCD measurements of solid-solid Na/NBA interfaces for comparison. Because this work is the first work to demonstrate low interfacial resistances between solid Na metal and NBA, the measurements conducted here represent the first CCD measurements for a room temperature Na/NBA couple. This allows, for the first time, a side-by-side comparison of the cycling behavior of two different alkali-metal/solid-electrolyte interface couples.

The following chapter sections are published in modified forms as:

I. Michael Wang, Jeffrey B. Wolfenstine, & Jeff Sakamoto. Temperature dependent flux balance of the Li/Li7La3Zr2O12 interface. *Electrochim. Acta* **296**, 842–847 (2019).

II. Marie-Claude Bay, Michael Wang, Rabeb Grissa, Meike V.F. Heinz, Jeff Sakamoto, and Corsin Battaglia. Sodium Plating from Na-β″-Alumina Ceramics at Room Temperature, Paving the Way for Fast-Charging All-Solid-State Batteries. *Adv. Energy Mater.* **10**, 1902899 (2020).

3.1 Temperature Dependent Flux Balance of the Li/$Li_7La_3Zr_2O_{12}$ Interface

3.1.1 Introduction

As the demand for safe, high energy density Li-ion batteries continues to increase, all solid state batteries are emerging as a viable candidate to meet the high requirements set for future Li-ion technology[38,39]. In theory, Li metal electrodes can offer drastic improvements in capacity over standard graphite electrodes (with ~40% porosity), having a volumetric capacity 4x greater , assuming an excess 20% volume of Li for mechanical compliance[38,39]. However, from a practical perspective, Li metal has not seen widespread use due to instability against conventional liquid electrolytes, which severely limits the cyclability[38,39]. Solid electrolytes, like the cubic garnet $Li_7La_3Zr_2O_{12}$ (LLZO), have been proposed as an approach to physically stabilize the Li-electrolyte interface. Despite the high shear moduli that ceramics commonly exhibit, like LLZO[40], it has been widely observed that Li can propagate through ceramic separators and lead to short circuits[23,27,35,36,41]. We determined that the propensity for dendrites to propagate and result in short-circuits is known to be dependent on the applied current density. Sharafi *et al.*[27] characterized the maximum sustainable current density without short-circuiting as a function of temperature. This current density is referred to as the critical current density

(CCD). Currently, the highest reported CCD for Al-stabilized LLZO is 0.6 mA cm^{-2} at room temperature[32], however, this is still well below the current density regimes relevant to applications like electric vehicles (>3 mA cm^{-2}). A recent report demonstrated higher CCDs, up to 1mA cm^{-2}, however this study used interfacial coatings and Ta-stabilized LLZO, which has been suggested to have a higher CCD[42]. Although the reported CCDs in the literature have demonstrated significant step-increases over the years, further improvements must be made to enable widespread adoption of LLZO electrolytes. The demand for applications like electric vehicles, which require current densities $\geq$ 3 mA cm^{-2} [43] provides the impetus to better understand and maximize the CCD of the Li/LLZO interface.

Although the mechanisms that govern the CCD are still relatively unknown, in recent years, many variables have been identified that have an impact on the CCD. Some of these factors on the LLZO side include the presence of grain boundaries, grain size, interfacial impedance, and size of surface flaws[23,28,32,41]. These studies have resulted in rapid step increases in the CCD in recent years, however, achieving the goal of $\geq$ 3 mA cm^{-2} continues to be a challenge[43].

In this study, the relationship between CCD and temperature for the LLZO system is revisited, utilizing well-understood processing steps over recent years to eliminate variability from the material, interfaces resistance, and cell preparation. Pressure-assisted densification was used to prepare (>96% r.d.), low and consistent grain boundary resistance Al-stabilized cubic LLZO. Furthermore, the LLZO interfaces were prepared by heat-treating in Ar to achieve chemically clean surfaces that allow for consistently low interfacial impedances, as low as 10 Ω cm^2, compared to >500 Ω cm^2 observed in previous studies[27]. This is a major distinguishing factor, as recent reports have demonstrated clear correlations between interfacial resistance and CCD [28]. The CCD is then studied as a function of cycling temperature and CCDs close to 1 mA cm^{-2}

are demonstrated at room temperature. Furthermore, due to the improvements in the quality of the materials and interfaces, defects that typically limit the CCD can be eliminated and other potential mechanisms for the CCD can be presented here. Unlike past works which studied the role of LLZO on the CCD, it is hypothesized here that the properties of the Li metal electrode may also play an important role in governing the CCD. By identifying the sources of Li flux toward and away (plating vs stripping) from the Li/LLZO interface, the importance of Li transport in the electrode is highlighted. While the properties of the LLZO may still be important, the transport properties of the Li metal may ultimately set the limit on the maximum CCD regardless of the solid electrolyte type or chemistry. Overall, this study presents yet another step increase in the CCD of the Li/LLZO system and provides further insight on the role that the properties of Li metal play in the interface kinetics.

3.1.2 Experimental

3.1.2.1 LLZO synthesis and cell assembly

Al-stabilized cubic LLZO ($Li_{6.25}La_3Zr_2Al_{0.25}O_{12}$) was prepared with a solid-state synthesis technique, using Li_2CO_3 (1 μm, Alfa Aesar, Ward Hill, MA), La_2O_3 (PIDC, Ann Arbor, MI), Al_2O_3 (0.05 μm, Mager, Scientific Inc. Dexter, MI), and ZrO_2 (30–60 nm, Inframat, Advanced Materials, Manchester, CT) as starting precursors. The combined powders were calcined in dry air at 1000°C and then sintered using rapid induction hot-pressing. During the rapid induction hot-pressing process, the powder is rapidly heated (225°C/min) by induction heating to a temperature of 1225°C, while simultaneously under 47 MPa of pressure, and held for 40min before cooling (41°C/min) to room temperature. According to Sharafi *et al.*[32], these processing conditions produce LLZO with an average grain size of 50 μm. The resulting LLZO was cut into pellets of thickness 1.3±0.1 mm with a 12.7 mm diameter and then polished with a series of sandpapers and diamond pastes, to a final polish using 0.1 μm diamond paste. Sandpapers were used to make the pellet faces parallel and then the pellets were polished on a Buehler EcoMet250 automatic polisher using diamond pastes with particle sizes ranging from 15 μm to 0.1 μm (Leco, St. Joseph, MI). A mineral oil-based fluid (Leco, St. Joseph, MI) was used as an extender fluid. The final thickness of the LLZO pellets after polishing was approximately 1.2±0.1mm. Phase purity was confirmed using a Rigaku Miniflex 600 x-ray diffractometer. Before assembling Li/LLZO/Li symmetric cells, the LLZO pellets were heat treated in Ar at 400°C for 3 hrs, as described in Sharafi *et al.*[33], in order to remove surface contaminations without inducing any significant structural changes or grain growth in the LLZO. An initial 10 μm layer of Li metal was then deposited on each side of the LLZO pellet, using an Angstrom Engineering Li evaporator. A 750 μm thick Li foil was pressed on top of the initially evaporated Li layer under a pressure of 3.4 MPa in order to act as a reservoir of Li, preventing total depletion of the initial Li layer during cycling. The Li/LLZO/Li cell was then heated at ~170°C under a load of ~1 MPa for 12 hrs to improve contact between Li and LLZO.

3.1.2.2 Electrochemical characterization

Electrochemical impedance spectroscopy (EIS) was performed in order to measure the ionic conductivity of the cells. EIS was conducted at frequencies between 1 Hz and 7 MHz with a perturbation voltage of 10 mV. A modified version of the model proposed by Huggins was used to model the spectra[44]. The model contains three RC components in series, representing the bulk, grain boundary, and interfacial impedances, however, in this model the capacitors were replaced with constant phase elements (CPE). Features in the EIS spectra were matched to their corresponding physical phenomenon based off of the fitted capacitances, with capacitances of

~10^{-12} F, ~10^{-9} F, and ~10^{-6} F indicative of the bulk, grain boundary, and interface components respectively, as described in depth by Irvine *et al.*[16].

Galvanostatic cycling was conducted in order to determine the dependence of critical current density (CCD) on temperature. CCD measurements were performed for three samples each at 25°C, 40°C, 60°C, 80°C, and 100°C. Cycling was conducted in a load frame under a constant stack pressure of 3.4 MPa. The cells were then cycled at increasing current densities, passing 0.2 mAh cm^{-2} of charge each cycle. EIS was conducted between each charge/discharge cycle. The CCD was defined by the current at which both a drastic drop in the potential is observed, as well as a change in the impedance behavior from an ionic conductor to a pure resistor.

3.1.3 Results and Discussion

3.1.3.1 Materials and electrochemical characterization

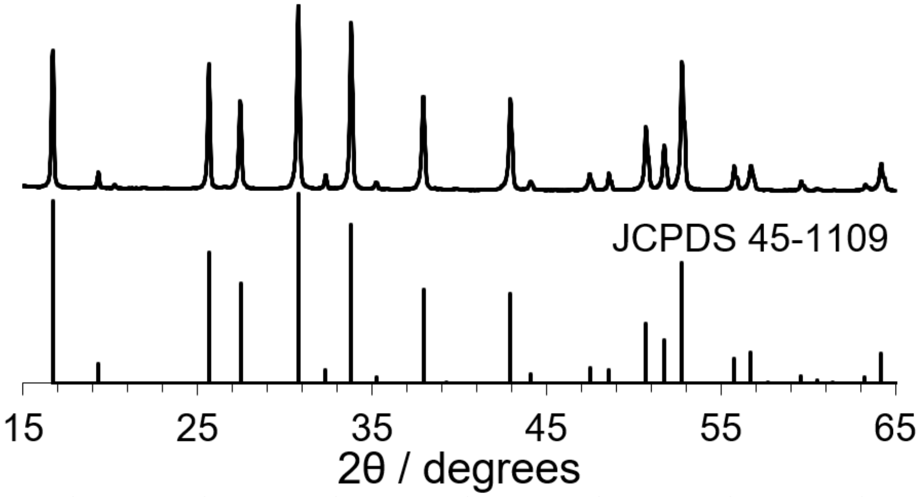

Figure 3.1: XRD spectra for the hot-pressed LLZO pellet. A reference for cubic garnet is provided.

Figure 3.1 depicts the XRD spectra for a representative LLZO pellet. XRD measurements were conducted before cell assembly to confirm that the LLZO is phase pure cubic garnet with minimal impurities (<5 wt%). EIS was used to investigate the temperature dependence of the resistances of each component in the Li/LLZO/Li cell. The EIS spectra were fitted using an equivalent circuit based off of the Huggins model, using constant phase elements instead of capacitors. The spectra were fit to the model shown in Figure 3.2 and each portion of the spectra was ascribed to a particular physical phenomenon based off the capacitance value, with 10^{-12} F, 10^{-9} F, and 10^{-6} F, corresponding to the bulk, grain boundary, and interface resistances, respectively. The measured resistance at a variety of temperatures is depicted in an Arrhenius plot shown in Figure 3.2. Measurements were not made above 65°C because the magnitude of the grain boundary and interfacial resistances were too low to accurately measure. Based off the Arrhenius equation the activation energy for Li^+ conduction through the bulk, grain boundaries, and interface were calculated to be 0.36, 0.46, and 0.47 eV respectively.

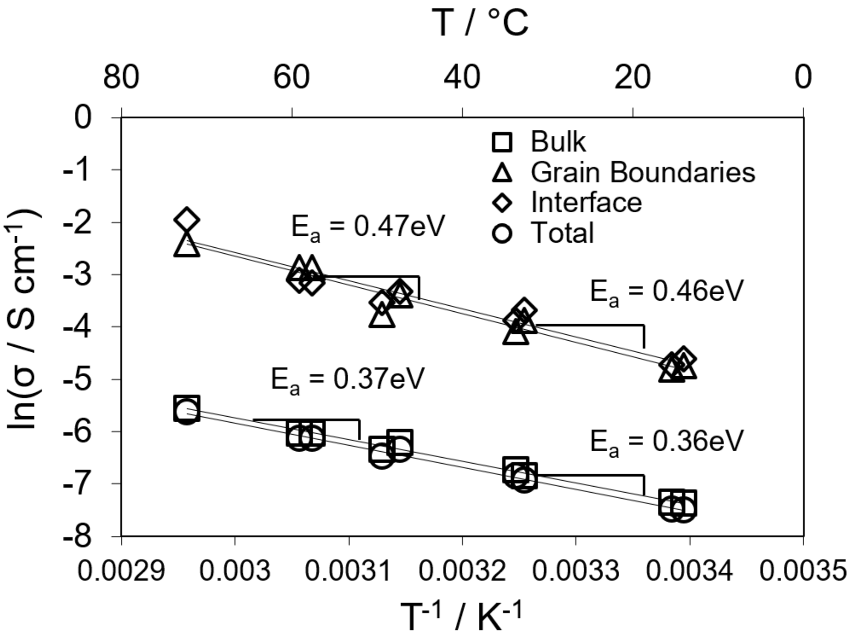

Figure 3.2: Conductivity as a function of a temperature calculated from the bulk, grain boundary, and interface resistances of the Li/LLZO/Li cell. The resistance value of each component was obtained by equivalent circuit modeling of the measured Nyquist plot at each temperature.

Figure 3.3a shows the potential response of a symmetric Li/LLZO/Li cell undergoing galvanostatic cycling at increasing current densities. The point at which the potential drops to 0 V is typically defined as the CCD or when Li metal filaments form a short-circuit between electrodes. Figure 3.3c shows the EIS spectra of the cell before cycling, before shorting, and after shorting. The shorting observed in the potential response is supported by the abrupt change in the EIS spectra. Before shorting, the EIS spectra is characterized by its distinct semicircular features, representative of an ionic conductor. After shorting, the impedance spectrum exhibits predominantly resistive behavior and some inductive behavior which is a clear indication of an electrical short circuit between the two Li electrodes. It has been previously suggested that the interfacial resistance may have a major impact on the CCD and that high interfacial resistances may lead to non-uniform current densities across the interfacial area[27,45]. In order to minimize the effects of interfacial resistance, the LLZO pellets were heat-treated which allows for near negligible interfacial resistances. Before cycling, EIS was performed on each sample at room temperature, and the average interfacial resistance was measured to be ~10 Ω cm^2.

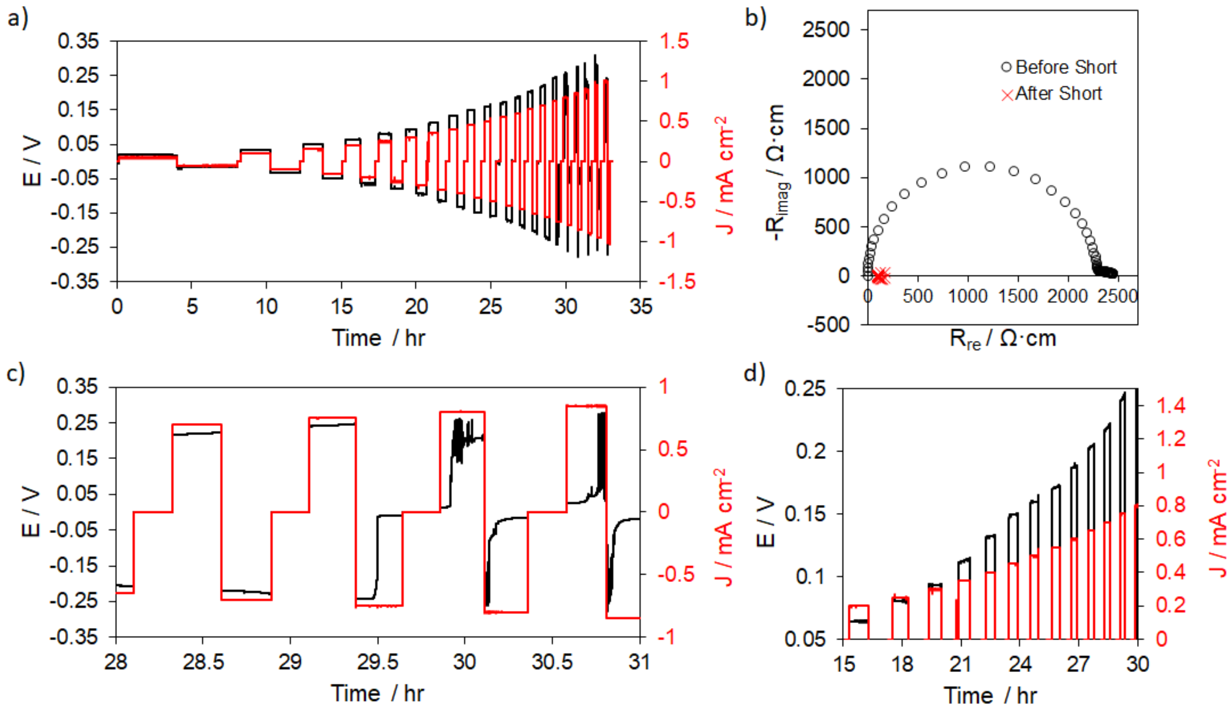

Figure 3.3: a) Representative potential response of a Li/LLZO/Li cell undergoing a CCD measurement and b) representative EIS spectra before and after the shorting condition. c) Potential response near the

CCD. Arrows indicate the drop in potential corresponding to the short circuit and the erratic behavior following the short. d) Polarization of the cell tends to increase as the magnitude of the applied current increases.

Galvanostatic cycling was performed at five different temperatures and the corresponding CCDs are plotted as a function of temperature in Figure 3.4. The averages and standard deviations for the CCDs are also listed in Figure 3.4c. When plotted as a function of temperature, an exponential relationship is observed between temperature and CCD, which is in good agreement with previous studies on LLZO[27]. However, in previous studies, the magnitudes of the interfacial resistance are significantly higher, up to 500 Ω cm^2 [27], which may lead to localized areas of higher current densities, previously referred to as "hot-spots". Since the interfacial resistances in this study are orders of magnitude lower, it is likely that the localization of current density from surface inhomogeneities is less drastic and the current is more evenly distributed over the interface. In both previous studies as well as this study, it is likely that the failure point is reached at the same current density, however, due to "hot-spots", these current densities are only reached at specific areas, while the average current density remains low. The average current densities reported here may be more representative of the localized current densities at "hot-spots" in these previous studies, since there should be a more even distribution of current over the interface. We believe that by achieving low Li/LLZO interface resistance, it can be assumed that there is a relatively uniform current density, which results in higher CCDs than previous studies have reported. Although not explicitly measured in each study, based off of the processing conditions, it is likely that the LLZO grain size in the referenced studies in Figure 3.4 are generally smaller than the grain size in this study. As demonstrated by Sharafi *et al*.[32], this may increase the number of potential nucleation sites for Li filaments since it has been observed that Li preferentially propagates along grain boundaries. This hypothesis has also been suggested by others based on the mechanics and chemistry of Li at the grain boundaries[20,46,47]. At room temperature, the CCD is nearly ~1mA cm^{-2} without any evidence of short circuiting in the EIS spectra. Figure 3.4 also highlights the deviation from ohmic behavior as the applied current density approaches the CCD. Well below the CCD, the potential response is ohmic and stable and as the current approaches the CCD, the potential begins to increase linearly as soon as the current is applied. This phenomena has been commonly observed and it has been suggested that it is the result of the inhomogeneous distribution of Li at the interface due to the stripping and plating of metallic Li[45]. However, the impact of polarization near the CCD on cell failure will likely require the usage of a reference electrode in order to fully understand.

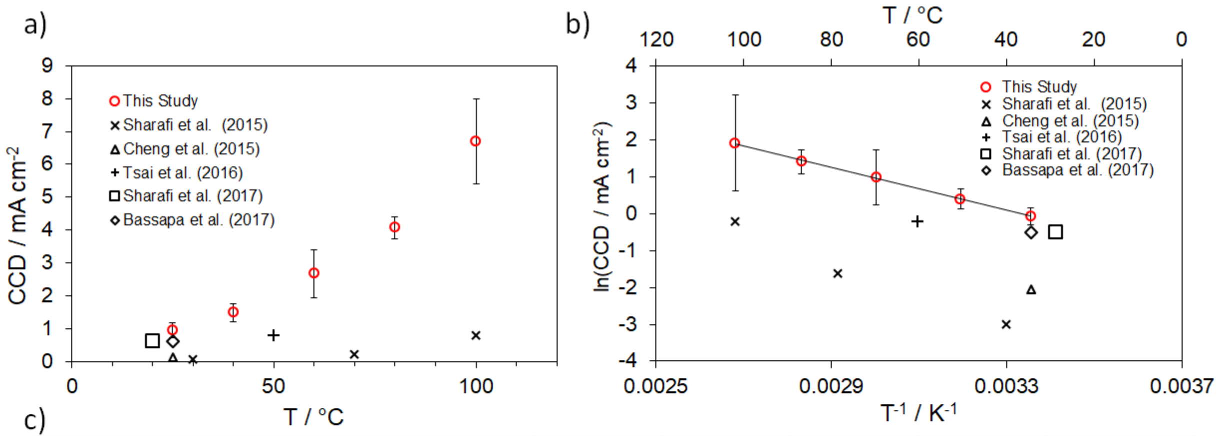

c)

Temperature	25°C	40°C	60°C	80°C	100°C
Average CCD ($mA \cdot cm^{-2}$)	0.93	1.48	2.67	4.07	6.70
Standard Dev. ($mA \cdot cm^{-2}$)	0.24	0.24	0.70	0.31	1.21

Figure 3.4: a) CCD as a function of temperature and b) Arrhenius plot of CCD. Reported CCDs from the literature are plotted for comparison[4,6–9]. c) Averages and standard deviations for CCDs as a function of temperature.

3.1.3.2 Relationship between CCD and temperature

It has been demonstrated in this study as well as previous studies that the CCD is exponentially related to the temperature, but currently this relationship is not well understood. The CCD has been defined as the maximum current density above which there is a transition to an unstable plating regime where the Li develops highly non-uniform morphologies such as dendrites or filaments. The analogy in a liquid electrolyte is the limiting current density, above which a diffusion-limited region forms and the lack of mass transport at the interface causes highly localized plating and dendrite formation[48,49]. However, the observation of classical dendrite growth in both polycrystalline and single crystalline LLZO, as well as the exponential relationship between CCD and temperature, suggests that the mechanism in a solid-state system may be similar to a liquid system[48,49]. The observation of Li filament growth in single crystal LLZO[23,34] is particularly interesting as it suggests that the presence of grain boundaries may facilitate Li propagation but are not an absolute requirement. Given that the limiting current in liquid systems is governed by mass transport limitations near the electrolyte/electrode interface, it may be necessary to analyze the mass transport phenomena near the Li/LLZO interface as well.

Using the Nernst-Einstein relation (Equation 3.1), the diffusion coefficient of Li^+ in LLZO is estimated to be 2.15×10^{-9} cm^2 s^{-1}, which is two orders of magnitude higher than the self diffusion coefficient of metallic Li, reported to be 5.6×10^{-11} cm^2 s^{-1} [50].

$$D_{Li}^{LLZO} = \sigma_{Li}^{LLZO} \frac{kT}{c_{Li} z_{Li}^2 e^2} \qquad (3.1)$$

The calculated diffusion coefficients for Li in LLZO is compared to the diffusion coefficients reported by Lodding *et al.*[51] (Figure 3.5). It can be seen that the diffusion coefficient in LLZO is greater than the self diffusion coefficient of metallic Li well within the range of standard operating temperatures.

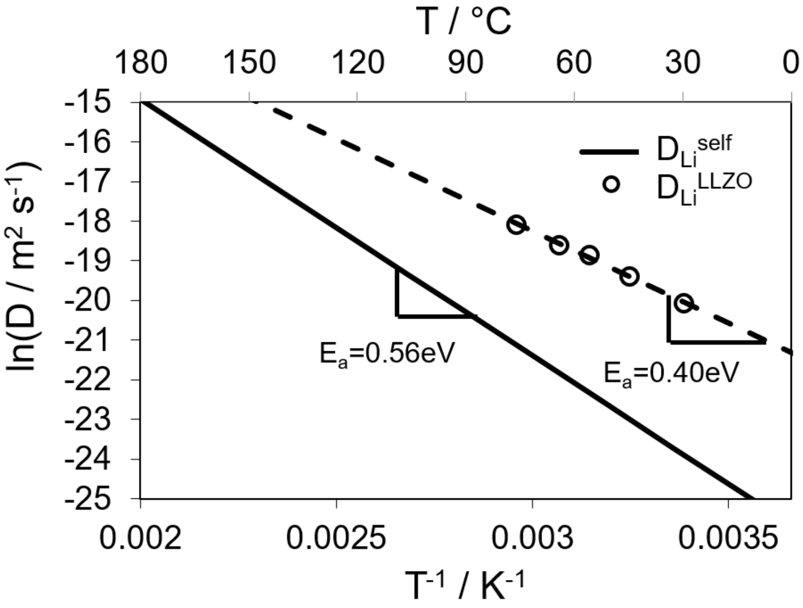

Figure 3.5: The calculated diffusivity of Li in LLZO calculated from the Nernst-Einstein equation. The self diffusivity of Li is shown for comparison[51].

The significant difference in the transport properties of Li^0 in the Li electrode and the Li^+ in LLZO imply that the flux of plated Li away from the interface and into the electrode may be the rate-limiting step that governs the CCD. Figure 3.6 shows a schematic of the different transport phenomena close to the interface of the Li metal and LLZO under different applied current conditions. Taking advantage of the fact that the ionic transference number of LLZO is near unity, it can be assumed that all of the current in the LLZO is generated by Li^+ transport. Furthermore, since the current density is fixed by the experimental setup, the migration flux is constant. This flux of Li^+ migrating from the LLZO toward the Li interface is given by:

$$J_m = \frac{j}{e} \tag{3.2}$$

Meanwhile, there is also a flux of Li metal away from the interface caused by diffusion, as well as creep (assuming a non-zero stack pressure):

$$J_a = J_{creep} + J_{diff} \tag{3.3}$$

At low current densities, the migration flux of Li^+ toward the interface is relatively small ($J_m << J_a$), such that the flux of Li^0 away from the interface is sufficiently fast to maintain a planar geometry. For example, as one Li atom is plated, the flux of Li away from the interface is sufficiently fast to transport the plated Li atom away from the interface and create another "vacant site" for a new Li to plate while maintaining a planar geometry (Figure 3.6). However, at high current densities, the flux of migrating Li^+ toward the interface is much greater than the flux of Li^0 away from the interface ($J_m >> J_a$). Since there are a finite number of vacant sites for Li deposition to occur per unit area, the "vacant sites" are quickly depleted as the flux from diffusion and creep are insufficiently fast to replenish them. In this case, as a Li atom is plated, the creep and diffusion are not fast enough to move the plated Li into the bulk before another Li atom is plated. Since there are no "vacant sites" left for plating that would maintain a planar geometry, the subsequent Li atoms are forced to plate on "non-planar" sites and eventually result in Li^0 pile-up. These pile-ups are localized curvatures on the surface which act as the nuclei for unstable growth fronts. Similar to dendritic growth in liquid systems, these non-planar growth fronts transition to a regime of unstable plating once a critical "hot-spot" size is formed. However, as opposed to the classical liquid systems, in the solid-state systems, the transport limitations exist within the electrode rather than the electrolyte. Furthermore, a recent finding by Masias *et al.*[52] suggests that a region of hydrostatic compression could be generated within the Li metal at and adjacent to the Li/LLZO interface, due to the balance of adhesive forces and stack pressure Moreover, it was determined that the deformation of Li was controlled by power law creep, under relevant stack pressures. This could suggest that temperature dependent dislocation motion manifests in the correlation between temperature and CCD.   It is possible that hydrostatic compressive regions effectively harden Li, thereby affecting the mechanical behavior of the Li/LLZO interface. Aside from decreasing the dislocation creep rate, this is likely to decrease the self-diffusivity in that region, as it has been shown to do by an order of magnitude in other metals like Na and In[53,54]. These additional forces may further hinder the mass transport required to maintain stable plating morphologies. In order to maintain a constant nominal potential, the region near the Li pile-up will polarize, resulting in "hot-spots" that have been alluded to in the literature. These "hot-spots" may be a result of the increased charge density surrounding the Li-pileups, which changes the local potential at the Li-electrolyte interface. The onset of Li metal penetration into the electrolyte could be triggered by these localized regions of high overpotential.

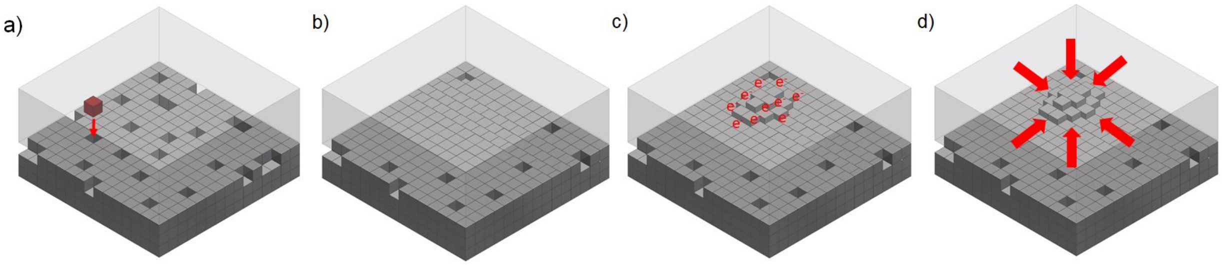

Figure 3.6: a) Schematic of Li^+ plating in a vacant surface site at the Li/LLZO interface. b) Near the CCD, diffusivity is insufficiently fast enough to maintain an adequate number of vacant sites at the surface c) At high current densities, Li^+ is forced to plate on already occupied sites leading to "hot-spots" with increased electron density. d) Hydrostatic compression in the Li metal as suggested by Masias *et al.*[52] may impede Li transport and expedite "hot-spot" formation.

3.1.3.3 Comparison of reported CCDs

Figure 3.4 also plots the reported CCDs for LLZO from various other studies[27,32,35,36,41]. If diffusion kinetics were the sole mechanism for CCD, then it would be expected that all of the reported CCDs would be very similar and follow the same trends, but this is clearly not the case. The two most prominent variables across these various studies are: 1) LLZO microstructure and 2) interfacial resistance. As previously reported by Cheng *et al.* and Sharafi *et al.*, Li metal has been observed to propagate along the grain boundaries, and therefore the CCD is greatly impacted by the LLZO grain size. However, as Porz *et al.* demonstrated, even in single crystal

LLZO, it is still possible to transgranularly propagate Li metal. Therefore, it could be that in polycrystalline LLZO, the point where grain boundaries meet the interface act as a preexisting nucleus where spherical rather than planar diffusion magnifies the net Li transport towards these surfaces. It may also be possible that the Li^+ flux is particularly fast at defects such as grain boundaries, leading to faster growth of a diffusion-limited region. In this case, the condition where $J_m >> J_a$ will be first met at the intersection of the grain boundary and the Li/LLZO interface. This would result in Li pile-ups to preferentially form and propagate at the grain boundaries.

One of the biggest differences between the many studies is the magnitude of the interfacial impedance, as it is clear that the CCD is inversely related to interfacial impedance. Moreover, as the measured interfacial impedance decreases, the magnitude of variation in impedance across the Li-solid electrolyte interface likely decreases. Given that the migration flux of Li^+ toward the interface is independent of interfacial resistance, it suggests that the onset of Li metal penetration may be governed by a critical overpotential rather than a critical current density. Since the overpotential is correlated to the current density by the exchange current density, the variations in interfacial resistance (hot spots) may be the result of variations in the exchange current density. The exchange current density, the measure of the equilibrium rate of charge transfer, is likely to vary based on differences in electrode-electrolyte contact, morphology of surface features, and spatial variations in electron density[55]. The rate of charge transfer at solid-solid interfaces in particular has been known to be heavily influenced by surface defects and lattice imperfections near the surface[55]. As previously suggested, regions of Li pile-up may create “hot-spots” which may locally increase the electron density and/or lead to a mechanical stress, which creates an energy term that manifests in an overpotential. These ideas have been described for the Na-β alumina system[56,57] and the latter more recently for the LLZO system[23,34]. However, the concept of a critical overpotential again necessitates the usage of a reference electrode in order to understand its impact on cycling performance. Moreover, if the overpotential is the root cause of failure, quantifying the overpotential is necessary to better understand what enables propagation of Li metal through ceramic electrolytes.

3.1.4 Conclusions

In this study, the relationship between critical current density and temperature at the Li/LLZO interface was revisited. Using recently developed methods for achieving consistently low interfacial resistance at the Li/LLZO interface, it was observed that current densities near 1mA cm^{-2} could be achieved at room temperature and near 7mA cm^{-2} at 100°C before short-circuiting. Furthermore, the role of Li transport at the interface was examined. Using the Nernst-Einstein relation, it was determined that the self diffusion of Li metal is slower than the diffusion of Li^+ in the LLZO electrolyte. By analyzing the flux balance of Li at the interface, it was hypothesized that the slow self diffusion of Li may play an important role in determining the maximum current that can be cycled in the Li/LLZO system. It was suggested that at high current densities, the flux of Li^+ ions toward the interface greatly exceeds the flux of Li^0 away from the interface due to diffusion and creep. The build-up of metallic Li due to slow diffusion may act as “hot-spots” that magnify the local overpotentials at the interface. Although there are still many other factors that may impact the CCD in real systems, the hypothesis presented here emphasizes the need to examine the role of the Li electrode in governing the CCD. Overall, the data presented here offers an optimistic improvement for the rate capabilities in the Li/LLZO system and represents another step closer toward the viability of high energy density batteries using Li metal electrodes.

3.2 Sodium Plating from Na-β″-Alumina Ceramics at Room Temperature, Paving the Way for Fast-Charging All-Solid-State Batteries

3.2.1 Introduction

Enabling reversible stripping and plating of alkali metals at current densities >10 mA cm^{-2} at room temperature is key for enabling next-generation batteries with an energy and power density surpassing that of established battery technologies. However, repeated cycling of a lithium metal anode in a liquid electrolyte leads to the formation of lithium metal dendrites that short-circuit the cell and constitute a serious safety hazard.[58] A similar phenomenon is observed in solid electrolytes employed in all-solid-state batteries, where lithium metal tends to deposit inside the electrolyte upon repeated cycling resulting ultimately in a short circuit between anode and cathode.[20,21,23,24]

While the underlying mechanisms are still under debate, it was shown that the critical current density (CCD) for dendrite formation is related to the interfacial resistance between solid electrolyte and the metal anode[33]. Several strategies have been adopted to reduce the interfacial resistance, e.g. at the interface between a $Li_7La_3Zr_2O_{12}$ (LLZO) electrolyte and a lithium metal anode. LLZO is currently investigated intensively because of its high ionic conductivity (~1 mS cm^{-1} at room temperature) and high stability towards lithium metal.[59,60] Strategies include the use of interfacial layers (e.g. Au,[35] Ge[61]), heat treatments to remove surface contamination from the electrolyte,[33] or promoting contact by pressurizing the cell during cycling.[62,63] Despite obtaining interfacial resistances comparable to values measured for the interface between a liquid electrolyte and lithium metal, CCD values remain far below fast charging requirements (e.g. 10 mA cm^{-2} corresponding to an areal charge capacity of 5 mAh cm^{-2} charged/discharged at 2C[64]).

In this study, we investigate Na-β”-alumina ceramics as electrolyte candidate for fast-charging all-solid-state batteries. Owing to its high ionic conductivity, low electronic conductivity, and stability against sodium metal, Na-β”-alumina is already commercially employed in high-temperature sodium-nickel-chloride (NaNiCl) and sodium-sulfur (NaS) batteries operating near 300 °C.[65–67] However, high interfacial resistance, possibly associated with poor sodium wetting and the presence of surface impurities, has impeded its use as solid electrolyte for room-temperature batteries.[30,66]

Here we show that by applying a heat treatment in argon atmosphere to a finely polished Na-β”-alumina surface, a low interfacial resistance to sodium metal <10 Ωcm^2 can be achieved, enabling CCD values of 12 mA cm^{-2} at room temperature fulfilling fast charging requirements. We also investigate the dependence of the CCD values on the total charge transferred. Compared to LLZO, we observe a tenfold increase in current density despite similar transference numbers. We are also discussing the critical role of the electronic conductivity of the electrolyte and the melting temperature of the alkali metal on the CCD.

3.2.2 Experimental Section

Spray-dried Li-stabilized Na-β”-alumina powders were prepared by solid-state synthesis from boehmite (AlO(OH)), lithium hydroxide (LiOH), and sodium carbonate (Na_2CO_3)[68]. Powders were pressed into green bodies of 15 mm diameter. These were sintered for 5 min at 1600 °C in static air in a high-temperature laboratory furnace (Carbolite Gero HTF 1700) applying constant heating and cooling rates of 3 °C min^{-1}. To mitigate sodium (and lithium) loss and to facilitate shrinkage during sintering, samples were placed on green buffer discs made from the same Na-β”-alumina powder. Samples and buffer discs were encapsulated within a dense magnesium-spinel dome and a corresponding magnesium-spinel support disc with a constant ratio of Na-β”-alumina mass (samples plus buffer disc) to encapsulated volume of 0.14 g cm^{-3}. Pellets of relative density of 97.6 ± 0.1 % were obtained. The pellets were then ground plan-parallel with increasingly finer sandpapers and polished with a succession of diamond pastes to a final polish using 0.1 µm diamond paste. Scanning electron microscopy analysis revealed homogeneous grain size distribution in the µm range and a bimodal pore size distribution with coarse pores of 10s of µm diameter and small pores in the sub-µm range (see SEM images in Figure S6). A detailed compositional and microstructural study was reported by some of us.[28] The resulting pellets had final dimensions of 1.4 ± 0.3 mm thickness and 12.7 mm diameter. The samples were then heat treated in argon atmosphere for 3 h at temperatures between 400 and 900 °C.

Cell assembly and electrochemical characterization were performed under argon atmosphere in a glovebox. The heat-treated Na-β”-alumina ceramics were first masked on both sides to an area of 0.49 cm^2 using polyimide foil. Mechanically cleaned sodium foils were then pressed onto both sides of the masked pellets at a pressure of 3.4 MPa. Electrochemical characterization was performed using a Biologic VMP-300 galvanostat/potentiostat using nickel current collectors at a pressure of 3.4 MPa in an argon glovebox. The temperature-dependent ion-conductivity of Na-β”-alumina was extracted from potentiostatic electrochemical impedance spectroscopy (PEIS) data measured at frequencies between 0.5 Hz and 7 MHz with a 20 mV sinusoidal amplitude. Measurements at frequencies > 1 MHz were not taken into account for the fitting. The temperature-dependent electronic conductivity was determined by a DC polarization method (Mott-Schottky) at 0.2 V vs Na/Na^+ after 12 h stabilization (1 V was applied for the measurement at 0 °C due to resolution limits) using a sputtered Ni working electrode and a Na counter electrode. The assessment of the critical current density (CCD) was performed by galvanostatic measurements applying an initial pressure of 3.4 MPa. The current density was increased at each cycle while transferring a constant charge of 0.25 mAh cm^{-2} or 3 mAh cm^{-2}. PEIS was conducted before and after each plating and stripping cycle. CCD was defined as the current density when short-circuit of the cell occurred, indicated by a sudden drop in potential response and cell impedance. CCD values are given as the average over 3 to 4 measurements and the error bars represent the maximum and minimum values.

X-ray photoelectron spectroscopy (XPS) measurements were performed at room temperature on a PHI Quantum 2000 using a monochromated Al Kα X-ray source (1486.6 eV) with a pass energy of 30 eV. All measurements were conducted on three different areas, 150 µm in diameter, of each sample. Sample charging was prevented by charge compensation provided by a low energy electron and an argon ion gun. XPS data were processed with the CasaXPS software. Spectra were calibrated by setting the hydrocarbon component of the C 1s photoemission peak to 285.0 eV binding energy.

3.2.3 Results and Discussion

3.2.3.1 Impact of heat treatment temperature on interfacial resistance and interface chemistry

To study the impact of a heat treatment on the interfacial resistance (R_{int}) between sodium metal and Na-β”-alumina, potentiostatic electrochemical impedance spectroscopy (PEIS) measurements were conducted on Na-β”-alumina pellets heat treated in argon at temperatures between 400 and 900 °C and compared to as-polished untreated samples. These measurements were performed on symmetric Na/Na-β”-alumina/Na cells as depicted in Figure 3.7a. A mask was applied on Na-β”-alumina to obtain a well-defined contact area between Na-β"-alumina and the Na disc and a pressure of 3.4 MPa was applied during PEIS measurements. Representative Nyquist plots for the various heat-treatment conditions are shown in Figure 3.7b. The PEIS spectra reveal two semi-circles representing the impedance contributions from the Na-β”-alumina ceramic characterized by an apex frequency of 4.3×10^5 Hz and from the Na/Na-β”-alumina interface characterized by an apex frequency ranging from 10 to 400 Hz. While the Na-β”-alumina contribution remains constant, the interface contribution is drastically reduced with increasing heat-treatment temperature. To quantify the change in interfacial resistance with the heat-treatment temperature, the PEIS spectra were fitted with two parallel R/CPE circuits in series together with an additional resistance (R_{uc}) to account for any uncompensated resistances e.g. from the cell casing and electrical connections (Figure 3.7a). The interfacial resistances were normalized by the mask area and divided by two because of the two interfaces measured. The results of the fits are presented in Table 3.1 and in Figure 3.7c in a semi-logarithmic scale as a function of the heat-treatment temperature. A significant decrease of the interfacial resistance from tens of thousands of Ωcm^2 for non-heat-treated samples to 8 Ωcm^2 is achieved by heat treating the Na-β”-alumina pellets at 900 °C, while the CPE values increases by two orders of magnitude. Heat treating Na-β”-alumina ceramics in argon atmosphere represents thus a very effective method to reduce the interfacial resistance to sodium metal.

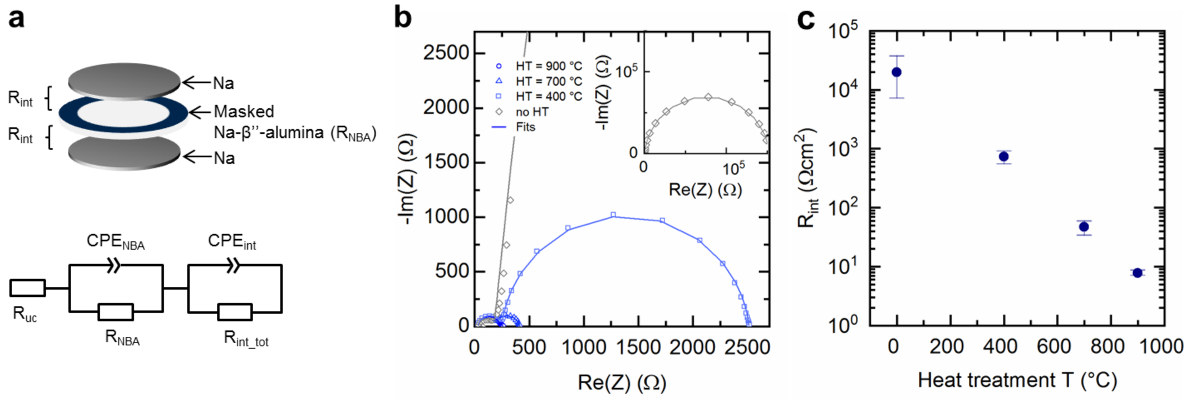

Figure 3.7 Impact of heat-treatment (HT) temperature on interfacial resistance at room temperature. (a) Schematic of the symmetric Na/Na-β”-alumina/Na cell and equivalent circuit for fitting the impedance spectra. (b) Representative Nyquist plots for the different heat-treatment temperatures. Markers represent experimental data and lines represent the fitted data. (c) Interfacial resistance as a function of heat-treatment temperature.

Table 3.1: Fitting results of room temperature interfacial resistance (R_{int}) and capacitance (CPE_{int}) for the various heat-treatment (HT) conditions.

HT [°C]	R_{int} [Ω cm^2]	CPE_{int} [F s^{a-1}]
None	19909	2.7·10-7
400 °C	735	4.1·10-7
700 °C	47	1.4·10-6
900 °C	8	1.8·10-5

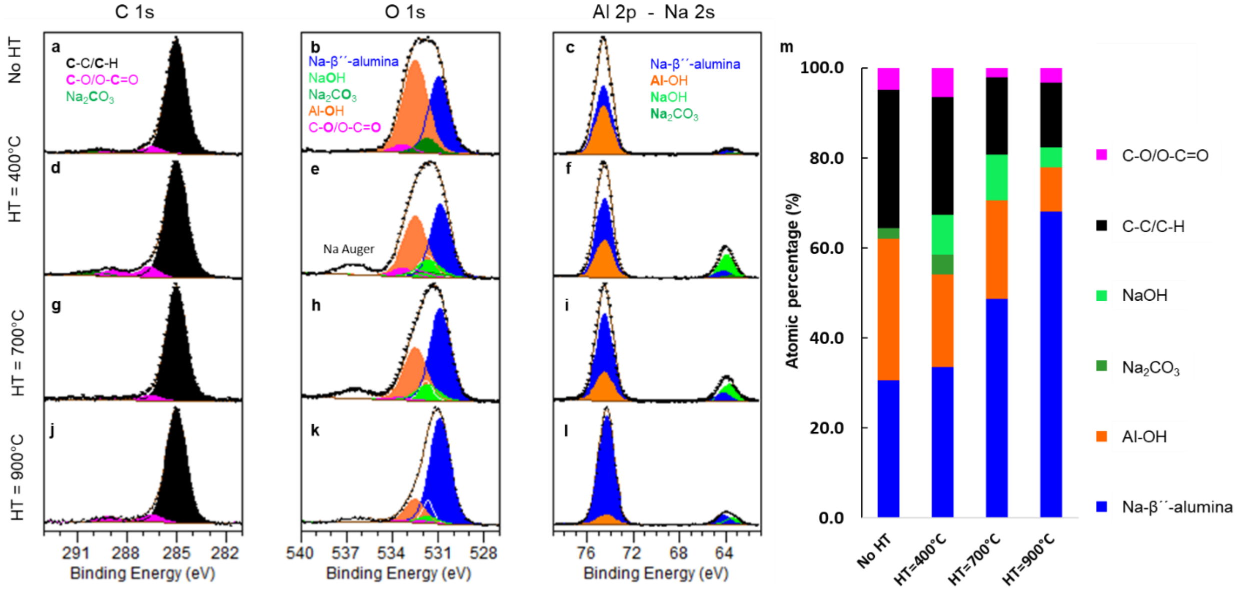

Figure 3.8: XPS analysis of Na-β"-alumina surfaces before and after heat treatment. XPS spectra of C 1s, O 1s and Al 2p-Na 2s core levels of the Na-β"-alumina before heat treatment (a-c), and after heat treatment under argon atmosphere at 400 °C (d-f), at 700 °C (g-i), and at 900 °C (j-l), respectively. Summary of surface chemical composition, estimated by XPS, for all Na-β"-alumina samples (m).

To investigate the effect of the heat treatment on the Na-β"-alumina electrolyte surface, we performed XPS on Na-β"-alumina pellets before and after heat treatment at 400, 700, and 900 °C. Spectra of the C 1s, O 1s, Al 2p, and Na 2s core levels are shown in Figure 3.8. The detailed XPS results are summarized in Figure 3.8m and Table 3.2. The main peak in the C 1s spectra at 285.0 eV (by calibration) is attributed to adventitious carbon species (C-C/C-H). Oxidized carbon contamination (C-O and O-C=O) is detected at higher binding energies. Only a very small amount of Na_2CO_3 (<5 atomic %) is detected at the surface above 289.9 eV before and after heat treatment at 400 °C and is no longer detected after heat treatment at higher temperatures.

Table 3.2: XPS quantification data for the Na-β"-alumina samples before and after heat treatment at Ar atmosphere at 400, 700 and 900 °C.

		Na-β"-alumina No HAT		Na-β"-alumina HT=400°C		Na-β"-alumina HT=700°C		Na-β"-alumina HT=900°C		
Orbital		B.E. (eV)	Atomic %	B.E. (eV)	Atomic %	B.E. (eV)	Atomic %	B.E. (eV)	Atomic %	Peaks assignments
C 1s		285.0	31.0	285.0	27.0	285.0	17.6	285.0	15.1	**C**-C/**C**-H (contamination)
C 1s **Total C**		286.5	1.7	286.6	2.0	286.5	0.8	286.5	1.0	**C**-O (contamination)
		289.1	0.4	288.7	1.4	288.9	0.3	289.1	0.7	O-**C**=O (contamination)
		289.9	0.8	289.9	0.8	__	0.0	__	0.0	$Na_2\mathbf{C}O_3$
			33.9		**31.2**		**18.7**		**16.7**	
O 1s		531.0	16.3	530.8	16.0	530.9	26.1	530.9	37.2	**O** (Na-β"-Alumina)
O 1s **Total O**				531.6	4.6	531.7	5.2	531.7	2.3	Na**O**H
O 1s		531.7	3.1	531.8	2.2	__	0.0	__	0.0	$Na_2C\mathbf{O}_3$
O 1s **Total O** Al 2p		__	0.0	532.4	1.8	532.4	0.3	532.0	0.7	C=**O**
		532.5	23.7	532.5	14.7	532.5	16.3	532.5	7.8	Al-**O**H
		533.3	1.6	533.3	1.9	533.5	0.8	533.3	0.9	C-**O**
			44.6		**41.2**		**48.6**		**48.9**	
	Al $\mathbf{2p_{3/2}}$	74.1	5.5	74.2	8.4	74.2	12.1	74.1	17.2	**Al** (Na-β"-Alumina)
Al 2p **Total Al**	**Al** $\mathbf{2p_{1/2}}$	74.7	2.7	74.9	4.2	74.8	6.1	74.8	8.6	
Al 2p	**Al** $\mathbf{2p_{3/2}}$	74.6	7.5	74.6	4.4	74.7	4.0	74.7	1.6	$Al(\mathbf{O}H)_3$
Al 2p **Total Al** Na 2s	**Al** $\mathbf{2p_{1/2}}$	75.3	3.8	75.2	2.2	75.3	2.0	75.3	0.8	
			19.5		**19.3**		**24.2**		**28.3**	
		63.1	0.7	63.6	0.8	__	0.0	__	0.0	$\mathbf{Na}_2CO_3$
Na 2s **Total Na**		__	0.0	63.9	5.8	63.7	5.9	63.4	2.6	**Na**OH
Na 2s		64.0	1.2	64.2	1.8	64.3	2.6	64.2	3.5	**Na** (Na-β"-Alumina)
Na 2s **Total Na**			**2.0**		**8.4**		**8.6**		**6.1**	
Total			**100.0**		**100.0**		**100.0**		**100.0**	

The O 1s peak for the non-treated Na-β"-alumina is very broad and cannot be fitted with a single component. The width of this peak reduces significantly with increasing heat treatment temperature accompanied by the formation of a small shoulder on the high binding energy side. Following Zähr *et al.*[69], we choose to take two main components to fit this peak representing oxygen (Al-O, ~530.9 eV, blue color in Figure 3.8) in the crystal structure and hydroxyl (Al-OH, 532.5 eV, orange color in Figure 3.8) groups present at the surface. In addition, oxygen atoms bound to carbon (C-O, O-C=O, Na_2CO_3) are taken into account in the ratio determined from the C 1s peak, corrected for their respective photoelectron cross sections (Table S2) and chemical formula. Interestingly, while the Al-OH component is comparable in area to the Al-O component, it reduces significantly after heat treatment at 900 °C. This is strong evidence that reducing the amount of hydroxyl groups at the interface is key to obtain low ionic interfacial resistance to sodium metal.

For completeness, we also show the Al 2p and Na 2s spectra. Following Zähr *et al.*[69] and Hüfner *et al.*[70], we refrain from deconvoluting the Al 2p doublet ($2p_{3/2}$ and $2p_{1/2}$) into an Al-O and Al-OH component with different binding energies. Instead, both components are constrained to the same binding energy and the peak area ratio between the two components is constrained to the value calculated from the analysis of the O 1s peak. Note that the presence of the Al 2p peak confirms that the surface contamination layer is thinner than the photoelectron inelastic mean free path[70]. From the Na 2s peak, we observe the presence of NaOH, for the heat-treated samples only, which we ascribe to segregated sodium reacting to NaOH at the surface during the short transfer into the XPS chamber. We confirmed experimentally that this short air exposure does not affect the interfacial resistance between sodium metal and Na-β''-alumina. XPS results are summarized in Figure 3.8m showing that the heat treatment results in a significant reduction of hydroxyl groups and carbon contaminations at the Na-β''-alumina surface.

3.2.3.2 Temperature-dependent transport properties

In order to better understand the transport kinetics at the Na/Na-β”-alumina interface, we analyze the different conduction processes as a function of temperature on samples heat treated at 900 °C. Figure 3.9a exemplarily shows Nyquist plots of Na/Na-β”-alumina/Na cells measured from 0 to 60 °C. To avoid hysteresis effects due to thermal cycling, each measurement was taken with a freshly and identically prepared cell. It is clear that the impedance of both the Na-β”-alumina ceramic and the interface decrease as the temperature increases. Extracting both contributions using the equivalent circuit of Figure 3.7a results in the temperature-dependent ion conductivity and interfacial resistance shown in Figure 3.9b. The ionic conductivity of the Na-β”-alumina ceramic at room temperature is 1.6 mS cm^{-1} and follows an Arrhenius behavior with activation energy of 0.41 ± 0.02 eV derived from a linear fit of $\ln(\sigma_{ion}T)$ vs 1000/T. In comparison, the interfacial process follows an Arrhenius behavior with similar activation energy of 0.40 ± 0.03 eV derived from a linear fit of ln(T/Rint) vs 1000/T. An analogous situation was recently also reported for the Li/LLZO interface and points towards an interfacial resistance dominated by current constriction resulting from void formation at the interface upon stripping.[62] As pressure is applied during the measurements, a good contact is expected to be maintained also at low temperatures. Therefore, we attribute the temperature-dependent interfacial resistance to improved kinetics rather than to a change in viscosity of sodium metal with temperature. Additional requirements for solid electrolytes are low electronic conductivity σ_{el} and high ionic transference number t. Figures 3.9c and d show the electronic conductivity and ionic transference number t from 0 to 60 °C, plotted as $1-t$ for better readability. At room temperature, a low electronic conductivity of $7 \cdot 10^{-11}$ S cm^{-1} is measured, which increases only slightly with temperature following an Arrhenius behavior with an activation energy of 0.42 eV. Corresponding transference numbers are close to 1 in this temperature range. Overall, the high ionic conductivity coupled to low electronic conductivity of Na-β”-alumina ceramics and interfacial charge transfer process with low resistivity are key enablers for the development of solid-state Na/Na-β”-alumina batteries.

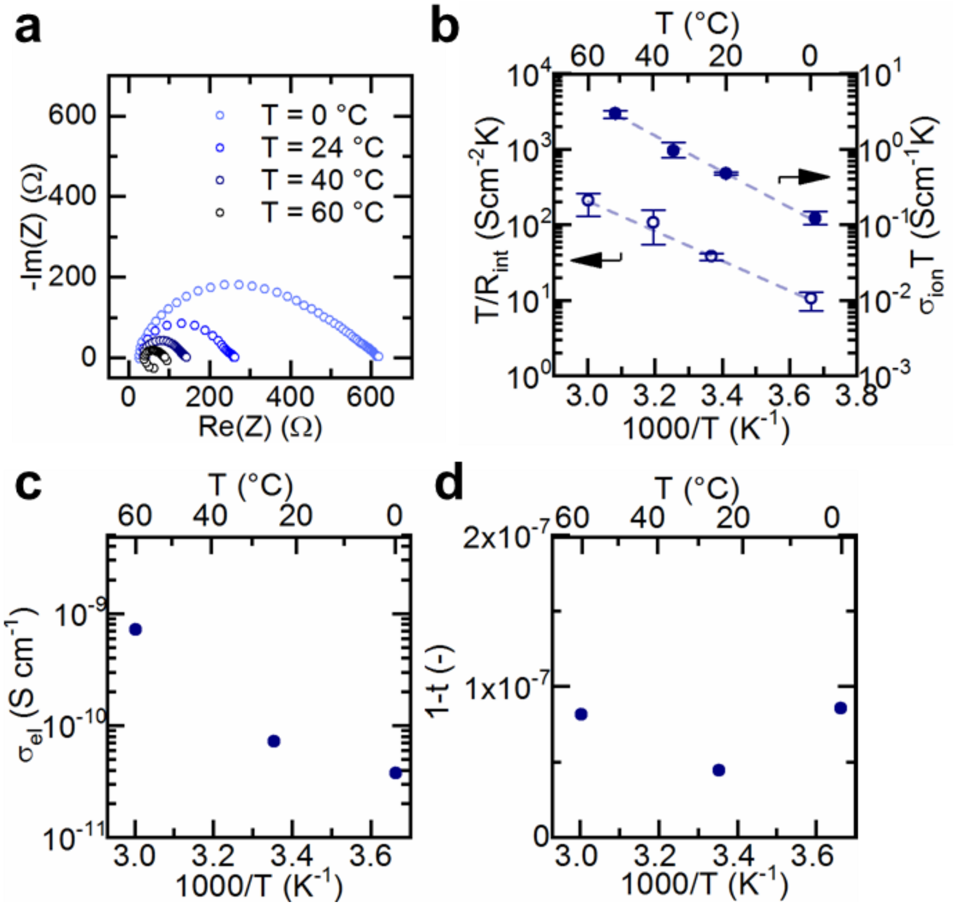

Figure 3.9: (a) Representative Nyquist plots as a function of temperature on samples heat treated at 900 °C. Temperature-dependent (b) interfacial resistance and ionic conductivity, (c) electronic conductivity, and (d) ionic transference number t plotted as 1-t for readability.

3.2.3.3 Critical current densities in Na-β”-alumina ceramics as function of charge and R_{int}

After demonstrating low interfacial resistance and favorable charge transport properties, we now focus on the sodium stripping/plating behavior in symmetric Na/Na-β”-alumina/Na cells. The critical current densities (CCD) at which dendrites propagate through Na-β”-alumina ceramics were determined by galvanostatic measurements. In order to ensure a good contact between sodium metal and Na-β”-alumina ceramics, 10 cycles of 1 h at a current density of 10 μA cm^{-2}

were first applied.[21] CCD measurements were then performed with increasing current density at each cycle, while transferring a constant charge density of 0.25 mAh cm^{-2} to be comparable with recent studies on LLZO. To mitigate too strong contact loss during stripping as recently demonstrated in lithium metal in contact with LLZO,[62,63] the cells were put under pressure at 3.4 MPa. After the measurement, the pressure was recorded to be still about -5 % of the initial value. The potential response during a typical CCD measurement is shown in Figure 3.10a for a sample heat treated at 900 °C. In this example, the CCD was reached at 9 mA cm^{-2} as observed by a sudden drop of the potential to 0 V (see arrow in Figure 3.10e), indicating a short circuit in the cell due to dendrite formation. In some cases, if the dendrites short the cells only locally at point contacts, the potential may partially recover as shown in the example of Figure 3.10e. To confirm the short in the cell, PEIS was performed between each stripping/plating cycle. Figure 3.10b shows typical PEIS spectra before and after the CCD was reached. Below the CCD, the spectra are dominated by the electrolyte contribution (as described by parallel connection of R_{NBA} and CPE_{NBA} in Figure 3.7a). After short-circuiting, the electrolyte contribution is significantly reduced, and the spectra are dominated by a resistive behavior, with some minor capacitance contributions, possibly related to the local point contact of the sodium dendrite. A closer look on the potential response at different stages of the measurement (boxes in Figure 3.10a), are shown in Figure 3.10c-e. At low current densities, the potential response follows an Ohmic behavior, $U = RI$, where U is the potential, R the total cell resistance, and I the current as observed by the stable potential. Due to negligible interfacial resistance, the overpotential at low current density is given by the electrolyte only. As the current density increases, the potential response deviates from Ohmic behavior until CCD is reached. Such an increase of potential was recently ascribed to void formation in lithium metal at the interface to LLZO during stripping,[63] but measurements with a reference electrode would be required to decouple stripping from plating effects.

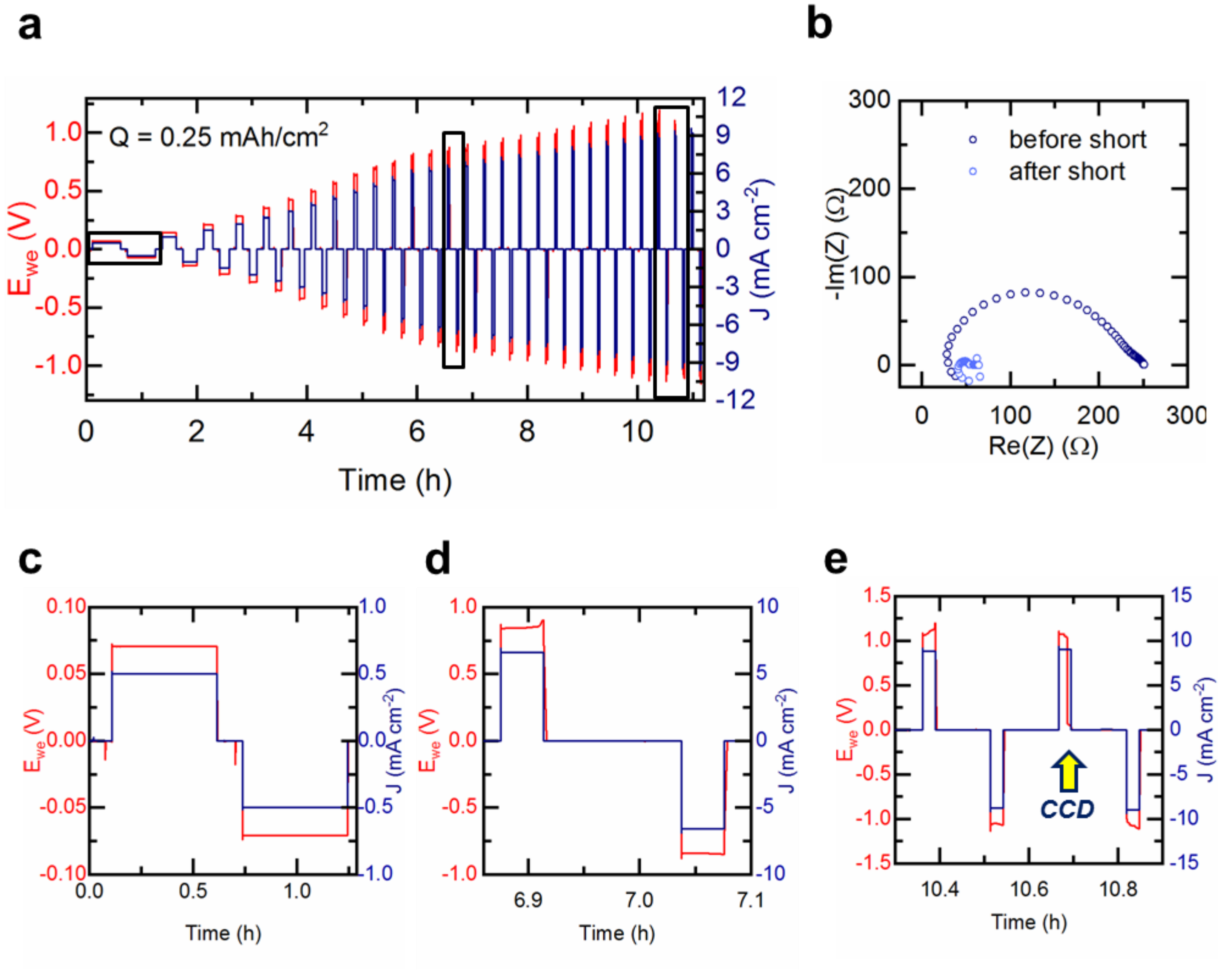

Figure 3.10: (a) Representative potential response of a Na/Na-β”-alumina/Na cell undergoing CCD measurement at room temperature and charge of 0.25 mAh cm^{-2} per half cycle. (b) Nyquist plots before and after short-circuit. Closer view on the potential response during CCD measurement (c) at low current densities (d) at medium current densities, and (e) close to short circuit, showing an increase of the polarization.

We now explore the impact of the charge density and interfacial resistance on CCD. Figure 3.11a and b compares the potential response of cells cycled with charge densities of 0.25 and 3 mAh cm^{-2}, respectively, up to a current density of 6.6 mA cm^{-2} using Na-β”-alumina pellets heat treated at 900 °C. While the cell cycled at a charge density of 0.25 mAh cm^{-2} does not fail up to 6.6 mA cm^{-2}, the cell cycled at a charge of 3 mAh cm^{-2} fails at 5.5 mA cm^{-2} as observed by the sudden drop in potential response to 0 V, indicated by the arrow in Figure 3.11b. Compared to the potential response of the cell cycled at low charge density, the polarization of the cell cycled at high charge density increases continuously with increasing current density until the cut-off voltage of 4.5 V is reached (axis cut at 1 V for better readability). Early cell failure with increased charge supports the void formation hypothesis. When a larger amount of charge is transferred per cycle, void formation in sodium metal near the interface to Na-β"-alumina reduces the contact surface area and thus increases the interfacial resistance and the local current densities at the remaining contact spots. As a result, higher overpotentials are needed to supply a constant current. While void formation can be avoided by increasing the pressure,[62,63] we performed all CCD measurements with a charge density of 0.25 mAh cm^{-2} to enable direct comparison with CCD values on LLZO.[22]

The impact of increasing heat treatment (HT) temperature is shown in Figure 3.10c. The CCD values increase significantly with decreasing interfacial resistance. For the maximum heat treatment temperature applied, an average CCD value over four samples of 12 mA cm^{-2} is obtained. To the best of our knowledge, this is the highest reported CCD value for a solid electrolyte at room temperature (without implementation of a porous electrolyte layer that locally reduces the current density by increasing the surface area as in Chapter 3.1). Increasing CCD values with decreasing interfacial resistance have previously been reported for LLZO,[33] where this effect was attributed to the suppression of localized regions featuring higher current densities, often referred to as “hot spots”. Similar observations were also made for Na-β”-alumina at elevated temperatures using a molten sodium metal anode, where higher charge could be passed in cells featuring lower charge transfer resistances.[71] Note that the maximum heat-treatment temperature in this study was limited by the furnace to 900 °C. While it is possible that higher temperatures may further decrease the interfacial resistance and thus increase the CCD value, void formation at the interface may limit the physical maximum CCD. Nonetheless, this surface treatment gives optimistic results for the implementation of fast-charging all-solid-state batteries.

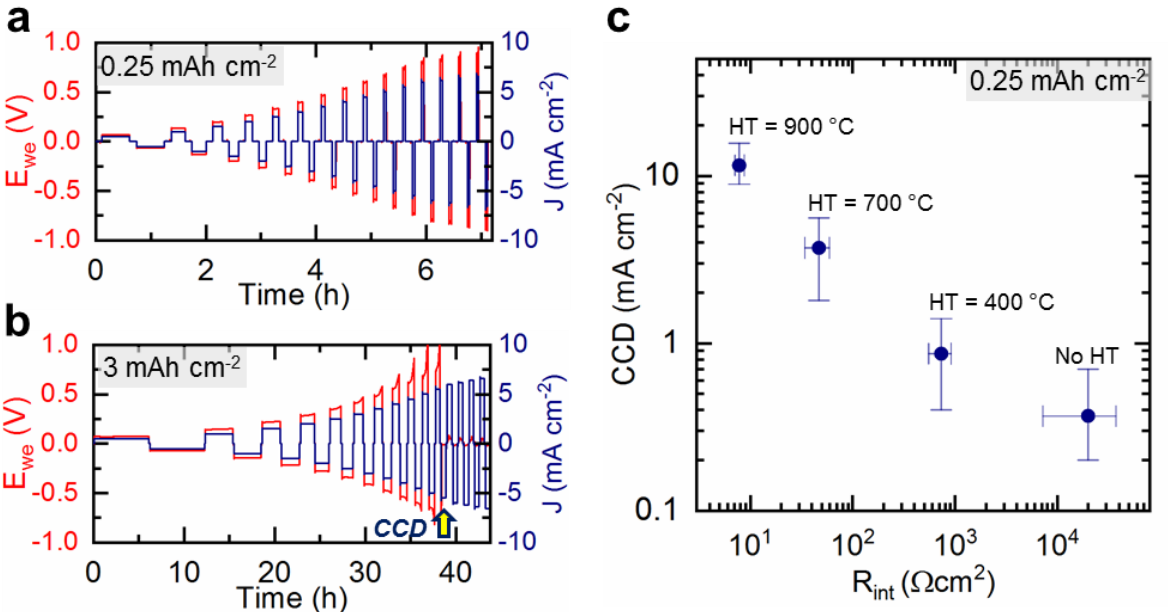

Figure 3.11: Representative potential responses of Na/Na-β”-alumina/Na cells undergoing CCD measurements at total transferred charge Q per half cycle of (a) $Q = 0.25$ mAh cm^{-2} and (b) $Q = 3$ mAh cm^{-2} for Na-β”-alumina samples heat treated at 900 °C (while the potential response of the two last cycles before failure reached a limit of 4.5 V, the maximum value of the y axis scale bar is 1 V for better readability). (c) CCD as a function of interfacial resistance.

3.2.3.4 Temperature-dependent CCD and comparison with literature

The effect of stripping/plating temperature on the CCD was investigated on samples heat treated at 900 °C in a temperature range from 0 to 60 °C. The results are plotted in Figure 3.11a in Arrhenius representation. Similarly to literature,[29,57] we find an exponential relationship between CCD and inverse temperature (taking into account the error bars) with activation energy of 0.27 eV. By increasing the temperature to 60 °C, critical current densities up to 19 mA cm^{-2} can be achieved, which is in agreement with acoustic measurements from the 1980s employing a liquid mercury sodium amalgam.[57] While this temperature behavior is currently not completely understood, Han *et al.* recently proposed that dendrite formation is governed by the electronic conductivity of the electrolyte, governing the rate at which sodium ions are reduced to metallic sodium in the bulk of the solid electrolyte above the plating potential.[72] They concluded that the electronic conductivity should be lower than 10^{-12} S cm^{-1} to enable dendrite-free plating at 10 mA cm^{-2}. Although this criterion corresponds roughly to the measured values at room temperature in this study ($7 \cdot 10^{-11}$ S cm^{-1}, 12 mA cm^{-2}), the electronic conductivity at 60 °C deviates by almost three orders of magnitude ($7 \cdot 10^{-10}$ S cm^{-1}) from this threshold, whereas the critical current densities improves by 30 %. Furthermore, it was also shown that Na-β”-alumina can sustain critical current densities up to 300 mA cm^{-2}[57] at 350 °C at an electronic conductivity of ~10^{-8} S cm^{-1}.[73] It is clear that the ionic conductivity and charge transfer kinetics are also improved at the same time, and therefore a theory only based on the electronic conductivity cannot fully explain the temperature-dependent CCD measurements. Some of us recently hypothesized that the properties of the alkali metal electrode may govern dendrite formation.[29] It was reported that flux imbalances at the interface caused by differences between the metal self-diffusivity in the alkali metal and the ionic diffusivity in the electrolyte may create metal pile-up at the interface, which eventually acts as nucleation site for dendritic growth. To better understand the role of the electrode metal, we compare in Figure 3.12a the results for LLZO obtained in a previous study.[29] Note that identical measurement conditions were applied and similar interfacial resistances were obtained. Over the measured temperature range, the CCD values for Na-β”-alumina are systematically ten times higher than for LLZO. It is interesting to note that the error bars for Na-β”-alumina are also larger. On the one hand, this could be the result of the bimodal grain and pore size distribution of the Na-β”-alumina ceramics as recently described in detail in a previous publication[68]. In particular, pores at the interface may lead to an increase in local current density. On the other hand, this could be the result of an amplification effect of surface inhomogeneities at higher current densities, as also observed to a smaller extent for LLZO for increasing temperature. When comparing the behavior of the two alkali metals, we should also take into account their different melting temperatures (97.79 °C for Na, 180.5 °C for Li) as they differ in viscosity for the same measurement temperature. In Figure 3.12b, we plot the CCD values as a function of the homologous temperature, defined as the (absolute) temperature (*T*) divided by the melting temperature ($T_{melting}$) of the alkali metal. While similar CCD values are obtained for both the Na and the Li system at e.g. at $T/T_{melting}$ of 0.74, those of the Na system feature a much stronger exponential increase above a homologous temperature of 0.8 (corresponding to >24 °C for Na system, >90 °C for Li system). To better understand these results, we compare in Figure 3.13 temperature-dependent diffusivities in both the Li and the Na systems as reported in literature[50,53] and estimated the diffusivities of Li^+ in LLZO and Na^+ in Na-β"-alumina applying Nernst-Einstein equation.[29] In the lithium system, the diffusivities of Li^0 in Li and Li^+ in LLZO differ by a factor ~100 ($5\cdot10^{-11}$ cm^2 s^{-1} vs $2\cdot10^{-9}$ cm^2 s^{-1} at room temperature, respectively). In comparison, the diffusivities of Na^0 in Na and Na^+ in Na-β"-alumina differ by a factor of only ~10 ($5\cdot10^{-9}$ vs $3\cdot10^{-8}$ cm^2 s^{-1} at room temperature, respectively). Furthermore, it is interesting to note that the self-diffusivity of sodium is about hundred times the self-diffusivity of lithium ($5\cdot10^{-9}$ cm^2 s^{-1} vs $5\cdot10^{-11}$ cm^2 s^{-1} at room temperature, respectively). Interestingly, the Li^+ diffusivity in LiPON ($2\cdot10^{-8}$ cm^2 s^{-1}[74] was reported to be on the same order of magnitudes as the Na^+ diffusivity in Na-β"-alumina. In addition, thin-film all-solid-state batteries based on LiPON with areal capacities up to 160 μAh cm^{-2} were cycled up to 10 mA cm^{-2} without dendrite formation.[75] Thus, while diffusivity may play a role in governing flux balance between the alkali metal and solid-state electrolyte, it should be acknowledged that other parameters such as the mechanical properties of the anode can affect interface stability.

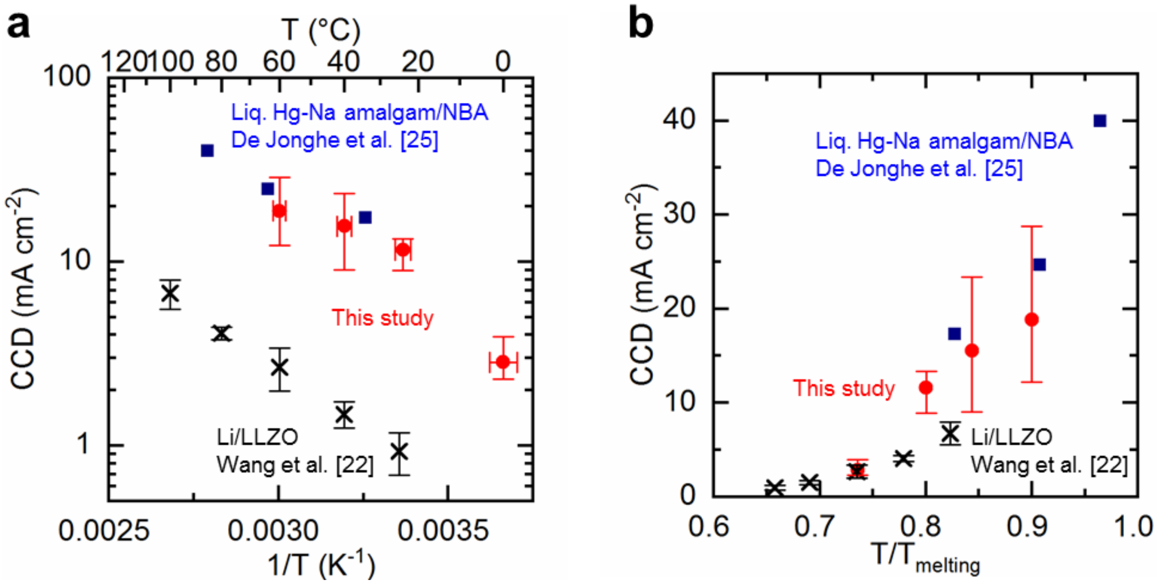

Figure 3.12: Temperature-dependent CCD and comparison with literature (a) in Arrhenius representation (b) as a function of homologous temperature (*$T/T_{melting}$*).

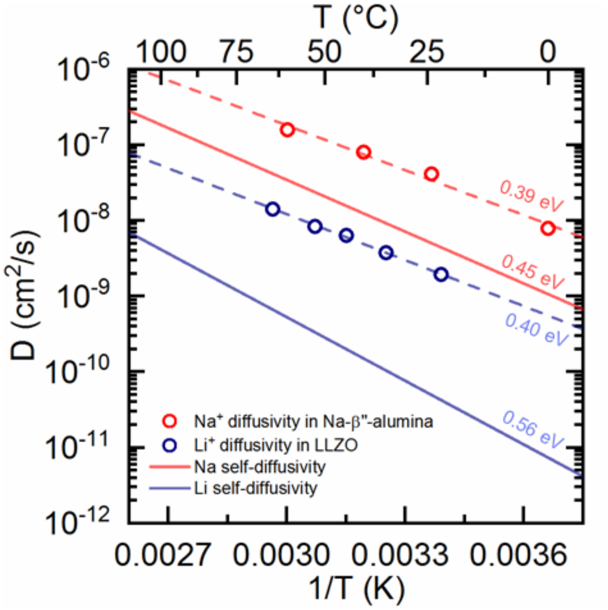

Figure 3.13: Temperature-dependent diffusivity of Na$^+$ in Na-β”-alumina and Na self-diffusivity compared to the diffusivity of Li$^+$ in LLZO and Li self-diffusivity (see manuscript for details).

3.2.4 Conclusion

Applying a heat treatment on finely polished Na-β”-alumina ceramics in argon atmosphere to eliminate surface hydroxyl groups and carbon contaminations, the interfacial resistance of symmetric Na/Na-β”-alumina cells was reduced from 100s of Ωcm^2 to 8 Ωcm^2 at room temperature. This improvement in interfacial resistance drastically increases the critical current density from 0.3 to 12 mA cm^{-2} for a total transferred charge density of 0.25 mAh cm^{-2} per half cycle. Increasing the charge density was demonstrated to increase the cell polarization, presumably due to the formation of voids at the interface between electrolyte and metal anode, highlighting the need of applying stack pressure. Compared to the garnet-type LLZO, the critical current densities obtained for Na-β”-alumina, measured on the same setup under identical measurements conditions,[22] are ten times higher despite similar transference number. While the temperature-dependent critical current density measurements both show an exponential behavior with comparable activation energy, we attribute the tenfold difference in CCD to the diffusive and mechanical properties of the alkali metal and of the solid electrolyte.

Currently the development of all-solid-state batteries based on sodium metal anodes is hindered by the lack of availability of an appropriate sodium cathode material that can compete in performance e.g. with nickel-rich layered oxides employed in lithium-ion batteries (e.g. NMC811). However, our results demonstrate that if such a cathode material becomes available in the near future, an all-solid-state sodium metal battery with fast charging capabilities based on a Na-β”-alumina electrolyte becomes a very promising option for rapid commercialization and market deployment.

3.3 A Comparison of the Mechanics and Electroplating Behavior of Li and Na at the Electrode/Electrolyte Interface

3.3.1 Introduction

Although there have been many studies to attempt to corelate variables with the tendency for electrodeposited alkali metals to grow through a solid-electrolyte, how a soft alkali metal can penetrate through a rigid ceramic is still not well understood. It was proposed by De Jonghe *et al.*[57] for molten Na/S batteries using a Na-β-alumina electrolyte that Na metal penetration was caused by either mechanical pressure build-up within a surface defect (Mode I) and/or by internal recombination events of Na^+ and electrons (Mode II). Since then, similar hypotheses have been proposed for solid Li and Na metal penetration, relating to the mechanical, microstructural, and electronic properties of the solid-electrolyte and electrode/electrolyte interface. A similar Mode I mechanism was proposed for solid Li metal penetration by Porz *et al.*[23] and others[29,37,76,77], which hypothesizes that inadequate flow of Li metal away from the interface during plating can result in local regions of pressure build-up. By assuming the pressure build-up is concentrated in a surface defect, a Griffith fracture mechanics approach can be taken to estimate the current density required to induce electrolyte fracture. However, limited understanding of the mechanical behavior of alkali metals, limited information on surface flaw size and shape distributions, and limited information on the current density distribution at the interface have led to discrepancies between theoretical and experimentally observed values. Alternatively, neutron depth profiling experiments by Han *et al.*[72] have been used to hypothesize that metal filaments originate within the electrolyte bulk from internal recombination events from Li^+ and electrons that are caused by high electronic conductivities. However, these results are seemingly inconsistent with the observed tendency for solid-state cells to cycle at higher current densities at higher temperatures and cannot completely justify the differences between rate capabilities in Li metal systems and Na metal systems with electronically similar electrolytes.

In Chapters 3.1 and 3.2, it was hypothesized that based on the exponential dependence of the critical current density (CCD) on temperature that some transport-limiting phenomenon acts as the governing factor for CCD. Similar to a classic dendrite, it was hypothesized that the transport limitation leads to a physical instability that eventually results in propagation of the metal filament through the solid-electrolyte. In Chapters 3.1 and 3.2, self-diffusivity was used as a defining transport mechanism to compare transport of the electroplated metal within the electrode bulk. However, given the time-scales and mechanical environment at which electroplating is occurring, it is unlikely that self-diffusion is the primary mechanism of transport. While fitting temperature dependent data as in Chapter 3.1 and 3.2 is not trivial and somewhat subjective, the best fit over this temperature range according to a least-squares fit results in an exponential equation, suggesting Arrhenius behavior. Interestingly, by examining the Arrhenius behavior of the CCD of Li/LLZO, it can be seen that the activation energy associated with CCD in the Li/LLZO system is ~0.36 eV. This value seems to closely resemble both the values for Li metal creep[76] (0.38 eV) and bulk LLZO conduction (0.37 eV).

It has been recently demonstrated that under identical cycling conditions, Na metal filaments initiate at significantly higher (~10x) current densities in Na-β”-alumina (NBA) compared to Li metal in the $Li_7La_3Zr_2O_{12}$ (LLZO) garnet and seems to be consistent with other trends observed throughout the literature[29,37]. Given that the mechanical and electronic properties of both oxide electrolytes are relatively similar, it is possible that the tendency to form metal filaments through the electrolyte is correlated to the mechanical properties of the metal anode.

The deformation of both Li and Na metal are known to be highly influenced by viscoplastic creep due to the low melting temperatures of 180°C and 98°C for Li and Na respectively. These melting temperatures correspond to homologous temperatures ($T_H = T/T_M$) of 0.66 and 0.80 at room temperature. Due to its higher homologous temperature at room temperature, Na metal exhibits both lower elastic and plastic properties compared to Li metal. Based on the Mode I hypothesis of metal penetration, the softer metal that can flow out of an existing surface defect more easily would be less likely to fracture the electrolyte and thus exhibit a higher CCD. This is consistent with the differences between the Na/NBA and Li/LLZO systems that has been experimentally observed, supporting the fracture mechanics-based mechanism behind filament initiation.

In this work, the results of a recent analysis modeling the flow of electroplated metal out of a surface defect is modified and used to assess the feasibility of a Mode I fracture mechanism for metal filament initiation in ceramic electrolytes. Combining the results of recent reports on the fracture properties of both LLZO and NBA, a representative critical flaw is used to assess the hydrostatic pressure build-up caused by electrodeposition. Then, the results of recently published models for describing the flow of electroplated metal are modified to incorporate the effects of strain-rate sensitivity of the alkali metal electrodes. From the models, the pressure build-up within a surface defect can be estimated and compared to experimental data and the resulting trends closely resemble the trends found within the experiments. Overall, this work suggests that the Mode I fracture hypothesis which governs CCD may be very plausible, thus providing guidelines on how to improve the rate capabilities of alkali-metal/solid-electrolyte batteries.

3.3.2 Mechanisms of Mode I Fracture

3.3.2.1 Conditions for fracture of the ceramic electrolyte

Based on the work by Armstrong *et al.*[78] for molten Na batteries, and more recent work by Porz *et al.*[23] and Barroso-Luque *et al.*[77], it is assumed that the origin of alkali metal penetration occurs at a pre-existing surface defect, as illustrated in Figure 3.14. Presumably the electroplated metal would fill the surface defect and eventually if the flux of incoming plated metal exceeds the rate at which existing metal can flow out of the defect, then a pressure build-up will occur inside the defect. All of the following analysis assumes that the critical defect has been filled with electroplated metal and thus can begin to build pressure.

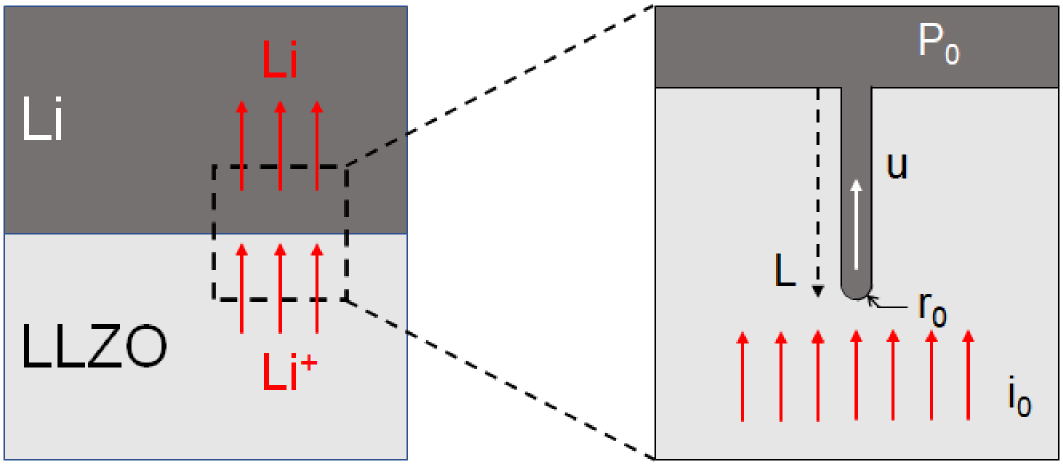

Figure 3.14: Illustration of the electrodeposition of Li at a surface flaw at the Li/LLZO interface under a stack pressure of P_0. It is assumed that the Li^+ are plated at the interface at a current density of i_0 near a surface flaw with length L and radius r_0. In order to accommodate the continued deposition of Li, the existing Li within the flaw must flow into the bulk with a velocity u.

Based on the idealized flaw geometry depicted in Figure 3.14, the criterion for crack propagation (assuming mode I loading under plane strain conditions; not to be confused with the Mode I alkali metal penetration model proposed by De Johnge *et al.*[57]) given by linear elastic fracture mechanics, is given by the equation:

$$\sigma \geq \sqrt{\frac{EG_c}{\pi a}} \tag{3.4}$$

where σ is the average stress within the flaw, E is the elastic modulus of the electrolyte, G_c is the critical strain-energy release rate of the electrolyte, and a is the flaw length. The product of the elastic modulus and the strain-energy release rate can also be expressed as the fracture toughness by the following expression:

$$K_{IC} = \sqrt{EG_c} \tag{3.5}$$

where K_{IC} is the mode I fracture toughness. Thus, if the plating current into the defect is sufficiently high to induce a stress that satisfies this criterion, the crack would propagate and thus initiate a metal filament. The current density at which the criterion is met would be considered the Mode I theoretical CCD.

Recent works by Han *et al.*[79] and Bay *et al.*[80] reported on the fracture properties of both LLZO and NBA electrolytes, using identical synthesis and processing methods used in Chapters 3.1 and 3.2. The mechanical properties of both LLZO and NBA obtained using flexural, ball-on-ring, and ring-on-ring methods are listed in Table 3.3. Based on the reported values for the fracture stresses and fracture toughnesses, an average size for the critical flaw length could be obtained. Furthermore, since the critical flaws are assumed to be area distributed surface flaws, the differences in sample size between the electrochemically tested ceramics and the mechanically tested ceramics could be accounted for according to the Weibull weakest-link model as follows:

$$\frac{\sigma_{f1}}{\sigma_{f2}} = \left(\frac{A_1}{A_2}\right)^{\frac{1}{M}} \tag{3.6}$$

where σ_f is the mean fracture stress, A is the effective area, and M is the Weibull modulus. Based on Equation 3.4 and 3.5, the average critical flaw lengths were determined to be ~15 µm and ~70 µm for LLZO and NBA respectively.

Table 3.3: List of electrolyte fracture properties for LLZO (as reported by Han *et al.*[79]) and for NBA (as reported by Bay *et al.*[80])

	LLZO	NBA
Mode I Fracture Toughness K_{1C}	1 MPa $m^{1/2}$	3 MPa $m^{1/2}$
Mean Fracture Strength σ_f	100 MPa	158 MPa
Weibull Modulus M	3.39	13.47
Mean Fracture Strength (Weibull) σ_f	158 MPa	197 MPa

However, as mentioned by Barroso-Luque *et al.*[77], the fracture toughness values measured using *ex situ* or more traditional experiments may not accurately reflect the fracture criterion necessary for internally imposed stresses caused by electrodeposition. In these *ex situ* experiments, the energy released when opening the crack is related to the surface energy of the newly exposed surface area to the surrounding environment. However, when propagating the metal filament, the newly exposed surface is instead exposed to the surface of the electroplated metal. Therefore, while the critical defect may remain the same, the "effective" fracture toughness may be different. The differences in surface energy in the *ex situ* and *in situ* cases can be estimated by the ratio of the surface energies as follows:

$$\frac{G_{es}}{G_{is}} = \frac{\frac{\gamma_{\frac{env}{SE}}}{\Delta A_c}}{\frac{\gamma_{\frac{AM}{SE}}}{\Delta A_c}} = \frac{\gamma_{\frac{env}{SE}}}{\gamma_{\frac{AM}{SE}}} \tag{3.7}$$

where G_{es} is the strain-energy release rate under *ex situ* measurements, G_{is} is the strain-energy release rate under *in situ* measurements, ΔA_c is the change in surface area associated with opening of the crack, $\gamma_{env/SE}$ is the surface energy between the solid-electrolyte and the *ex situ* testing environment, and $\gamma_{AM/SE}$ is the surface energy between the alkali metal and solid-electrolyte. Using the surface energy between Li/LLZO calculated by density functional theory[33], the effective fracture toughness of LLZO can be estimated to be ~0.12 MPa $m^{1/2}$. While the Na/NBA surface energy is unknown, it is assumed that the ratio is similar to that of Li/LLZO, which would result in an effective fracture toughness of ~0.38 MPa $m^{1/2}$.

3.3.2.2 Stress distribution within the surface defect

Based on the Mode I failure mechanism proposed by De Johnge *et al.*[57], the fracture of the ceramic electrolyte is caused by a pressure build-up within the surface defect due to the inability of the pre-existing metal to deform quickly enough to accommodate the continued deposition of additional metal. It has been demonstrated in recent works[52,76,81–83], due to the low melting temperatures of both Li and Na metal, that deformation of both metals at room temperature and above is highly influenced by dislocation climb-controlled creep. Because of the prominence of creep at room temperature and above, work-hardening in both metals is balanced by recovery, which allows both metals to flow at a steady-state stress under a constant strain-rate[52,76,83]. Furthermore, for both Li and Na metal which have high homologous temperatures at room temperature, the flow stress is highly dependent on the applied strain-rate. The dependence on temperature and strain-rate are highlighted in the generalized creep equation as follows:

$$\sigma_{creep} = A\dot{\varepsilon}^{\mathrm{m}} \exp\left(\frac{Q}{nRT}\right) = \tilde{A}(T)\, \dot{\varepsilon}^{\mathrm{m}} \tag{3.8}$$

where σ_{creep} is the creep stress, $\dot{\varepsilon}$ is the strain rate, m is the strain-rate sensitivity exponent, n is the stress exponent, Q is the activation energy for dislocation climb (in the case of Li and Na), R is the molar gas constant, T is the temperature, and A is a constant. Given that deformation of both alkali metals is observed to be dominated by creep within these pressure and temperature regimes, it is assumed that the deformation of both alkali metals is governed by this relationship. Therefore, as incoming metal is electrodeposited at the electrode/electrolyte interface, the pre-existing metal is put under a compressive stress due to the volume expansion associated with the reduction of the cation. The resulting stress thus induces a creep-dominated plastic flow of the metal away from the interface. This process is illustrated in Figure 3.15a. Given that strain is only caused by deviatoric stresses, the hydrostatic stresses primarily exert pressure on the surrounding electrolyte. Therefore, if the magnitude of the hydrostatic pressures of the confined metal generate sufficient pressure such that the stress intensity factor at the crack tip exceeds the fracture toughness, then the crack will propagate.

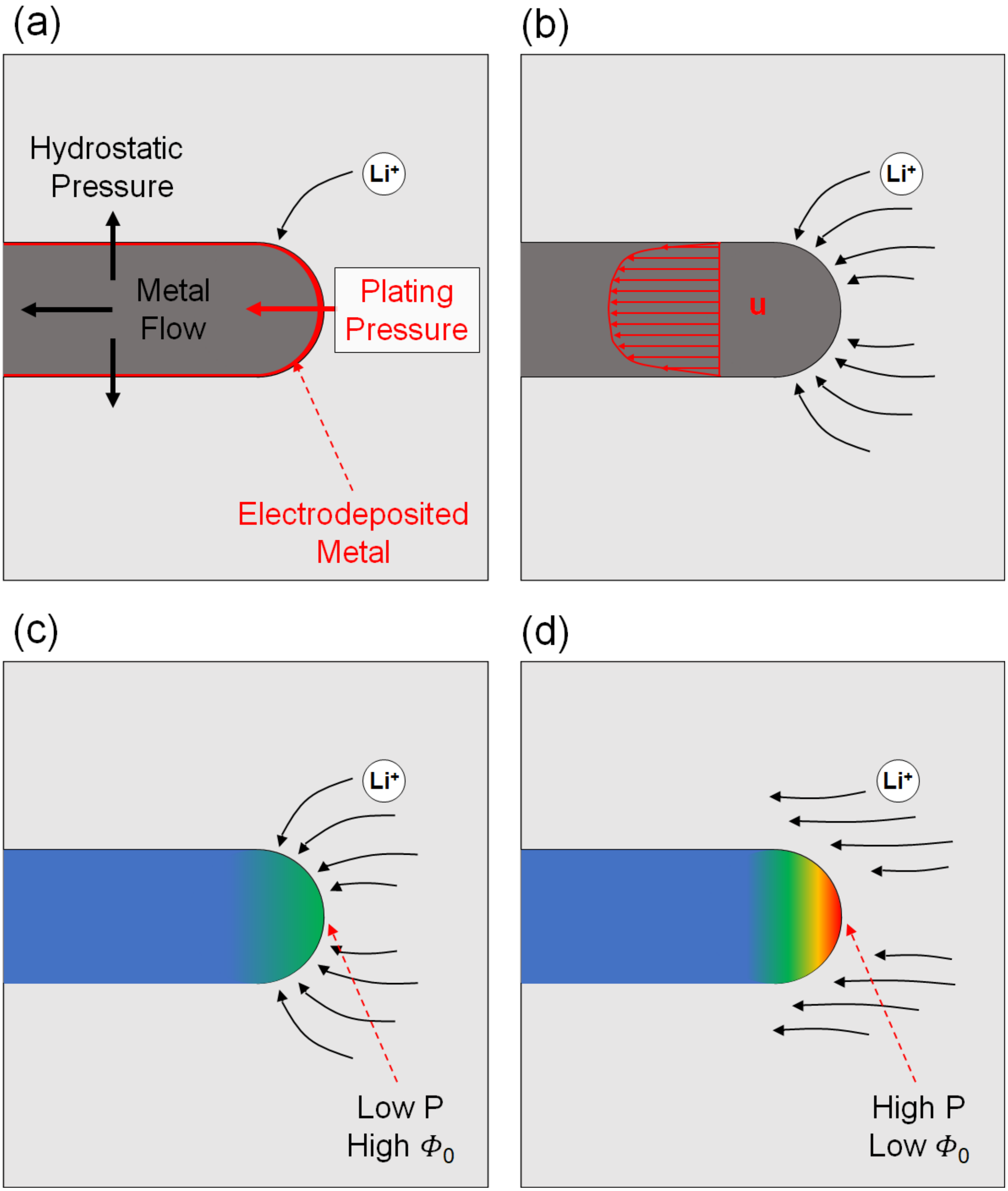

Figure 3.15: Illustration of the physical processes that occur during Li electrodeposition within the surface flaw. a) Li is electrodeposited at the Li/LLZO boundary (illustrated in red), exerting a pressure on the pre-existing Li within the flaw. The pressure induces flow of the Li out of the flaw and exerts a hydrostatic pressure on the walls of the flaw. b) Modeling the deformation of Li as creeping flow as suggested by LePage *et al.*[76], the velocity profile of Li within the flaw can be determined from the Li^+ flux in the electrolyte. As proposed by Barroso-Luque *et al.*[77], the flux of Li^+ in the electrolyte is affected

by electro-plastic effects. Based on this hypothesis, at regions of low pressures c) electrodeposition is dominated by electrostatic gradients. At regions of high pressure d) the electrochemical potential is reduced which redirects ion flux toward areas of lower pressure.

3.3.2.3 Model and assumptions

Analytical modeling of the Mode I fracture of solid electrolytes was first attempted by Armstrong *et al.*[78] for the case of NBA fracture by the electrodeposition of Na^+ onto a molten Na anode. In this case, the pressure build-up within the flaw was modeled by the well-known Poiseuille law for low Reynold's number flow. With the revived interest of alkali metal electrodes in the solid state, analogous models for solid metal deformation are necessary. However, given the highly plastic deformation of both Li and Na metals at relevant operating temperatures, it has since been hypothesized, and recently justified by Barroso-Luque *et al.*[77], that the deformation of these metals in the solid state can also effectively be described by low Reynold's number fluid flow. Because the deformation is dominated by diffusive processes (creep), the governing equations for metal deformation can be similarly described by diffusive (creeping) fluid flow (Figure 3.15b). Under the assumption that the deformation of the solid metal is analogous to the aptly named creeping flow (Stokes flow), the Navier-Stokes equation reduces to the form:

$$\nabla P = \eta \nabla^2 \boldsymbol{u} = \eta \nabla \dot{\boldsymbol{\gamma}} \tag{3.9}$$

where P is the pressure, η is the viscosity, u is the flow velocity, and $\dot{\gamma}$ is the shear strain rate. This representation of the Navier-Stokes equation strongly resembles the generalized stress-strain relation of a viscoplastic solid:

$$\sigma_{creep} = \eta \dot{\varepsilon} \tag{3.10}$$

Barroso-Luque *et al.*[77] recently developed a model for coupling the relation shown in Equation 3.9 with the electrochemical potential gradients in the electrolyte that govern the metal deposition rates. In their analysis, the diffusion potential in the solid electrolyte around the flaw is modeled, which provides a description of ion flux around the flaw tip. Assuming that the majority of the ion flux is concentrated around the flaw tip, the description of the flux therefore provides the initial flow velocity potentials into the flaw. Subsequently, the pressure distribution in the solid metal along the length of the flaw can be described by Stokes flow and compared to the fracture toughness. One of the main novelties of Barroso-Luque *et al.*'s work is that by coupling the electrochemical potential with the stress distribution at the electrode/electrolyte interface, they are able to define a length scale named the electro-plastic (EP) screening length. They demonstrate that based on the generalized diffusion potential at the electrode/electrolyte interface given by:

$$\mathbf{\Phi} = \mu + zF\boldsymbol{\phi} - \Omega_V \boldsymbol{\sigma_e} \tag{3.11}$$

where Φ is the electrochemical potential, μ is the ion chemical potential, z is the valence, F is Faraday's constant, ϕ is the electric potential, Ω_V is the ion volume, and σ_e is the applied stress, the pressure exerted by the metal anode on the electrolyte reduces the electrochemical potential and thus reduces the ion flux. Therefore, regions of high pressure along the interface will locally reduce the electrochemical potential gradient, thus redirecting the flux of electrodepositing ions (Figure 3.15c-d). This implies that it becomes thermodynamically unfavorable to plate metal at a region of high stress. Without this consideration, the classical Poiseuille pressure is related to the flaw-tip radius (r) given by:

$$P \sim \frac{1}{r^2} \tag{3.12}$$

Meanwhile, accounting for the electroplastic effects as shown by Barroso-Luque *et al.*[77], the pressure build-up is instead related by:

$$P \sim \frac{1}{r^2 + \xi^2} \tag{3.13}$$

where ξ is the EP length, a length scale that is a material constant dependent on the conductivity of the electrolyte and viscosity of the metal. The classical solution suggests that the pressure diverges as the radius approaches zero, which is unphysical. The introduction of the EP length therefore bounds the pressure such that the upper bound of the pressure is related to material properties. Thus, for flaws with radii sufficiently lower than the EP length, the effects of electroplasticity dominate such that electrodeposition is directed away from the high pressure at the flaw tip, "screening" out inhomogeneities in the deposition flux. The major implication of this is that for sufficiently small flaw tip radii, the deposition flux at the electrode/electrolyte interface is completely homogeneous with negligible plastic flow and therefore the pressure within the flaw becomes completely hydrostatic. Under the absence of flow, the magnitude of the hydrostatic stress becomes independent of the metal viscosity, and reduces to the form:

$$\Delta P \approx \frac{\alpha z F L}{\sigma_+ V_m} i_0 \tag{3.14}$$

where α is a constant on the order of unity, z is the valence, F is Faraday's constant, L is the flaw length, σ_+ is the ionic conductivity in the electrolyte, V_m is the metal molar volume, and i_0 is the applied current density. The result here demonstrates that the pressure build-up within the flaw is dependent only on the ionic conductivity of the solid electrolyte and the flaw geometry.

While the models of Barroso-Luque *et al.*[77] are extremely powerful for demonstrating the effects of electroplasticity, it is known that the viscosities of both Li and Na metal in the solid-state are dependent on the strain-rate[77], thus exhibiting behavior similar to a non-Newtonian fluid. Therefore, while, the models of Barroso-Luque *et al.*[77] assume that the viscosity is constant, this will likely lead to significant error in the magnitude of the pressure build-up within the flaw.- As demonstrated in Figure 3.16, the magnitude of the viscosity along the width of the flaw will deviate almost three orders of magnitude. Therefore, the viscosity also becomes a function of the applied current density and thus must be considered to more accurately determine the pressure build-up within the surface flaws.

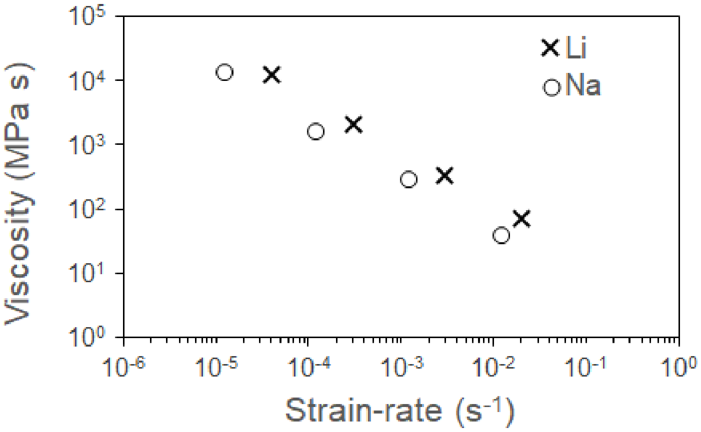

Figure 3.16: The dependence of the viscosity on the strain-rate for Li and Na metal at room temperature. The viscosities are calculated from Equation 3.17, using stress and strain-rate data taken from LePage *et al.*[76] and Wang *et al.*[83].

Using the electrochemical potential and boundary traction equations derived by Barroso-Luque *et al.*[77] as a starting point, the stream function for the flow of metal in the flaw in cylindrical coordinates is given by:

$$\Psi(r,\theta) = \frac{V_m i_0}{zF}\gamma_J\left(\frac{r\left(3r_0^2 + 4\gamma_J\xi^2\right) - r^3}{r_0^2 + 4\gamma_J\xi^2}\right)\cos(\theta) \tag{3.15}$$

The velocity field is then given by the partial derivatives of the stream function:

$$\boldsymbol{u}(r,\theta) = \begin{cases} \dfrac{1}{r}\dfrac{d\Psi}{\theta} \\ -\dfrac{d\Psi}{r} \end{cases} \tag{3.16}$$

Solving the Stokes equation in Equation 3.9, the hydrostatic pressure increase along the length of the flaw can be obtained. For a perfectly plastic solid, the viscosity can be estimated by the generalized relation:

$$\eta = \frac{\sigma_Y}{\sqrt{3}\dot{\varepsilon}} \tag{3.17}$$

where σ_Y is the yield strength and $\dot{\varepsilon}$ is the uniaxial strain rate. However, as demonstrated in Equation 3.8, due to the prominence of creep at relevant temperatures of these metals, the observed yield stresses are dependent on the applied strain-rate. Using the data provided by LePage *et al.*[76] and Wang *et al.*[83] for the dependence of yield stress on the strain rate, the effective viscosities of solid Li and Na are plotted in Figure 3.16. Due to the prominence of dislocation climb within these regimes, the viscosities exhibit a power-law relation given by:

$$\eta = \eta_0 \dot{\varepsilon}^m \tag{3.18}$$

where the quantity m+1 is known as the fluid behavior index and η_0 is a coefficient. For the data plotted in Figure 3.16, the values for m and η_0 respectively for Li are -0.83 and 2.7 MPa s^{m+1} and -0.84 and 0.98 MPa s^{m+1} for Na. By substituting the relation in Equation 3.18 into the Stokes equation, the strain rate dependence of the viscosity can be accounted for when solving for the hydrostatic pressure within the flaw:

$$\nabla P = \eta(\boldsymbol{u})\nabla^2 \boldsymbol{u} \tag{3.19}$$

Assuming the flaw is of a high aspect ratio ($r_0 \ll L$), the solution for the hydrostatic pressure increase along the length of the flaw takes the form:

$$\Delta P = \frac{\eta_0}{m+1}\left(\frac{\alpha V_m \gamma_J i_0 L}{zFr_0^2 + 4zF\gamma_J \xi^2}\right)^{m+1} \tag{3.20}$$

The resulting solution for the pressure is near-identical to the solution for constant viscosity as derived by Barroso-Luque *et al.*[77] with the exception of the power-law behavior. However, it can be seen that for the Newtonian case (m = 0, η = constant), the equation becomes identical to that of Barroso-Luque *et al.*[77]. This would presumably be the case for molten Li and molten Na, although due to the differences in surface energies between molten Li and Na compared to solid Li and Na, the effective fracture toughnesses of the electrolyte may vary.

However, not only does the pressure change non-linearly as a function of current density, but because of the coupling between current density and viscosity, the EP length also changes along with the current density. Because of this, the EP length must also be modified to account for variable viscosity at the interface boundary. By redefining the EP length as follows:

$$\xi^2 = \frac{V_m \, \sigma^{\frac{1}{1+m}} \, L}{F} \left(\frac{(m+1) F \, i_0^{-m} L}{V_m \, \eta_0} \right)^{\frac{-1}{1+m}} \tag{3.21}$$

the effects of strain-rate dependence of the viscosity can be accounted for. For the Newtonian case (m = 0), the EP length simplifies to its original form defined by Barroso-Luque *et al.*[77]. Similarly, it can be seen that as the flaw tip radius approaches 0, instead of diverging, the pressure approaches a value that is solely dependent on flaw geometry and electrolyte conductivity, given by Equation 3.14.

The values for key parameters are listed in Table 3.3. It should be noted that the activation energy for Na metal creep has not yet been reported and therefore, a value similar to that of Li is assumed. Furthermore, values for the bulk conductivity of NBA are known to be difficult to accurately assess due to the difficulty of quantifying Na content within the β”-alumina structure and the need for extremely high frequency measurements. Therefore, the bulk conductivity is estimated based on ranges found in the literature.

Table 3.4: List of mechanical and electrochemical properties and their values for the Li/LLZO and Na/NBA system (*indicates value calculated from reference data).

Alkali Metal Properties		
	Li	Na
Viscosity Coefficient η_0	2.7 MPa s^{m+1} [76]	0.98 MPa s^{m+1}
Fluid Behavior Index m+1	0.17 [76]	0.20[83]
Molar Volume V_m	12.9 cm^3 mol^{-1}	23.8 cm^3 mol^{-1}
Activation Energy for Creep	37 kJ mol^{-1} [76]	44 kJ mol^{-1} [83]
Solid-Electrolyte Properties		
	Li	Na
Bulk Ionic Conductivity σ_+	0.5 mS cm^{-1}	10 mS cm^{-1}
Activation Energy for Bulk Conduction	0.37 eV[29]	0.20 eV[84]

3.3.3 Results & Discussion

3.3.3.1 Comparison between the theoretical and experimental CCDs

Figure 3.17 shows the resulting stress intensity factor given by the previously described equations, as a function of the flaw tip radius for Li metal plating inside of a 15 µm long flaw in LLZO under a current density of 5 mA cm^{-2}. Three different situations corresponding to the purely electrostatic solution (disregarding electroplasticity), the electroplastic solution, and the upper bound governed by electrolyte conductivity are plotted. As previously described by Barroso-Luque *et al.*[77], at large flaw tip radii, the electrostatic and electroplastic solutions converge, while at low radii, the electrostatic solution diverges and the electroplastic solution approaches the upper bound. However, accounting for the strain rate dependence of the viscosity results in a more gradual increase in the pressure as the radius decreases compared to the constant viscosity case. Using the curves in Figure 3.17a, a condition for fracture can be defined as illustrated in Figure 3.17b. If the stress intensity factor is larger than the fracture toughness of the electrolyte, then flaws of those dimensions would become critical under the applied current density.

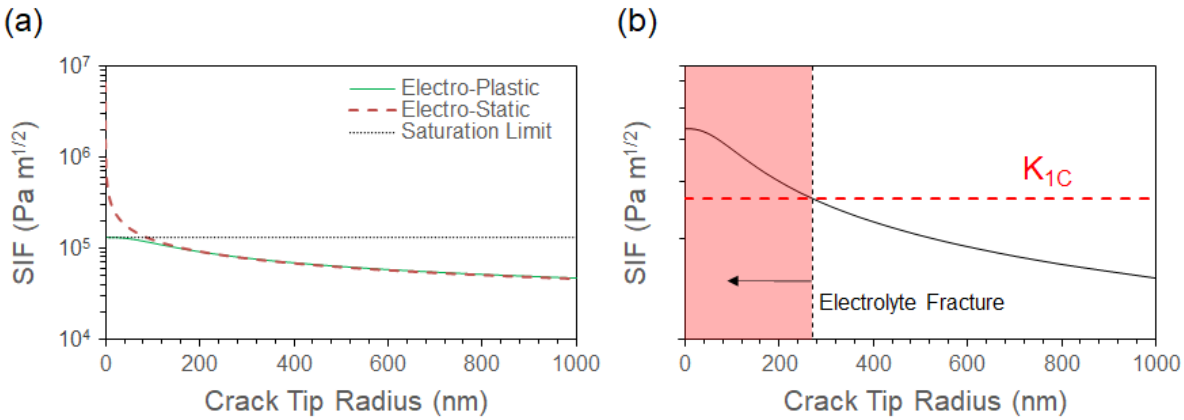

Figure 3.17: The resulting stress intensity factor (SIF) as a function of crack tip radius. a) The stress intensity factor resulting from both the electrostatic and the electroplastic equations, while plating Li into a 15µm crack in LLZO at 1 mA cm^{-2}. b) A comparison of an example SIF curve against the Mode I

fracture toughness (K_{1c}). If the crack tip radius is sufficiently small, the generated SIF exceeds K_{1c} and thus that flaw becomes critical. These critical flaws thus act as initiation sites for alkali metal filaments.

Using this criterion for fracture and the fracture toughnesses for LLZO and NBA as discussed in Chapter 3.1 and 3.2, the theoretical CCDs can be calculated as a function of flaw tip radius. Furthermore, using the activation energies for both metal viscosity and electrolyte conductivity, the CCDs can also be calculated as a function of temperature. The resulting relationships between flaw tip radius and temperature are shown in Figure 3.18.

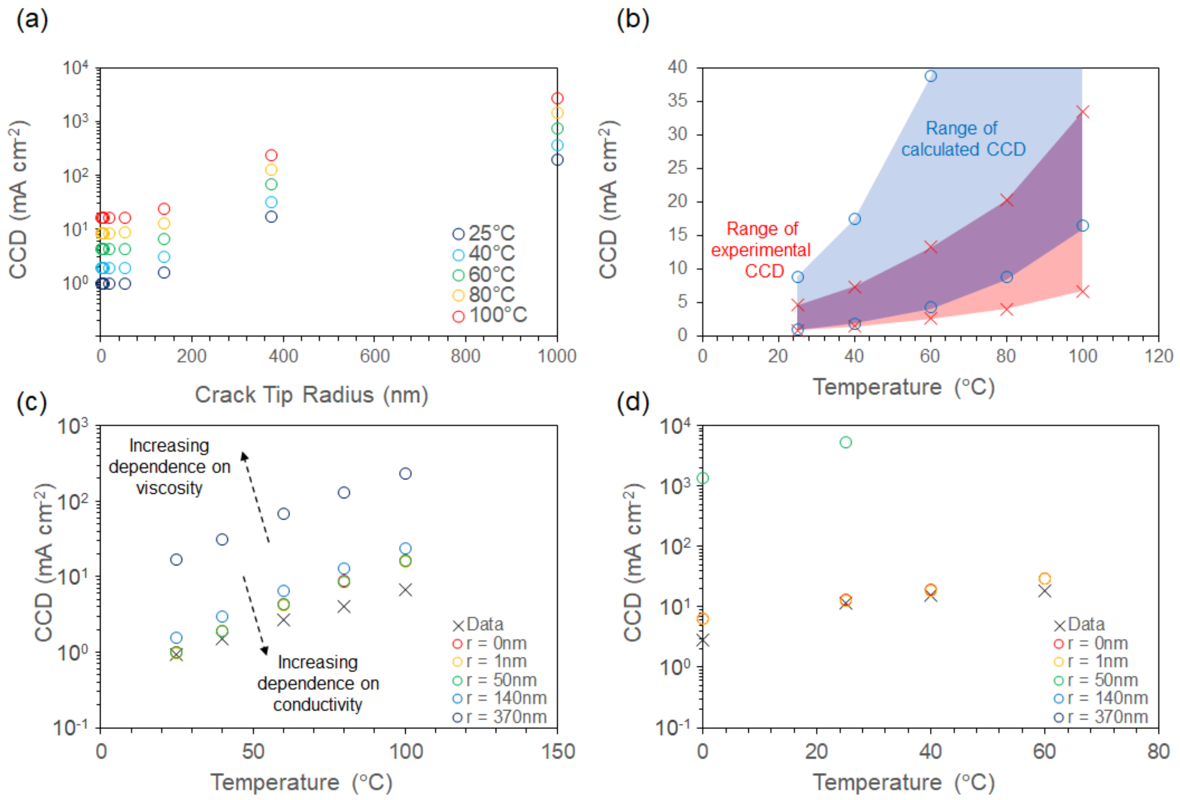

Figure 3.18: Calculated CCDs based on the fracture criterion illustrated in Figure 3.17b. a) The calculated CCD for LLZO as a function of crack tip radius. b) The range of calculated CCDs for LLZO accounting for variations in local current densities and accounting for differences in the effective fracture toughness. c) A comparison of the calculated CCDs for LLZO as a function of temperature with the data from Chapter 3.1. d) A comparison of the calculated CCDs for NBA as a function of temperature with the data from Chapter 3.2.

It can be seen in Figure 3.18a that because the fracture conditions are limited by the completely hydrostatic case at low flaw tip radii, the CCDs also converge at a minimum for sharp flaws. The CCDs in Figure 3.18a are calculated using a fracture toughness given by the ratio of surface energies previously described. However, given the uncertainty in the true fracture toughness under these conditions, the theoretical CCDs more likely fall within a range between the estimated values and the fracture toughness values measured via *ex situ* measurements. Similarly, it was shown by Choudhury *et al.*[85], that unavoidable effects of electrode edges will lead to current focusing effects and that the local current densities at the point of filament initiation can be up to 5x that of the nominal current densities. Therefore, the ranges of theoretical CCDs accounting for uncertainty in the fracture toughness and the ranges of experimentally measured CCDs accounting for macroscopic current focusing effects are plotted in Figure 3.18b. However, extensive future work would be necessary to better quantify the true fracture toughness *in situ* and the true local current densities. Assuming the minimum fracture toughness, the CCDs as a function of temperature and flaw tip radius for Li/LLZO and Na/NBA are plotted in Figure 3.18c and 3.18d respectively, in comparison to the data measured and presented in Chapters 3.1 and 3.2. It can be seen in both cases, that the experimental data closely matches the theoretical CCD values. Accounting for variation in the experimental current densities and calculated current densities, the similarities between the data sets demonstrate that the hypothesized Mode I fracture mechanism may be a very plausible explanation of how metal filaments initiate. Furthermore, it can be seen that in the case of sharp flaws, the temperature dependence of the CCD is completely dependent on the activation energy for bulk ion conduction, as can be seen in Equation 3.14. In both cases, the temperature dependence for both systems closely match this. At larger flaw tip radii, the pressure build-up is dominated by the plastic flow behavior within the flaw and therefore the CCDs in these regimes are instead dominated by the activation energy for metal creep. However, because the activation energies for Li creep and Li^+ conduction in LLZO are so similar, it is difficult to clearly observe this in Figure 3.18c. Given that sharp flaws are extremely difficult to avoid when dealing with bulk processed ceramics, for the data presented in Figure 3.18, the CCDs are likely limited by electrolyte conductivity as opposed to viscosity, which is more consistent with the magnitude of the experimental and theoretical CCDs. Therefore, it can be concluded that the observed differences in CCDs between the Li/LLZO and Na/NBA systems for the data presented here can be explained by the differences in bulk conductivity (LLZO: ~0.1-1 mS cm^{-1}, NBA: ~1-10 mS cm^{-1}) and the fracture toughnesses (LLZO: 1 MPa $m^{1/2}$, NBA: 3 MPa $m^{1/2}$).

3.3.3.2 Implications for solid-state battery design

It was previously hypothesized that the differences in measured CCDs between the Li/LLZO and Na/NBA systems was primarily the cause of the differences in mechanical properties between Li and Na metal. However, it has been demonstrated here that while pressure build-up caused by a lack of plastic flow of metal out of a surface defect in specific cases can certainly generate sufficient stresses to cause fracture within a ceramic solid-electrolyte, the ionic conductivity of the solid-electrolyte also plays a very significant role due to electroplastic phenomena. In the case where electrodeposition is homogeneous, the stress within a surface defect is dominated by the hydrostatic compression of the metal by the overpotential near the interface. Therefore, if the surface defects are all of large flaw tip radii, then the CCD becomes limited by the viscosity of the metal electrode, while for sharp flaws the CCD becomes limited by the bulk ionic conductivity of the electrolyte. In both cases, the fracture toughness of the solid-electrolyte also greatly impacts the CCD. Given that sharp flaws are unavoidable in any bulk processed ceramic material, the CCDs of both bulk LLZO and NBA will thus be primarily controlled by their ionic conductivity and fracture toughnesses. Additionally, the results also suggest that a metal filament can initiate at a variety of different flaw geometries. While it is widely believed that grain boundaries are a major limitation of oxide electrolytes, the mechanism presented demonstrates that grain boundary triple points at the electrode/electrolyte interface are not necessarily the critical defect. While, it is certainly possible for a filament to initiate at a grain boundary triple point, filaments can also initiate within a single grain, which has been observed by Porz *et al.*[23].

Until now, the CCD has been seen as a defining limitation of alkali-metal/solid-electrolyte systems that must be increased in order to improve the charging rates for these batteries. Although it was previously believed that the primary limitation of the system was the mechanical properties of the alkali metal electrode, the proposed model suggests that bulk ionic conductivity is equally important. Therefore, in order to improve the rate capabilities of solid-state systems, future efforts should look toward improving the bulk conductivity and fracture toughness of the solid-electrolyte and/or controlling the size distribution of processing-related flaws.

3.3.4 Conclusions

The origins behind alkali metal filament initiation in rigid ceramic solid electrolyte has been a major question surrounding solid-state batteries. From a practical perspective, the initiation of metal filaments above the CCD severely limits the rate capabilities and lifetime of the battery, while from a mechanistic perspective, the mechanism behind electrodeposition within a solid electrolyte is extremely unintuitive. This work re-evaluates the Mode I fracture hypothesis that suggests that a build-up of pressure within a surface defect can exceed the fracture criterion of the ceramic and propagate a crack across the electrolyte. By utilizing a recent model for describing plastic flow of the metal out of a surface flaw, incorporating the effects of strain rate sensitivity, and combining the model with data on the fracture properties of the electrolytes, a method of estimating the theoretical CCD was developed. By comparing the results of the theoretical CCDs with published experimental data, it was demonstrated that the models for determining the CCD align well with experimental results. Based on the resulting trends, it was shown that while the viscosity of the alkali metal is the dominating factor for flow-driven pressure build-up at large flaw tip radii, bulk ionic conductivity of the electrolyte plays a larger role for sharper flaws and more closely aligns with the experimental data. The results here not only affirm the Mode I mechanism for alkali metal filament initiation and propagation through a solid electrolyte, but also provide concrete strategies for designing solid electrolytes materials in order to achieve solid state batteries with fast rate capabilities.

Chapter 4 Effects of External Pressure on Alkali Metal Stripping

Chapter 3 discusses the phenomena of morphological instabilities upon electroplating on the Li or Na anode, which limits the maximum rates that solid-state batteries can charge at. Since electrodeposition is only occurring on the charge cycle, formation of internal short-circuits should not be problematic upon battery discharge. However, as will be discussed in this chapter, the discharge of the solid-state battery is also limited by a similar phenomenon at the anode/electrolyte interface. It is argued in Chapter 3 that the origin of this instability is essentially a flux imbalance between incoming Li or Na toward the interface provided by the charging current and an outgoing flux away from the interface via diffusion and/or mechanical deformation. However, based on this argument, a similar type of instability should therefore occur upon discharging if there is an imbalance between the outgoing flux of Li or Na dissolving into the electrolyte and the incoming flux that is being supplied by diffusion and/or by mechanical pressure. In this case, rather than a build-up of Li or Na, there will be a build-up of Li or Na vacancies, resulting in a depleted layer near the interface, which may have detrimental effects on the cell resistance.

This chapter investigates this particular phenomenon of Li and Na stripping while discharging of the battery, presenting some of the first work[63] on this idea in three decades where the hypothesis was proposed for the Ag/AgI system[86]. Once again taking advantage of the ability to create Li/LLZO and Na/NBA interfaces with low interfacial resistances and the excellent chemical stability of the oxide electrolytes, the couplings between cell resistance, applied current density, and external stack pressure are explored in this chapter.

The following chapter sections are published in modified forms as:

I. Michael J. Wang, Rishav Choudhury, & Jeff Sakamoto, Characterizing the Li-Solid-Electrolyte Interface Dynamics as a Function of Stack Pressure and Current Density. *Joule* **3**, 2165–2178 (2019).

4.1 Characterizing the Li-Solid-Electrolyte Interface Dynamics as a Function of Stack Pressure and Current Density

4.1.1 Introduction

Li metal has long been sought after as a potential anode material for next-generation Li-ion batteries due to its high energy density, 4x greater than the volumetric energy density of graphite anodes[29,38,39,87]. However, the tendency for Li metal to form dendrites and in some cases form solid electrolyte interphase(s) when used in liquid electrolytes has limited widespread adoption for rechargeable batteries. All-solid-state batteries present a potential solution for enabling Li metal anodes, by physically stabilizing the Li electrode interface, while also eliminating the use of flammable liquid electrolytes, making solid-state systems promising for the next-generation of electric vehicle batteries. However, despite the presence of a solid electrolyte, it has been widely demonstrated that Li filaments are able to propagate through a variety of different solid-state electrolytes, including polymers, sulfides, and oxides[20,23,24]. Due to this challenge, a significant emphasis has been placed on studying the interface between the solid electrolyte and Li metal during Li plating and subsequently, the rate at which Li plates in solid-state systems has steadily been improving to current densities above 1mA cm^{-2}[29,42,88]. As these current densities will define the maximum power densities of solid-state batteries, these steady improvements provide optimistic outlooks on the rate capabilities of Li metal during charging. However, equally as important as charge is discharge or the Li stripping of Li.

Due to the inherent differences in the nature of solid-solid interfaces from solid-liquid interfaces, the kinetics and mechanics of the solid electrolyte and Li metal during Li stripping are not well understood. It has been demonstrated in the literature that there are a variety of factors that play a role in the ability of symmetric Li/solid-electrolyte cells to stably cycle. Many of those factors are strongly related to the interfacial resistance (R_{int}) between Li and the electrolyte, which is a representative value for the quality of chemical and mechanical interactions between the two materials[28,87,89,90]. Some known factors are the chemical composition at the interface, the surface morphology (including the presence of Li filaments), and the external temperature and pressure[24,35,36,88,90]. Given that deviation from Ohmic behavior during DC cycling and changes in the AC impedance after cycling have commonly been observed in the cycling of symmetric Li/solid-electrolyte cells[29,32,35,36,45], it is clear that dynamic changes at the Li-metal/solid-electrolyte interface play an important role in the performance of the cell and its ability to stably cycle over a large number of cycles. In terms of morphological changes, Li filament initiation and propagation has been clearly demonstrated in numerous studies during Li plating[20,23,24]. However, because the interface is buried, it is difficult to observe morphological changes on the Li stripping side. It has been hypothesized that Li stripping at high rates may lead to the formation of Kirkendall voids, which may arise from the insufficient rate of mass transport from diffusion and applied pressure to replenish the Li being dissolved into the solid-electrolyte[45,50,62]. This phenomenon has previously been well-studied and discussed for the Ag-metal/solid-electrolyte system[91,92]. Although this phenomenon has long been suggested to be relevant in the Li-metal/solid-electrolyte system, few studies have addressed it in detail. However, given the considerable differences in the homologous temperature and yield strength between Li-metal and Ag-metal, it is important to characterize the mechanics of void formation in Li-metal systems as well. The formation of these voids at the interface essentially increases the porosity and/or surface roughness of the Li at the interface, consequently reducing the contact area between the two interfaces and thus increasing the R_{int} as described by the equation:

$$R = \frac{\rho l}{A} \tag{4.1}$$

where R is the resistance, ρ is the resistivity, l is the length, and A is the area. However, due to the nature of the two-electrode cell configuration, that is typically used to characterize cycling behavior, it is not possible to isolate stripping and plating phenomena. It is also difficult to conclusively isolate morphological changes at the interface to changes in the R_{int} without the ability to consistently achieve high-quality Li/electrolyte interfaces with low R_{int}.

Based on this hypothesis, the formation and prevention of void formation during Li stripping should be drastically affected by the external operating conditions, namely the stack pressure applied to the cell. In this study, the effects of stack pressure on the electrochemical behavior in symmetric Li-metal/solid-electrolyte cells are evaluated *in operando*. The garnet $Li_7La_3Zr_2O_{12}$ (LLZO) electrolyte was used as a model system, due to its relevance in the literature. LLZO not only exhibits high conductivity and a relatively high elastic modulus compared to Li metal but is also stable against metallic Li. This eliminates the possibility of significant chemical reactivity at the interface, which may occur in other electrolytes, such as in sulfides or perovskites. Furthermore, it has been demonstrated that the LLZO electrolyte can be synthesized at high relative densities (>95%) and low R_{int} without the need for interfacial modifications[45,54], and have well defined regimes for stable and unstable Li plating[29,42].

This study utilizes a unique mechanical testing platform contained within an inert environment to couple electrochemical and mechanical behavior. Symmetric Li-LLZO cells are cycled under galvanostatic conditions over a range of current densities while the stack pressure is varied *in operando*, and the DC behavior is coupled with AC techniques, namely electrochemical impedance spectroscopy (EIS). Furthermore, by integrating a reference electrode into the cell, the electrochemical behavior during Li plating and stripping was decoupled, providing further insights on the contributions of each electrode toward the overall electrochemical behavior. The results suggest that deviation from Ohmic behavior during galvanostatic cycling is primarily attributed to the electrode undergoing Li stripping, which strongly supports the void formation hypothesis presented by Koshikawa *et al.*[45] and by Krauskpof *et al.*[62], who recently investigated the transport limitations under stripping currents. Furthermore, since void formation at the interface is primarily an issue of mechanical compliance under these operating conditions, the reversibility and prevention of void formation is demonstrated. This not only offers new understanding about the kinetics and mechanics at the Li-metal/solid-electrolyte interface, but also provides a practical framework for the operating conditions of future all-solid-state batteries with high power densities.

4.1.2 Experimental

4.1.2.1 Materials synthesis and cell assembly

LLZO pellets of the composition, $Li_{6.5}La_3Zr_{1.5}Ta_{0.5}O_{12}$ (LLZO), were synthesized by rapid-induction hot-pressing, as previously reported[29,42] and cut to a thickness of ~1.3 mm on a diamond saw. The pellets were then polished with sandpaper and diamond pastes of varying grits to a final polish using 0.1 µm diamond paste using a Buehler EcoMet250 automatic polisher. The LLZO pellets were stored in an Ar-filled glovebox and heat-treated at 400°C for 3 hours to remove Li_2CO_3 surface contaminations. In order to fabricate symmetric cells, 750 µm thick Li metal foil (Alfa Aesar, Ward Hill, MA) was pressed onto both sides of the pellet under a load of 3.2 MPa and then heated to ~170°C under a load of ~1MPa to improve interfacial contact.

In order to incorporate a third electrode, a symmetric cell was first fabricated using the methods described using a 5.7 mm thick LLZO billet instead of a 1.3 mm pellet. To incorporate the reference electrode, a diamond saw was used to create a third face on the LLZO pellet, perpendicular to both the top and bottom faces. Using an Angstrom Engineering NexDep sputterer, a ~200 nm thick Ni electrode was sputtered onto the third face and a Ni foil tab was attached to the sputtered Ni electrode with conductive silver paste. EIS was used to confirm that the reference electrode was electrically isolated from both the working and counter electrodes.

4.1.2.2 Mechanical testing

An Instron 5944 tension/compression testing unit inside an Ar-filled glovebox was used to dynamically control the stack pressure on the Li-LLZO cells. To measure the potential response as a function of stack pressure, the cells began at a stack pressure of 3.2 MPa and a unidirectional constant current was applied for 5 hrs to allow for the system to reach a steady-state. Without removing the applied current, at the end of the 5 hrs, the stack pressure was decreased by 0.4 MPa at a rate of 1 mm min^{-1} and then the cell was held at the subsequent stack pressure for another 5 hrs. This process was repeated until a 0 MPa stack pressure was reached. A maximum stack pressure of 3.2 MPa was chosen to be comparable with past studies[27,42,89]. For observing the potential response under stack pressure cycling, a constant current of 0.1 mA cm^{-2} was applied while both increasing and decreasing the stack pressure between 1.2 MPa and 2.4 MPa. Each pressure step was held for 2 hrs before increasing or decreasing the stack pressure by 0.4 MPa and repeating for a total of 25 steps.

4.1.2.3 Electrochemical testing

Galvanostatic cycling and EIS were conducted using a Biologic VMP-300 galvanostat/potentiostat. All cycling was performed within the Instron testing apparatus while cycling at current densities between 0.05 mA cm^{-2} and 0.4 mA cm^{-2}. This range in current density was chosen to be low enough such that Li filaments should not initiate in the LLZO and introduce extraneous variables. EIS was conducted at frequencies from 7 MHz to 1 Hz with a perturbation voltage of 10 mV and equivalent circuit modeling was performed to deconvolute R_{int} from the bulk and grain boundary contributions to the resistance. Using a modified Huggins model, the EIS spectra were fit to an equivalent circuit containing three RC components in series, representing the bulk, grain boundary, and interfacial contributions of the resistance. Constant phase elements were used instead of capacitors to account for variable time constants.

4.1.3 Results & Discussion

4.1.3.1 Galvanostatic cycling under dynamic stack pressure conditions

In order to determine the effect of stack pressure on the potential behavior during cycling, a stack pressure of 3.2 MPa was applied to symmetric Li-LLZO cells and then a unidirectional constant current was applied. A schematic of the testing conditions is shown in Figure 4.1. After 5hrs of cycling, the stack pressure was reduced by 0.4 MPa and the corresponding potential response was monitored. The stack pressure was reduced by 0.4 MPa every 5 hours while the potential was measured. The potential response under this type of loading profile is shown in Figure 4.2 for current densities of 0.05 mA cm^{-2}, 0.1 mA cm^{-2}, 0.2 mA cm^{-2}, and 0.4 mA cm^{-2}. In order to eliminate the variability in total cell resistance, the potential was normalized by the initial potential (E_0) at the start of cycling. For each cell it can be seen that the potential response is relatively flat at higher stack pressures, indicating negligible change in the total resistance of the cell. However, when cycling at 0.1 mA cm^{-2} and higher, a dramatic increase in the potential is observed at lower stack pressures. Furthermore, this stack pressure is observed to increase with increasing current densities. Loosely defining this pressure as the “critical stack pressure”, the measured “critical stack pressures” for cycling at 0.1 mA cm^{-2}, 0.2 mA cm^{-2}, and 0.4 mA cm^{-2} are 0.4 MPa, 1.2 MPa, and 2.0 MPa respectively. In comparison to the higher current densities, the cell cycled at 0.05mA cm^{-2} does not exhibit a drastic potential increase at any stack pressure, although a noticeable amount of polarization is observed at the end of the 0.4 MPa step. The dependence of the observed polarization on both the stack pressure and current density suggest that this phenomenon is strongly correlated to a Li flux imbalance near the Li-LLZO interface, as previously discussed[29]. For the majority of this work, Ta-stabilized LLZO of the composition $Li_{6.5}La_3Zr_{1.5}Ta_{0.5}O_{12}$, was used, however, the same test was performed with Al-stabilized LLZO of the composition $Li_{6.25}Al_{0.25}La_3Zr_2O_{12}$ and the same behavior was observed at the same stack pressures. This independence of the polarization behavior from the electrolyte composition further suggests that this behavior is primarily caused by the Li electrode, rather than the electrolyte. This comparison between Ta-stabilized and Al-stabilized LLZO is included in Figure 4.3.

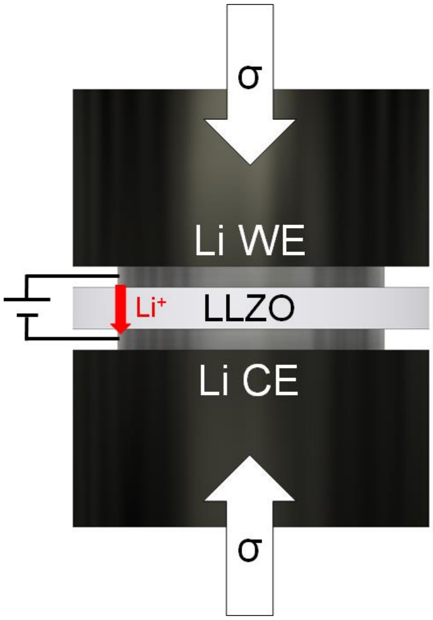

Figure 4.1: Schematic of a symmetric Li-LLZO cell with Li metal as both the working and counter electrode. The cell is cycling within a mechanical testing unit that controls the applied stack pressure.

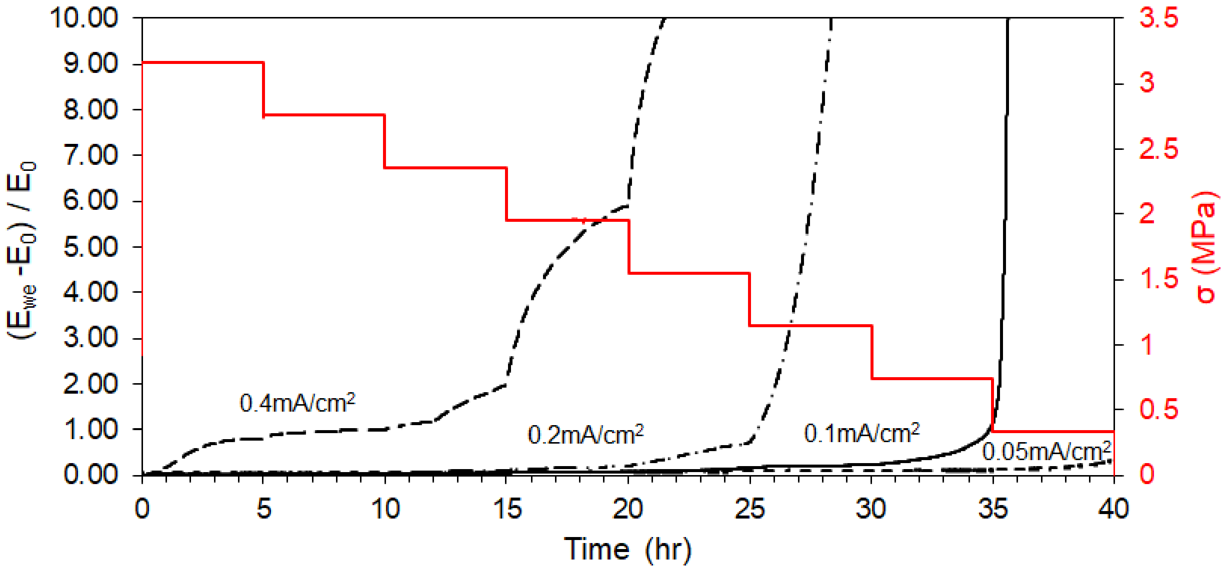

Figure 4.2: The potential response to a constant current density at varying stack pressures. The potential is normalized to the initial potential at the beginning of the constant current cycling. The potential responses for four different current densities are shown.

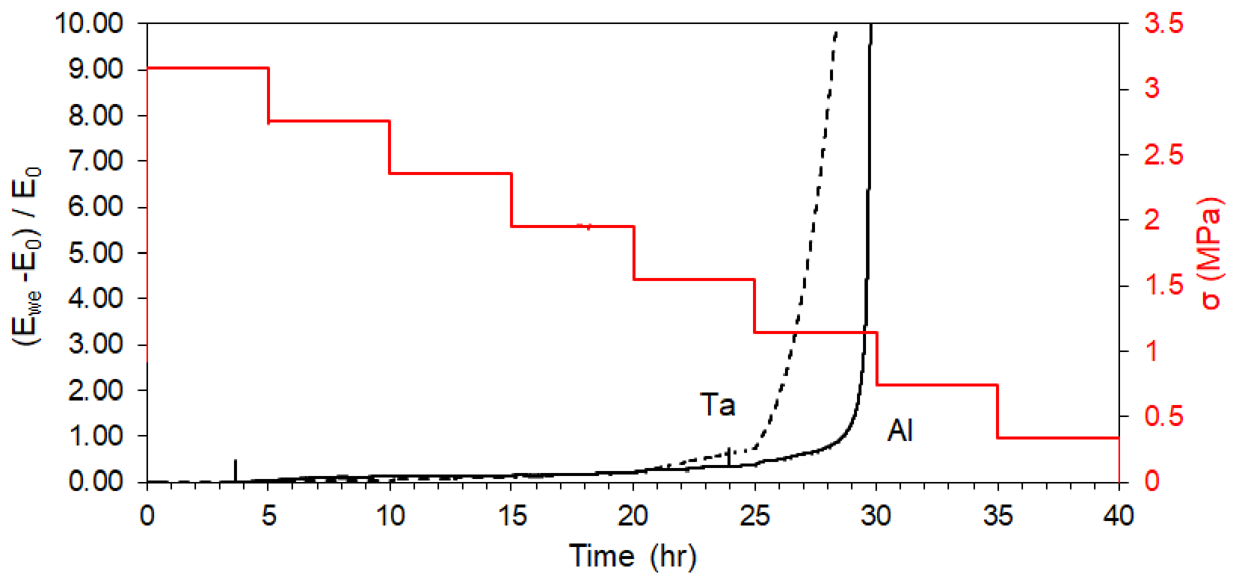

Figure 4.3: A comparison of the potential response to a constant current density of 0.2 mA cm^{-2} for Ta-stabilized LLZO ($Li_{6.5}La_3Zr_{1.5}Ta_{0.5}O_{12}$) and Al-stabilized LLZO ($Li_{6.25}Al_{0.25}La_3Zr_2O_{12}$). The same polarization behavior is observed for both compositions at the same stack pressures.

4.1.3.2 Reversibility of void-induced polarization

In order to investigate the potential behavior just above the "critical stack pressure", a cell was cycled at 0.1 mA cm^{-2} at both increasing and decreasing stack pressures between 1.2 and 2.4 MPa. In order to avoid unstable polarization that will prematurely end the test, the "critical stack pressure" was not exceeded. Furthermore, EIS was conducted at the end of each step, with the AC signal superimposed onto the DC signal. Since the stack pressure is above the "critical stack pressure", it is assumed that the interface is in dynamic equilibrium at the end of each hold step, and therefore the interface morphologies are not changing significantly over the course of the EIS measurement. This would not be possible if the AC signal was not superimposed onto the DC signal, as the presence of stack pressure combined with the absence of Li dissolution would not be representative of the interface morphology during cycling.

Figure 4.4a shows the potential response while increasing and decrease the stack pressure under constant current conditions. As expected, slight increases are observed as the stack pressure is decreased, but the changes are stable and show relatively flat responses near the end of the hold step. Similarly, slight decreases in potential are observed as the stack pressure is increased. Figure 4.4b, shows a representative EIS spectra at 2.4 MPa in comparison to an EIS spectra taken at 1.2 MPa. It is noticeable that the high frequency regime is nearly identical in spectra, which suggests that there is no change in the bulk or grain boundary contribution of the electrolyte. The only observable difference between the spectra taken at high stack pressure versus the spectra taken at low stack pressure is in the low frequency regime. Given that these stack pressures were chosen to be above the "critical stack pressure", there should be minimal changes in area due to void formation, as any significant areal change should affect both the high and low frequency regimes. Fitting of the spectra to the equivalent circuit model, the characteristic capacitance value of the changing low frequency semi-circle is $\sim 10^{-3}$ F, which corresponds to an electrochemical reaction according to Irvine *et al.*[16]. Because these AC measurements were performed *in operando*, the presence of this low frequency semi-circle is consistent with the fact that Li is actively being plated/stripped throughout the measurement. This suggests that above the "critical stack pressure" there is minimal change in bulk, grain boundary, and interfacial resistance due to loss of contact area. Instead, it suggests that the electrochemical kinetics at the interface may be pressure dependent with the low frequency semi-circle being large at 1.2 MPa and small at 2.4 MPa. These kinetics may be related to vacancy or adatom motion of Li near the interface, as recently suggested by Krauskopf *et al.*[62]. However, these changes are relatively reversible as a function of stack pressure, as exhibited in Figure 4.4c.

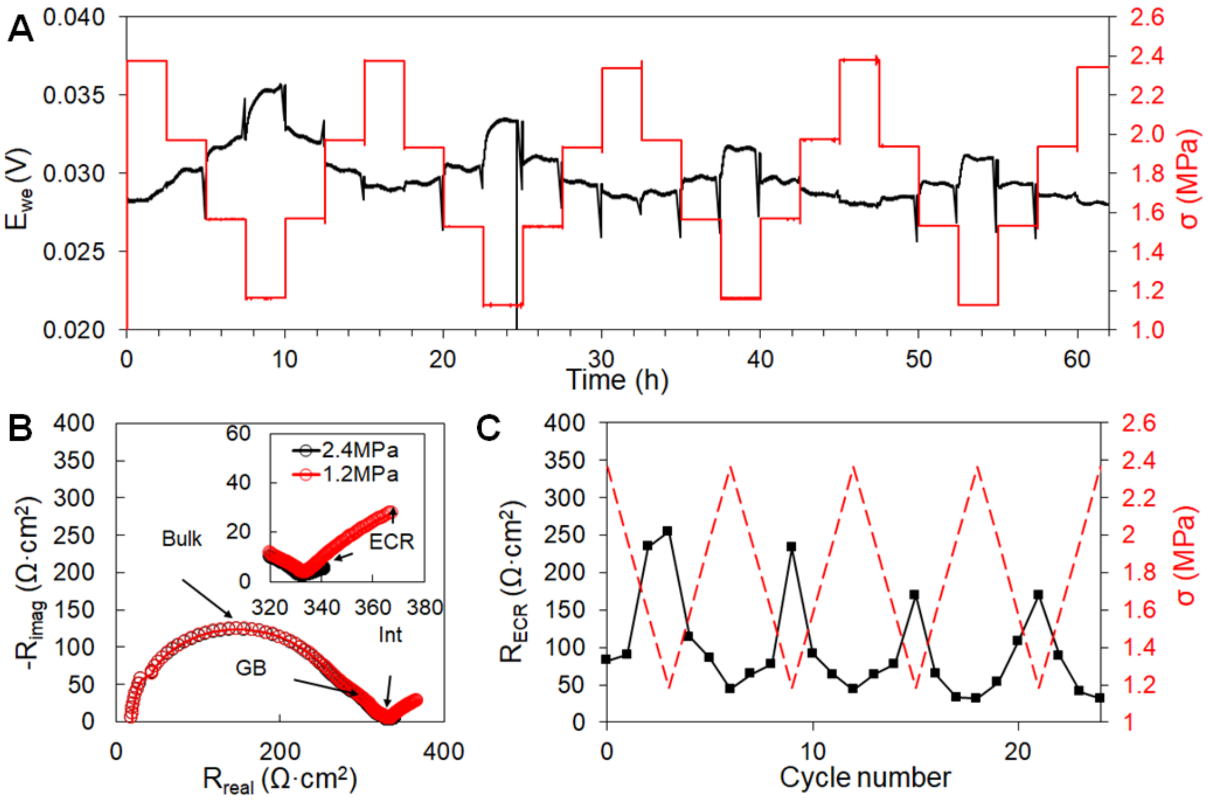

Figure 4.4: a) The potential response under a constant current of 0.1mA cm^{-2} while increasing and decreasing the stack pressure above the "critical stack pressure". Artifacts of the AC signal superimposed onto the DC signal are noticeable at the end of each pressure step. b) Representative EIS spectra at high (2.4MPa) and low (1.2MPa) stack pressure: inset highlights low frequency electrochemical reaction (ECR) behavior. c) The R_{int} calculated from the EIS taken at the end of each pressure step for each cycle.

4.1.3.3 Decoupling Li stripping from plating

Although it has been hypothesized that void formation is the primary reason for increases in R_{int} and subsequent polarization during cycling[45], conventional two-electrode configurations are unable to deconvolute the contributions of Li plating and Li stripping in symmetric cells, and therefore, it is difficult to conclusively isolate changes in R_{int} to the formation of voids. In order to circumvent this limitation, the test performed in Figure 4.2 was repeated but with the inclusion of a Ni reference electrode. A schematic of the three-electrode configuration is shown in Figure 4.5.

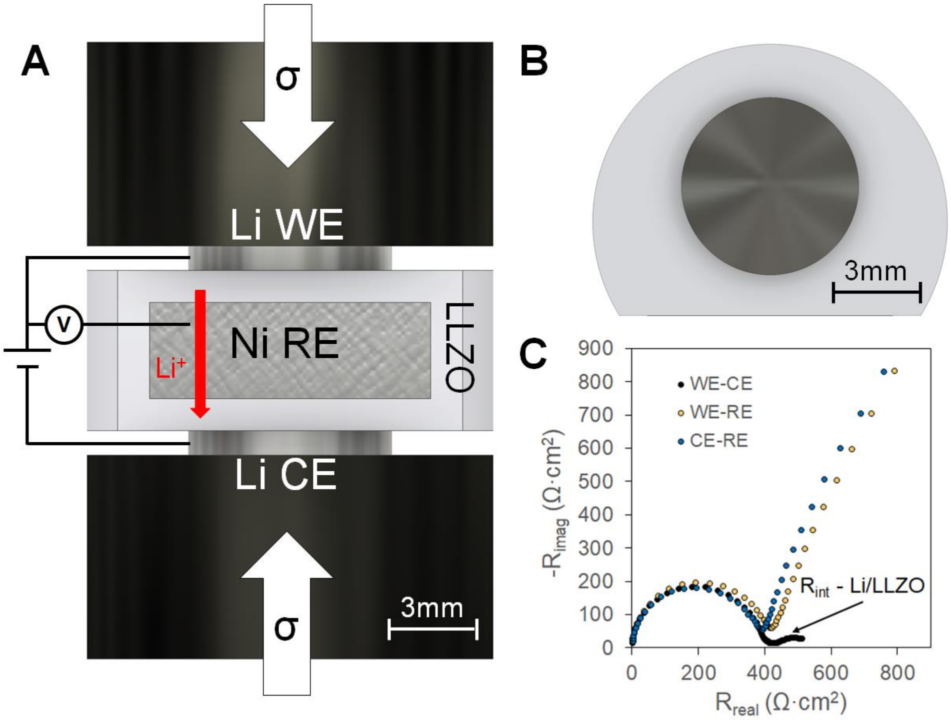

Figure 4.5: a) Schematic of the three-electrode setup with a Ni reference electrode. b) Top-view illustrating the geometry of the LLZO billet with a third face cut perpendicular to the billet face. c) EIS between the three different electrodes, showing blocking behavior for the Li-Ni configurations and non-blocking behavior for the Li-Li configurations.

Because it is completely blocking to Li-ions (does not alloy with Li) at ambient temperatures[93] and unreactive against LLZO, Ni is an ideal electrode to use as a reference. This is demonstrated in Figure 4.5c, which shows non-blocking behavior between the WE and CE and blocking behavior between the WE and reference and CE and reference. The three spectra also show that the three electrodes are electrically isolated from each other. Figure 4.6 shows a symmetric Li-LLZO cell where the Li is being stripped from the working electrode (WE) and plated at the counter electrode (CE) at a current density of 0.2 mA cm^{-2}. Similar to Figure 4.2, the potential difference between the WE and CE is nearly flat at high stack pressures, and then dramatically increases at 1.2 MPa. However, with the addition of the Ni reference electrode, the potential of the WE and the CE can be deconvoluted and it can be seen that a noticeable increase in the potential can be observed on the WE around 2 MPa, while the CE remains flat.

Continuing to lower stack pressures, it can be seen that the CE remains flat over the entirety of the test, while the WE continues to increase and follows the same trend as observed in Figure 4.2. A closer look at the potential changes of the WE and CE around 2 MPa is shown in Figure 4.7. These trends strongly support the hypothesis that the observed polarization is entirely due to the formation of voids at the Li stripping interface, eliminating the possibility that the surface roughness of the plated Li is significantly contributing to any changes in R_{int}.

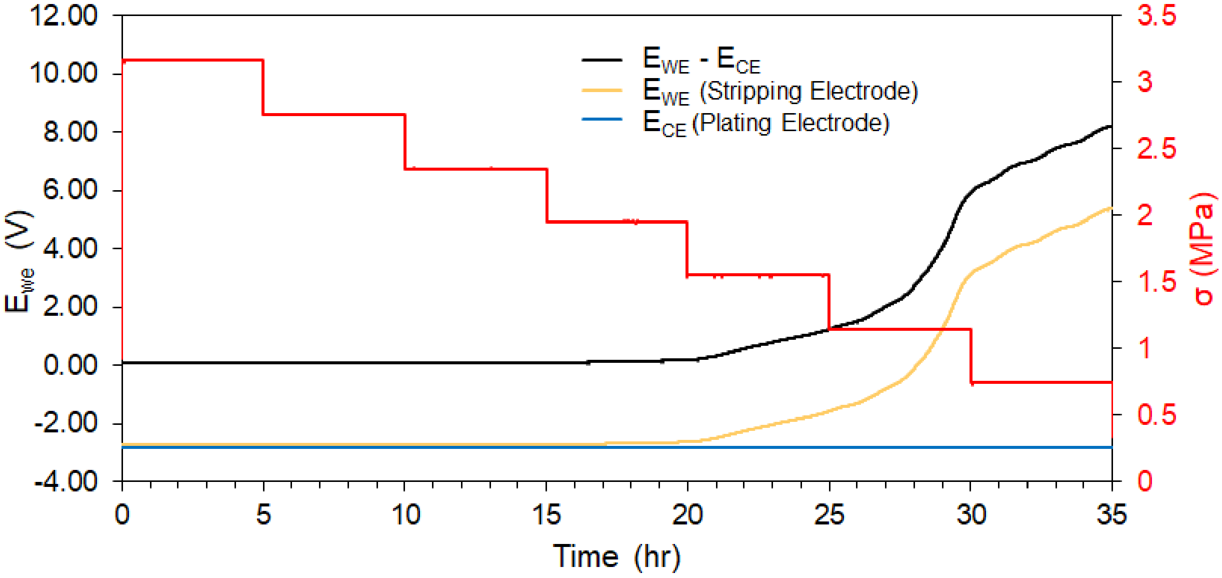

Figure 4.6: Potential response under a constant current density of 0.2mA cm^{-2} and decreasing stack pressures. The usage of the Ni reference electrode allows for the decoupling of the Li stripping electrode (WE) and the Li plating electrode (CE).

Another noticeable feature in the potential responses in both Figures 4.2 and 4.6, is that the potential difference between WE and CE increased up to 9 V before hitting the potentiostat cut-off. Even at potential differences of 9 V, no short-circuiting is observed. This implies that neither the polarization on the WE electrode nor the potential difference play a role in the formation of Li filaments, and instead the absolute potential of the CE is the main factor in Li filament initiation. This is in agreement with the observations of Garcia-Mendez *et al.*[94], who hypothesized that Li filament initiation is governed by an underpotential on the Li plating electrode, which results in Li precipitation due to the overlap of valence and conduction bands.

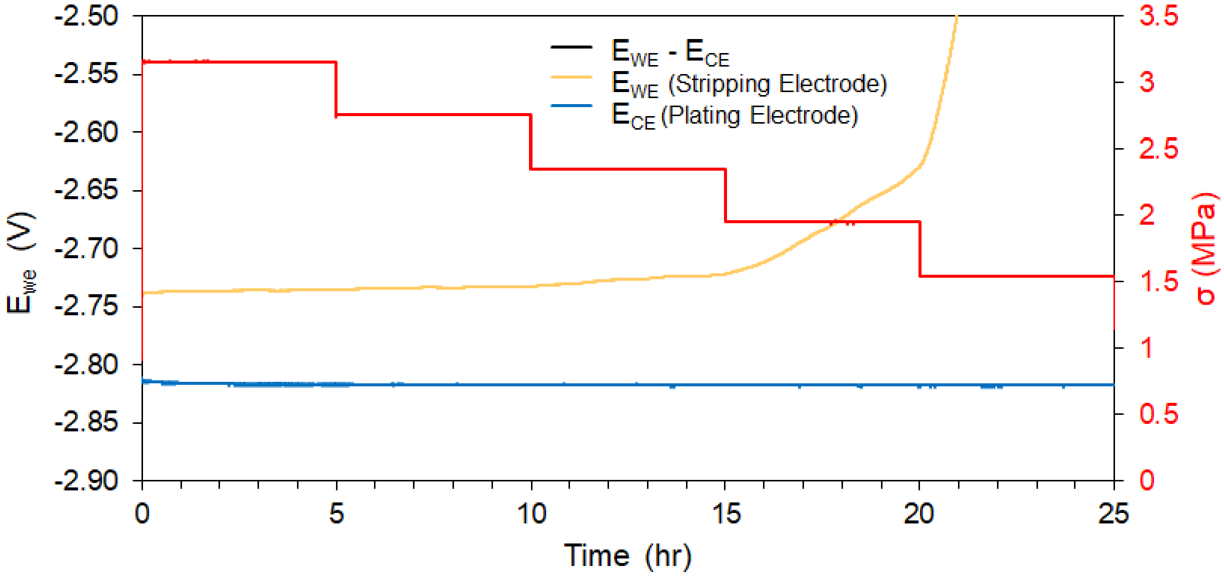

Figure 4.7: The potential response near the open-circuit voltage (2.78V measured for Li vs Ni) in Figure 4.5, highlighting the polarization on the WE and the lack of change on the CE.

4.1.3.4 Electrochemical void formation mechanism and prevention

The results presented here demonstrate a clear correlation between stack pressure, current density, and polarization during cycling that are in good agreement with Koshikawa *et al.*, Krauskopf *et al.*, and others[24,45,62]. With the decoupling of the contributions of the stripping and plating electrode, it is now clear that surface roughening due to Li plating has a negligible impact on the total resistance of the cell, while surface roughening from Li stripping has major impacts. As previously discussed, if the flux of Li being pushed toward the Li-LLZO interface is insufficient to replenish the Li being dissolved into the LLZO, voids will form at the interface, reducing the contact area and therefore increasing the resistance and overpotential needed to supply a constant current. A demonstration of this phenomenon is shown in Figure 4.8. In Figure 4.8, two symmetric Li-LLZO cells are cycled at a current density of 0.2 mA cm^{-2}, with one cycled at a stack pressure of 3.2 MPa and the other cycled at a stack pressure of 0.4 MPa.

Given that the amount of Li being cycled is relatively small in comparison to Figure 4.2, the polarization is not as drastic, however, the cell cycling at low stack pressure exhibits noticeably more polarization than the cell cycling at high stack pressure and the polarization is observed and approximately equal for both polarities. Meanwhile, the cell cycling at high stack pressures exhibits relatively flat potential responses as the effects of void formation are significantly smaller. Furthermore, in the cell cycling at low stack pressure, the magnitude of the overpotential seemingly increases with cycle number. Although there is a 15min rest in between each cycle, there is likely insufficient time, temperature, and pressure to recreate an intimate contact and good adhesion between the Li and LLZO. Therefore, it is likely easier for contact loss to occur, resulting in quicker void formation and higher overpotentials with increasing cycle number.

In comparison to other studies in the literature, these observations are consistent with reports of stable cell cycling with similar stack pressures and current densities. In these studies, noticeable polarization is observed at higher current densities (>0.2-0.5 mA cm^{-2})[29,36,62] and flat potential responses are observed at lower current densities. Although stack pressures are not widely reported, other studies presumably cycle at lower stack pressures (<1 MPa), and similarly observe noticeable polarization at lower current densities. These lower current densities are reasonable given the current-pressure regimes defined in this study[27,28,95]. Many of the studies which demonstrate low overpotentials at high currents and/or at low stack pressures incorporate interfacial layers between the Li and LLZO, which presumably affects the Li mobility and interface mechanics[35,96].

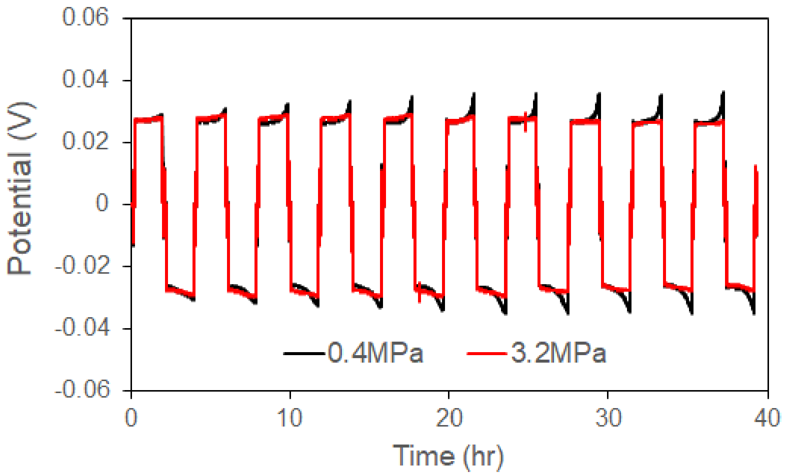

Figure 4.8: The potential response to both Li stripping and plating at a constant current density of 0.2mA cm^{-2} at a representative high stack pressure and representative low stack pressure. 0.35mA cm^{-2} of Li is stripped/plated each cycle.

In the context of this work, the flux of Li moving toward the interface is controlled by the stack pressure, which creeps Li toward the interface. Therefore, the measured "critical stack pressures" can be assumed to be the point at which the flux of incoming Li from the applied stack pressure is equal to the flux of Li dissolving and migrating through the LLZO. Therefore, above the "critical stack pressure", the stack pressure is enough to sufficiently creep Li toward the interface, preventing significant void formation. Below the "critical stack pressure", the flux balance is instead dominated by the flux of Li migrating into the LLZO, in which case the stack pressure is insufficient to replenish the Li at the interface and voids can readily form and grow. This is supported by the dependence of the "critical stack pressure" on the applied current density, as the current density is analogous to the flux of Li dissolution and migration at the interface. Therefore, at higher current densities, a higher stack pressure is necessary to match the higher migration flux. Additionally, the ability to reverse the effects of polarization at relatively low stack pressures by simply increasing the stack pressure strongly suggests that this phenomenon is related to the mechanics of the Li electrode and is purely mechanical in nature, rather than chemical, which would likely not be reversible with stack pressure.

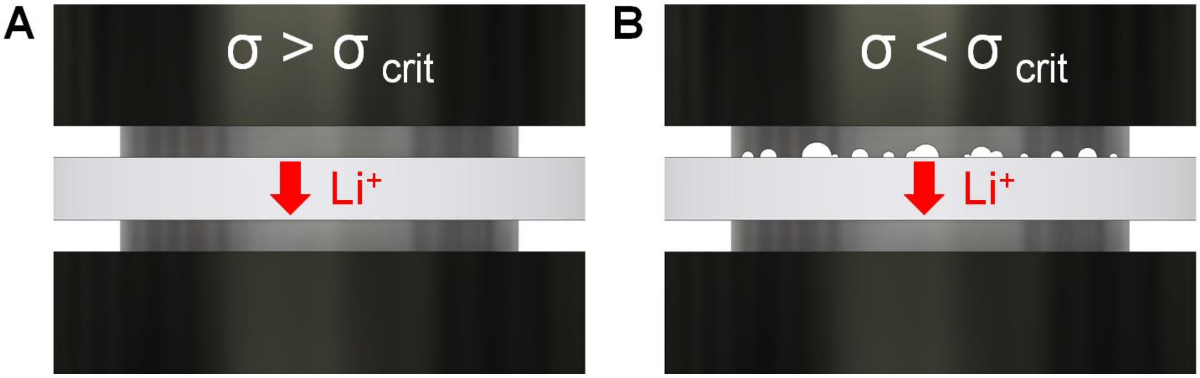

Figure 4.9: a) The proposed microstructure of the Li/electrolyte interface above the "critical stack pressure" where the magnitude of the applied pressure is sufficient to maintain contact between Li and electrolyte. b) The proposed microstructure of the interface below the "critical stack pressure" where the applied pressure is insufficient to replenish the Li at the interface, resulting in void formation at the interface and a subsequent reduction in the contact area.

Although detailed computational models would be necessary to accurately simulate the chemo-mechanical interactions at the Li stripping interface, a first-order estimation can be made based off the balance simply between the current density and creep. Because the ionic transference number of LLZO is ~1, it can be assumed that all of the charge being passed is by means of Li^+ migration and therefore the current density is analogous to a Li flux. Furthermore, since the Li stripping flux causes a change in the electrode thickness, this Li flux and therefore the current density is analogous to a strain rate. The strain rate induced by the current density is given by the equation:

$$\dot{\varepsilon}_j = \frac{\dot{\Delta l}}{l_0} = \frac{\frac{jAM}{\rho FA}}{l_0} = \frac{jM}{\rho F l_0} \tag{4.2}$$

where $\dot{\varepsilon}_j$ is the current-induced strain rate, l_0 is the length, j is the current density, A is the area, M is the molar mass of Li, ρ is the density of Li, and F is Faraday's constant. Meanwhile the generalized form of the strain rate induced by creep is given by:

$$\dot{\varepsilon}_{creep} = A\sigma^m \exp\left(-\frac{Q}{RT}\right) \quad (4.3)$$

where $\dot{\varepsilon}_{creep}$ is the pressure induced strain rate, A is a material parameter, σ is the stress, m is the power-law creep exponent, Q is an activation energy, R is the molar gas constant, and T is the temperature. In recent works, Masias *et al.*[52] and LePage *et al.*[76], have conducted comprehensive characterizations of the mechanical properties of Li metal, and both have concluded that creep in Li metal is governed by power law behavior dominated by dislocation climb (m=6.6)[52,76] at room temperature. An important observation made by Masias *et al.* is that under compression under a constant stress, Li cylinders exhibited a decay in the strain rate with time, which is caused by the barreling of the Li due to the frictional and adhesive forces between the Li and the substrate. For example, after five hours and based on the data from Masias *et al.*, the strain-rate decays by a factor of approximately 10^{-3}-10^{-4}[52]. Using the values provided by LePage *et al.* and Masias *et al.*, the strain-rate at the end of each pressure step can be calculated, assuming a decay of ~10^{-4} due to frictional and adhesive forces at the interface. These values are listed in Table 4.1.

Table 4.1: List of parameters and values for calculating strain rates in Figure 4.10

Parameter	**Symbol**	**Value**	**Reference**
Current - Strain Rate			
Molar mass of Li	M	6.941 g mol^{-1}	-
Density of Li	ρ	0.534 g cm^{-3}	-
Faraday's Constant	F	96485 C mol^{-1}	-
Initial Electrode Thickness	l_0	700 μm	-
Creep – Strain Rate			
Material-specific Creep Parameter (as reported)	A'	7×10^{-37} Pa^{-m} s^{-1}	LePage *et al.*[76]
Material-specific Creep Parameter (accounting for strain-rate decay reported by Masias *et al.*)	A	9×10^{-41} Pa^{-m} s^{-1}	LePage *et al.*, Masias *et al.* [52,76]

Power-law creep exponent	m	6.6	LePage *et al.*, Masias *et al.* [52,76]
Activation Energy	Q	37 kJ mol^{-1}	LePage *et al.*[76]
Molar Gas Constant	R	8.31 J $(mol\ K)^{-1}$	-

In the simplest case, considering only the contributions of creep and current density, the condition for void formation is when:

$$\dot{\varepsilon}_j > \dot{\varepsilon}_{creep} \qquad (4.4)$$

which describes the scenario where Li is being stripped faster than it can be replenished by the applied pressure.

A comparison of the theoretical $\dot{\varepsilon}_j$ and $\dot{\varepsilon}_{creep}$ at the end of each pressure step is shown in Figure 4.10 for a current density of 0.1 mA cm^{-2}. Additionally, assuming the polarization exhibited in Figure 4.2 is dominated by changes in contact area below the “critical stack pressure”, the change in area versus time is calculated by taking the derivative of the curve in Figure 4.2 and superimposed in Figure 4.10. It can be seen that at all stack pressures from 3.2 MPa to 0.8 MPa, $\dot{\varepsilon}_{creep}$ exceeds $\dot{\varepsilon}_j$ and likewise, no noticeable change in contact area is observed. Once $\dot{\varepsilon}_{creep}$ approaches and drops below $\dot{\varepsilon}_j$, a noticeable decrease in the contact area is observed, suggesting the formation of voids, around 0.4 MPa, which is the same pressure at which $\dot{\varepsilon}_j$ first begins to exceed $\dot{\varepsilon}_{creep}$. The same behavior is observed with current densities of 0.05 mA cm^{-2} and 0.2 mA cm^{-2}. However, for 0.4 mA cm^{-2}, noticeable areal changes are observed at 2 MPa, while the $\dot{\varepsilon}_j$ does not dominate until 1.2 MPa. This suggests that this basic model may be sufficient to describe the cycling behavior at low current densities but may involve more complex processes at higher current densities. Once a significant number of voids begin to form, the effective current density should also increase in response to the decreasing contact area, which effectively increases $\dot{\varepsilon}_j$. It may be possible that the statistical likelihood of void nucleation/growth may be higher at higher current densities, which would account for this discrepancy. However, the exact reasoning for this is unclear but may also be related to the strain-rate associated with decreasing the stack pressure, localized current densities due to surface roughness, the pressure dependence on interfacial kinetics, or the presence of frictional and adhesion forces. Additionally, the strain rates here are representative of macroscopic strain, while void nucleation likely occurs on a much more localized scale, which could have drastically different strain fields. Further investigation of the mechanics of Li metal under compression, including further quantification of the creep parameters, as well the development of more in-depth models that can address the multitude of interactions at the Li-LLZO interface would greatly aid in understanding the exact conditions for electrochemical void formation.

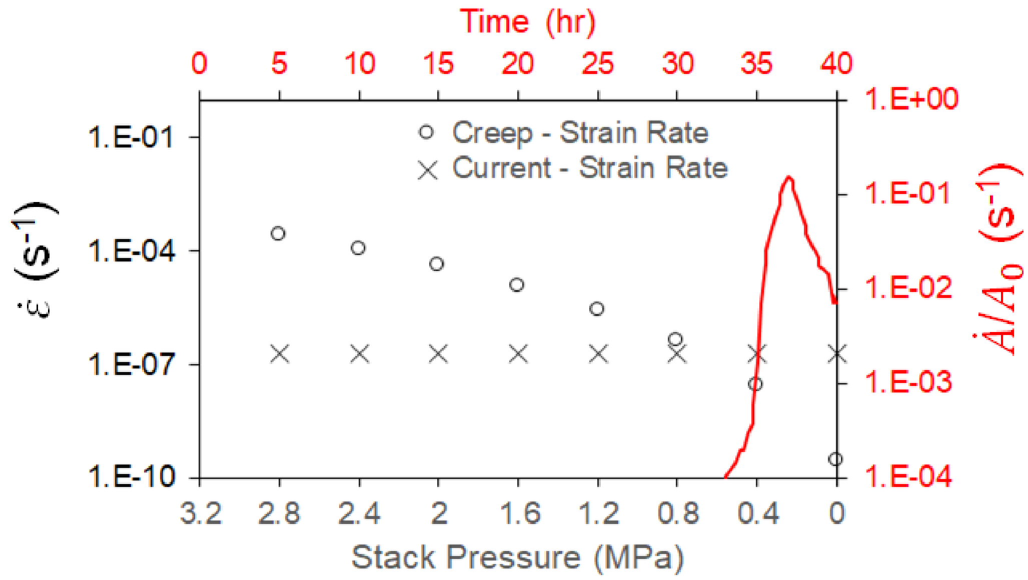

Figure 4.10: Comparison of the pressure-induced strain rate and the current-induced strain rate for cycling at 0.1mA cm^{-2}. The point at which the current-induced strain rate exceeds the pressure-induced strain rate is likely the point at which unstable void growth occurs, as evidenced by a decrease in the contact area, resulting in dramatic polarization.

In the greater context of all-solid-state batteries, the proposed mechanism implies that electrochemical void formation may pose the same challenge in any solid-state system using Li metal anodes, regardless of the electrolyte used. The overpotential required to drive a fixed current in any battery system should ideally be as low as possible, to mitigate the energy required to charge/discharge the battery. Furthermore, it has been suggested that if the voids are not closed before switching the polarity, the reduced contact area will localize the current density upon plating, lead to localized areas of high overpotentials, and can lead to the initiation of Li filaments and short-circuit the cell[45]. Therefore, void formation is clearly a detrimental effect that may significantly reduce the battery efficiency and reduce the cycle life. However, it has been demonstrated here, that voids can only form and cause noticeable effects in the potential behavior at stack pressures below a "critical stack pressure". This suggests that the applied stack pressure may be an important parameter to consider when designing all-solid-state batteries with higher rate capabilities and longer lifetimes. This may also suggest that in order to achieve fast-charging solid-state batteries with Li metal anodes, much higher stack pressures will be required compared to state-of-the-art Li-ion batteries. Current Li-ion batteries are manufactured with stack pressures in the range of 0.1-1 MPa[97,98]. However, in this study, the "critical stack pressure" at a relatively low current density, 0.4 mA cm^{-2}, is as high as 2.0 MPa, which sets an important constraint on the mechanical properties of viable solid-electrolytes. Not only must the electrolyte be able to cycle Li at these high current densities without propagating Li filaments, it must also be robust enough to withstand these high stack pressures. Currently it is also unclear how stack pressures of this magnitude will affect the propagation of Li filaments. It is possible that these high stack pressures are detrimental to the flux imbalance that could lead to filament initiation but conversely may also improve the uniformity of the plated Li. Regardless, the choice of material, the microstructure, and the geometry will ultimately set the upper bound for the maximum tolerable stack pressure and therefore the maximum tolerable stripping current. Although conventional methods for maintaining stack pressure in batteries may not be applicable in these high-pressure regimes, given the higher rigidity (compared to polymer separators) and operating temperature ranges of ceramic electrolytes, novel methods of maintaining higher stack pressures can be developed. Another possible method to prevent void formation is to increase the operating temperature rather than the stack pressure, which will improve the rate of Li creep towards the Li/electrolyte interface, as well as allow for higher tolerable current densities on the plating side[27,29,42]. With these constraints in place, it may be necessary for future studies to strongly consider the temperature and pressure regimes when working with Li metal, as the mechanics and kinetics at the Li/electrolyte interface during both stripping and plating can be dramatically different at elevated pressures and temperatures. Moreover, increasing both Li diffusivity at the interface, perhaps through coatings, and Li creep rates, through metallurgical engineering, are approaches that should be considered to improve the performance of Li metal solid-state batteries. Therefore, in order to achieve all-solid-state batteries with high rate capabilities, it will be necessary to not only consider the stack pressure as a design parameter, but also to consider how the elevated stack pressures and diffusive transport affect the cycling performance and failure of the batteries.

4.1.4 Conclusion

Currently one of the key challenges toward enabling solid-state Li metal batteries is the difficulty in achieving fast rate capabilities due to morphological changes at the Li-metal/solid-electrolyte interface. Although the issue of Li filament initiation and propagation alone has garnered significant interest and emphasis, in order to enable solid-state technology, it is essential to understand both the Li stripping and plating interfaces. In this study, the effects of stack pressure and current density on the potential response during galvanostatic cycling was evaluated. It was observed that below a “critical stack pressure”, dramatic increases in the cell potential was observed and that the “critical stack pressure” increased with increasing current density, from 0.4 MPa at 0.1 mA cm^{-2} to 2.0 MPa at 0.4 mA cm^{-2}. Furthermore, using EIS, the changes in cell potential showed to be reversible above the “critical stack pressure”. By switching to a three-electrode configuration with a Ni reference electrode, the increase in R_{int} with decreasing stack pressure was shown to be entirely isolated to changes on the Li stripping electrode, with negligible changes on the Li plating electrode. The combination of these results supports the hypothesis that this polarization is caused by the formation of voids at the Li/electrolyte interface if the flux of Li towards the interface from diffusion and creep in the Li metal is insufficient to replenish the flux of Li being dissolved and migrated through the LLZO electrolyte. Therefore, in order to minimize the required overpotential to cycle solid-state batteries, it will be important to consider the required stack pressure not only for the prevention of void formation, but also for the selection of viable solid-state electrolytes. Overall, this introduces important parameters and considerations for the design of future solid-state Li-metal batteries, but also motivates the further study and understanding of the mechanics of the Li-metal/solid-electrolyte interface.

4.2 Investigating the Effects of Stack Pressure on the Na-Metal/Solid-Electrolyte Interface

4.2.1 Introduction

Chapter 4.1 discusses the role of external pressure on the cell resistance of a Li/LLZO cell under a constant current. It was demonstrated that low, stable cell resistances could be maintained while cycling at high stack pressures, while at low stack pressures, dramatic increases in the cell resistance were observed. The pressure at which this dramatic increase occurs was shown to be dependent on the applied current density, thus resulting in a current-dependent “critical stack pressure”. Furthermore, it was demonstrated that the observed increase in cell potential while cycling was completely attributed to the formation of voids upon Li stripping, which reduce the contact area at the interface and therefore increase the cell resistance. This coupling between cell resistance, stack pressure, and current density was also observed by others in the literature with a number of other solid-electrolytes coupled with both Li[30,62,63] and Na[31] metal. Significant amounts of contact loss at that interface not only causes catastrophic increases in the cell resistance but can also lead to significant current focusing effects upon switching polarity. These current focusing effects create regions of high current density which can lead to premature short-circuiting at lower current densities.

It was demonstrated in Chapter 3 that the mechanical properties of the alkali metal anode may have profound effects on the tendency for electroplating to induce fracture of the electrolyte and may serve to explain the observed differences in critical current density (CCD) between Li metal and Na metal anodes when coupled with similar oxide electrolytes. It was observed that the critical current density of Na-metal/Na-β”-alumina (NBA) was an order of magnitude higher than that of Li/$Li_7La_3Zr_2O_{12}$ (LLZO). Presumably, since the tendency to form voids under stripping currents also seems to be dependent on the creep response of the metal anode to an externally applied stack pressure, differences in the mechanical properties of the metal anode should also play an important role in the tendency to electrochemically form voids at the electrode/electrolyte interface. As was shown by Jolly *et al.*[31], Na/NBA cells were observed to withstand higher current densities at lower pressures than a Li-based analogue. Due to the higher homologous temperature of Na metal (0.80 T_m) compared to Li metal (0.66 T_m) at room temperature, Na metal is typically softer and flows more easily than Li metal under the same applied stress. Therefore, it is to be expected that Na metal should be less prone to void formation under similar current densities compared to Li metal, as under the same applied stack pressure, it should be easier to replenish depleted Na at the interface while cycling.

This work studies the relationship between current density, cell resistance, and stack pressure in the Na/NBA system. Using identical methodology as was done with Li/LLZO, the "critical stack pressure" is measured in the Na/NBA system at various current densities. Similarly, the potential response under a constant current at varying high stack pressures was examined. Finally, the wetting and re-wetting behavior of Na metal onto NBA under an applied current and dynamic stack pressure conditions is examined.

4.2.2 Experimental Methods

4.2.2.1 Cell assembly

Experiments were conducted using symmetric Na/NBA cells. Spray-dried Li-stabilized Na-β"-alumina powders were prepared by a solid-state synthesis and sintered into 12 mm pellets as described in Chapter 3.2. The resulting pellets were then polished with a series of sandpapers and diamond pastes to a final polish using 0.1 µm diamond paste. Prior to cell assembly, the NBA pellets were then heat-treated in Ar at 900°C to remove surface contaminants, as was described in depth in Chapter 3.2. Na metal foils were made from a Na ingot (99.8% metals basis) (Alfa Aesar #10342) by cold-rolling into the desired thickness (1.5 mm) and then the surfaces were scraped with stainless steel spatulas to remove oxides and other surface contaminants. The foils were then pressed onto both sides of the heat-treated pellets at a pressure of 3.4 MPa.

4.2.2.2 Mechanical and electrochemical methods

Mechanical and electrochemical measurements were conducted using an Instron 5944 tension/compression testing unit inside an Ar-filled glovebox and a Biologic VMP-300 galvanostat/potentiostat respectively. In order to measure the "critical stack pressure", an identical measurement as described in Chapter 4.1.2 was conducted, which first loads the cells to a stack pressure of 3.2 MPa at a rate of 1 mm min^{-1}. A unidirectional constant current is then applied, and the stack pressure is subsequently decreased every 5 hrs. The stack pressure is decreased by 0.4 MPa at a 1 mm min^{-1} rate until a stack pressure of 0 MPa is reached. In these measurements, current densities well below the critical current density were chosen to avoid any potential artifacts from Na metal filament growth. To observe the behavior at high stack pressures, a similar measurement was performed as in Chapter 4.1.2. The cell is cycled at a constant current of 0.1 mA cm^{-2} while the stack pressure starts at 2.4 MPa, decreases by 0.4 MPa every 2 hrs until a value of 1.2 MPa, and then is increased by 0.4 MPa every 2 hrs back to 2.4 MPa and repeated for a total of 32 steps.

Electrochemical impedance spectroscopy (EIS) was conducted at frequencies between 7 MHz and 100 MHz with a perturbation voltage of 20 mV. The resulting spectra were modeled using a modified version of the equivalent circuit shown in Figure 2.3, which contains a single resistor representing uncompensated resistance, bulk resistance, and grain boundary resistance, in series with an inductor (to account for inductive noise) and an RC element representing interfacial resistance. In the RC element, a constant phase element is used instead of the capacitive element to account for varying time constants.

4.2.3 Results & Discussion

4.2.3.1 Potential response to decreasing stack pressure

As was described in Chapter 4.1, the effects of stack pressure were investigated in symmetric Na/NBA cells under an applied constant current density. Beginning at a high stack pressure of 3.2 MPa the stack pressure was periodically decreased every 5 hrs under the constant current density. The resulting potential response at current densities of 0.2 mA cm^{-2}, 0.4 mA cm^{-2}, and 0.8 mA cm^{-2} is shown in Figure 4.11. In order to account for variability in the total cell resistance, the potentials are normalized by the initial potential (E_0) as the current is first applied. It can be seen that at high stack pressures, the potential is relatively flat for all current densities. Eventually, at some low stack pressure at each current density, a sudden dramatic increase in cell polarization is observed. The stack pressure at which this change occurs, increases with increasing current density. This behavior is identical to the behavior observed with the Li/LLZO system as previously described in Chapter 4.1, which is also shown in Figure 4.11. However, compared to the Li/LLZO behavior, the stack pressures at which the onset of polarization was observed, previously dubbed as the "critical stack pressure", are consistently lower in the Na/NBA system. The "critical stack pressures" for the Na/NBA system are 0.8 MPa, 1.6 MPa, and 2.0 MPa at 0.2 mA cm^{-2}, 0.4 mA cm^{-2}, and 0.8 mA cm^{-2} respectively, while the "critical stack pressure" for the Li/LLZO system was measured to be 0.4 MPa, 1.2 MPa, and 2.0 MPa at 0.1 mA cm^{-2}, 0.2 mA cm^{-2}, and 0.4 mA cm^{-2} respectively. This was also observed by Jolly *et al.*[31]. The dramatic onset of polarization was shown in Chapter 4.1 to be isolated to the Li stripping electrode[63], which strongly suggests that the increase in cell resistance is attributed to void formation which can significantly reduce the electrode/electrolyte contact area. In this case, this suggests that the Na/NBA system can tolerate higher current densities than the

Li/LLZO system at identical stack pressures without loss of contact area. Alternatively, it suggests that lower stack pressures are required to maintain low overpotentials with Na metal systems. This is likely due to the lower yield stress and flow stresses for Na metal, which allow for the Na metal under an external stack pressure to flow toward the NBA interface more easily. This would require higher current densities to completely deplete the interface, therefore making it more difficult for voids to form.

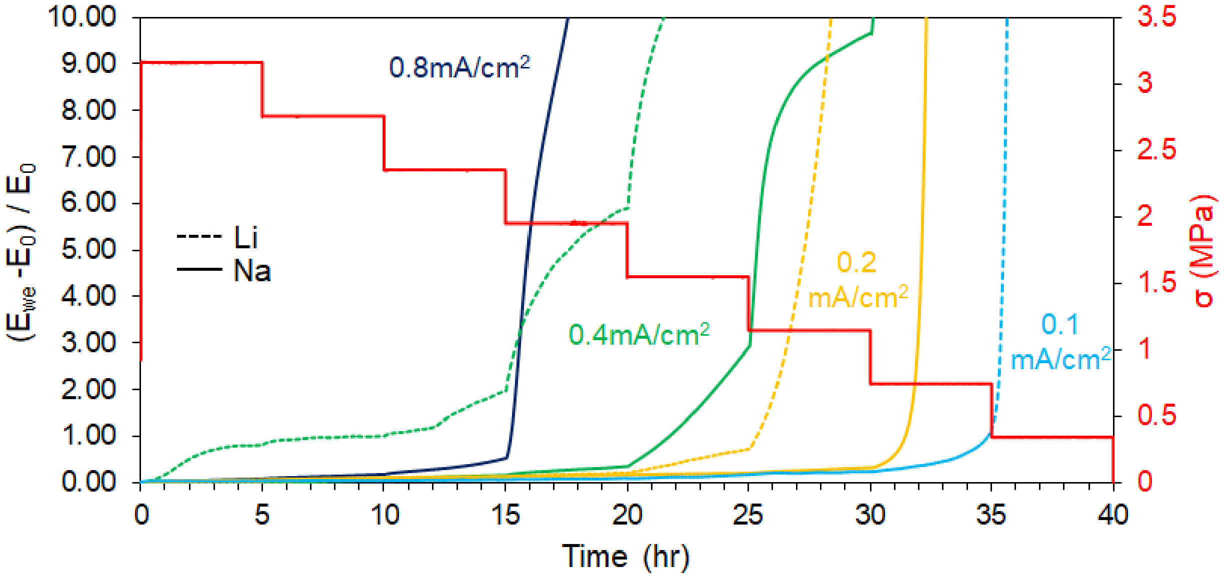

Figure 4.11: The potential response as a function of stack pressure at constant current density. The potential response for the Na/NBA is shown in comparison to the potential response for Li/LLZO, reproduced from Figure 4.2.

4.2.3.2 Void closure and reversibility at low stack pressure

In the case of Li/LLZO, higher temperatures are often required for the Li metal to completely wet the LLZO surface and attain intimate surface contact. This would imply that once voids form, de-wetting the Li from the LLZO, high temperatures would presumably be required to re-wet the Li to the LLZO surface. However, with the Na/NBA system, it was observed that higher temperatures are not required to achieve low interfacial resistances and thus are assembled simply by applying the Na metal electrodes with high pressures at room temperature. Therefore, it may be possible for Na to re-wet the NBA surface once voids form by simply increasing the stack pressure. The feasibility of this was assessed by dropping the stack pressure below the "critical stack pressure" under a current of 0.4 mA cm^{-2} to allow voids to form and then subsequently bringing the stack pressure back to 3.2 MPa. The potential response is shown in Figure 4.12. The onset of polarization at ~2 MPa indicates the formation and presence of voids at the interface. Once the pressure is returned to 3.2 MPa, it can be seen that the potential drops, indicating a decrease in the cell resistance. However, the potential does not completely recover to its original value, suggesting that while some of the contact area has been recovered, the Na has not completely re-wet the NBA surface to the same degree as it originally was. This is unexpected given that similar pressures are applied to wet the Na to the NBA during the initial cell assembly, but after cycling and de-wetting from void formation, returning the system to high stack pressures cannot re-wet the Na to the NBA.

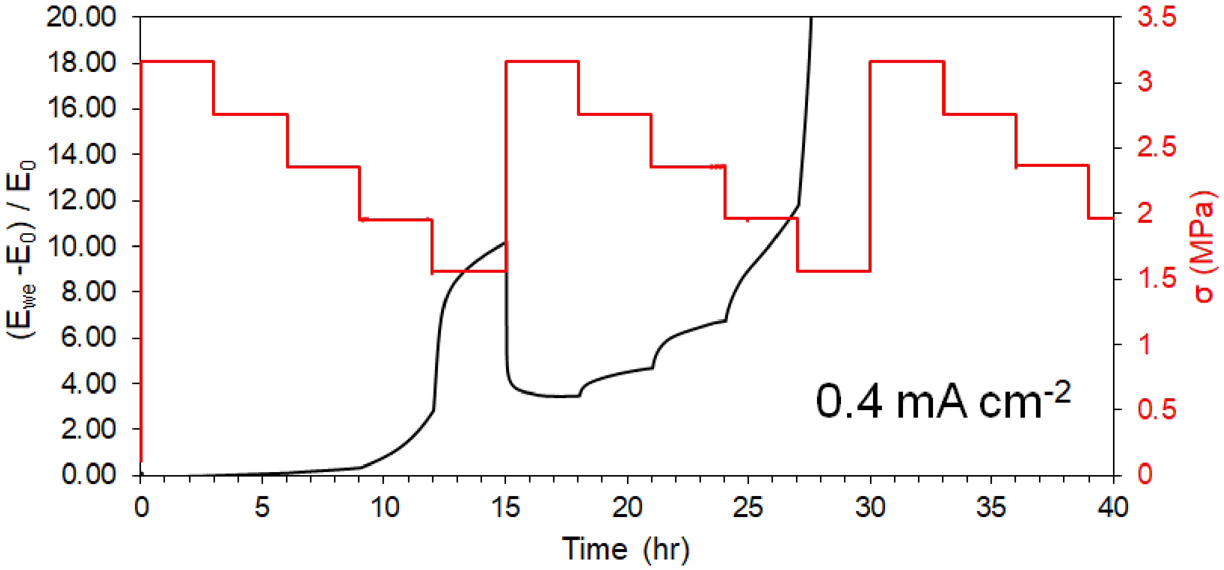

Figure 4.12: The potential response after voids begin to form and then the stack pressure is significantly increased in attempts to re-wet the Na to the NBA surface.

4.2.3.3 Effects and reversibility at high stack pressure

To further investigate the wetting phenomenon, the potential response at high stack pressures was investigated. It was demonstrated in Chapter X that in the Li/LLZO system at high stack pressures, while no dramatic polarization was observed, it was observed that small increases in cell potential occurred as the stack pressure decreased. However, using *in operando* EIS, these small changes were observed to be reversible at high stack pressures, pointing to a potential pressure-dependent kinetic phenomenon at the interface. Similar measurements were conducted for the Na/NBA system, under current density of 0.1 mA cm^{-2} and cycling between stack pressures of 2.4 MPa and 1.2 MPa. Figure 4.13 shows the potential response, which shows that at high stack pressures, there is a gradual, steady increase in the potential throughout the measurements which seems to have negligible contribution from the changing stack pressure. This behavior is different from the observed behavior in the Li/LLZO system, but it can be seen using *in operando* EIS that it stems from an irreversible increase isolated to the interfacial resistance. It was also observed that this increase occurs more rapidly at higher current density. The dependence on the experimental parameters and the isolation of the increase to the interfacial resistance suggests that the increase is caused by passivation of the buried interface. This can be explained by the mechanism proposed by Maslyn *et al.*[25], who demonstrated that as the metal is depleted near the interface via the stripping current, additional metal is moved towrd the interface and impurities are also dragged along. Once the impurities reach the surface, they cannot permeate the electrolyte nor can they move against the flow of metal, thus trapping and accumulating them at the interface (Figure 4.13a). Although this may contribute to the inability for the Na metal to re-wet the NBA surface as previously shown, based on the magnitude of the hysteresis, it is unlikely that this is the sole reason for the lack of re-wetting. Given the differences in processing of the Li and Na metal foils in this work compared to Chapter 4.1, it is expected that the Na foils have significantly higher levels of impurities which may explain this increase. As will be discussed in Chapter 4.2.3.4, it is expected that this particular mechanism would result in a linear increase in resistance, suggesting that the effects of impurity trapping can be subtracted. The resulting potential response subtracting out a linearly increasing baseline is shown in Figure 4.13d. In this potential response, it can be seen that there is a slight, yet reversible, response to the cycling pressure, where the potential increases at low stack pressures, but will decrease to its approximate original value when the stack pressure is increased again. This is consistent with what was observed in the Li/LLZO system. These reversible changes in the cell resistance at high stack pressures was originally believed to suggest the presence of a pressure-dependent kinetic phenomenon at the interface, but was also recently hypothesized by Zhang *et al.*[99] to be related to the accumulation of miniscule changes in electrode/electrolyte contact area caused by the flow of the metal into and out of surface asperities.

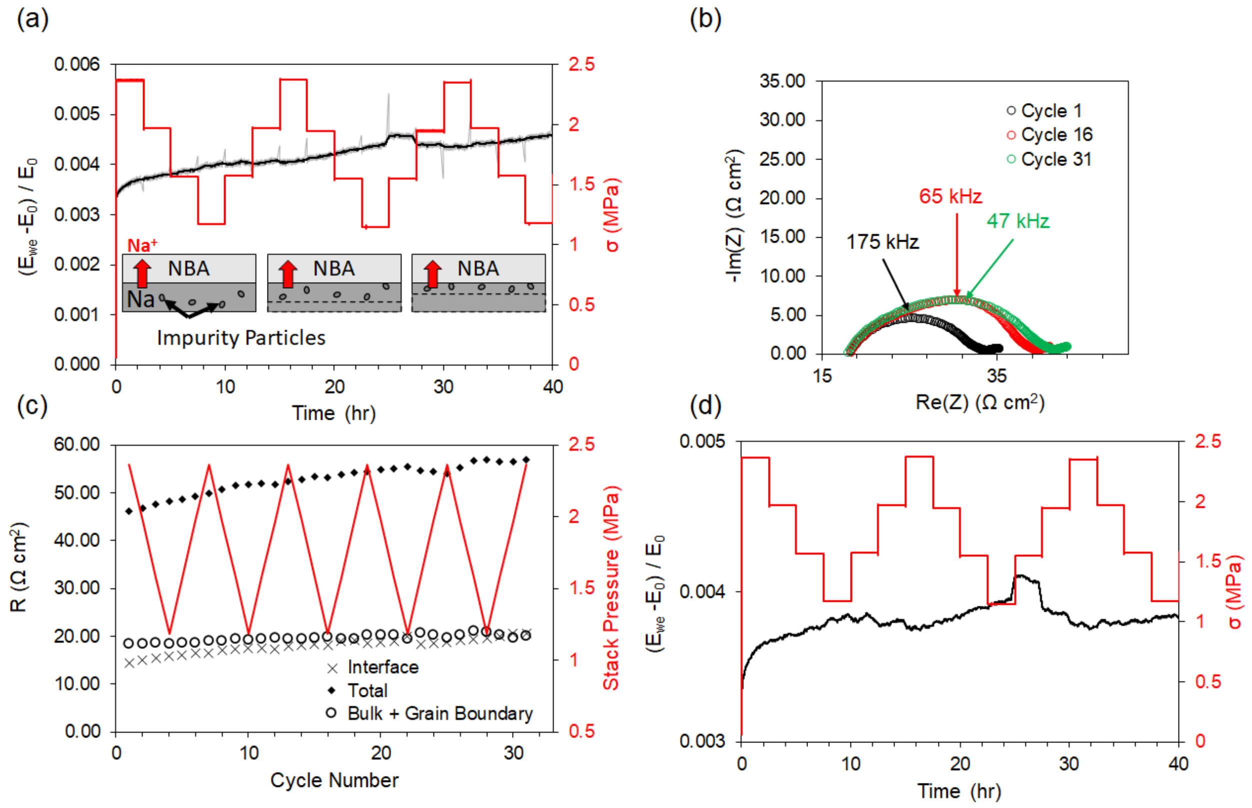

Figure 4.13: The potential behavior at high stack pressures. a) The potential response while cycling the stack pressure at high values under a constant current density of 0.1 mA cm^{-2}. A curve smoothed using a 100-point moving average is shown in black while the original data is shown in grey. b) The impedance spectra measured *in operando* at the end of the first, sixteenth, and thirty-first pressure step in (a). c) The values of the individual components of the cell resistance measured at each pressure step in (a). d) The resulting potential response from (a) with a linear baseline subtracted out.

4.2.3.4 Identifying interface morphology at the anode/electrolyte interface under stripping currents

From a practical perspective, significant changes in the cell resistance and contact area will lead to equally significant shortening of the lifetime of the cell. For this reason, defining a "critical stack pressure" provides a useful metric for designing and operating solid-state batteries such that void formation can be mitigated. However, as voids continue to grow and the anode/electrolyte contact area decreases, the true stress on the remaining metal anode also increases, thus improving the likelihood of closing those voids. Therefore, the balance between electrode creep and stripping is constantly changing, resulting in a variety of features that appear in the potential response. This also makes it extremely difficult to clearly define an absolute "critical stack pressure". However, a better understanding of how the contact area changes in response to applied current and stack pressure can provide methods for better diagnosis and analysis of battery failure.

It was estimated in Chapter 4.1.3.4 from a simple comparison between the creep flux and current flux that their magnitudes are similar enough to justify the existence of pressure-dependent void formation, however, the flux balance alone does not describe the evolution of the interface nor the corresponding potential response. As shown in Figure 4.14a, a number of different features in the potential response can be identified which may suggest different changes in the morphological evolution of the interface. These features may be better understood by modeling the evolution of interface voids. In the simplest case, contact loss at the electrode/electrolyte interface can be modeled by the growth of hemispherical voids as depicted in Figure 4.14b. Although these voids are unlikely to be spherical in reality, more in-depth knowledge about the shape of the voids, including the contact angle as a function of the radius, would be necessary. While the contact angle would typically be the wetting angle, which is solely a function of surface chemistry, an externally applied stack pressure should flatten these voids such that the contact area also becomes dependent on extrinsic factors such as pore size.

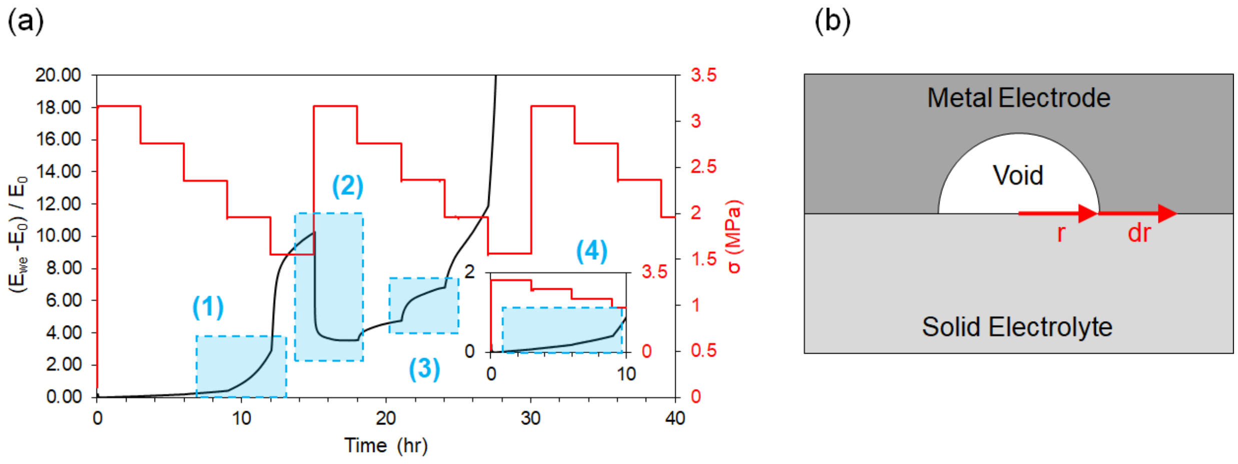

Figure 4.14: A basic model for understanding different features in the potential response to changing stack pressure. a) Potential response to changing stack pressures of Na/NBA at 0.4 mA cm^{-2}, reproduced from Figure 4.12, highlighting key features in the potential response. b) Schematic of void with radius r at the electrode/electrolyte interface

The driving force for void growth or shrinkage is a non-zero net flux of either incoming or outgoing metal. This can be expressed by the equation:

$$\frac{dV}{dt} = 2\pi r^2 \frac{dr}{dt} = \bar{V}\Delta J \tag{4.5}$$

Where V is the volume of the void, t is the time, r is the radius of the void, and ΔJ is the net flux of metal into or out of the void. The quantity $\bar{V}$ is a characteristic volume of material that is transported by the flux. This volume is dependent on the geometry of the void and the physical properties of the metal electrode. In this section, each of the four different features shown in Figure 4.14a will be described by this basic model, which describes the of growth of N equally fast-growing voids. It is assumed that interfacial kinetics are uniform and constant and therefore changes in electrode/electrolyte area are solely responsible for changes in cell potential. Therefore, the potential is proportional to the contact area:

$$E(t) \sim \frac{1}{A(t)} \tag{4.6}$$

where E is the cell potential and A is the contact area.

The first feature (1) is a convex potential response. This type of potential response is unstable in nature and therefore is likely to be dominated by the stripping of metal due to the applied current. The stripping of the metal therefore grows the size of the voids in an unstable manner (neglecting the effects of stack pressure). Therefore, the flux is driven by the applied current and the characteristic volume is associated with the physical properties of the metal electrode as shown in the equation:

$$\frac{dV}{dt} = \frac{jM}{\rho F} = \frac{IM}{\rho F(A_0 - N\pi r^2)} \tag{4.7}$$

Similarly, this can be rewritten as a differential equation and analytically solved, resulting in the following relation:

$$\frac{2\pi r^3}{3}A_0 - \frac{2N\pi^2 r^5}{5} = \frac{IM}{\rho F}t + C(r_0) \tag{4.8}$$

where A_0 is the initial area, I is the applied current, M is the molar mass, ρ is the density, F is Faraday's constant, and C is a constant dependent on the initial radius.

The second feature (2) is a concave potential response. This type of potential response was described by Zhang *et al.*[99] and shown to be dominated by creep of the metal electrode. In this case, it is assumed that the flux is dominated by power-law creep of the alkali metal. In addition, the volume change is given by the strain-rate multiplied by the characteristic volume, which is related to the void volume in this case. This is described by the equation:

$$\frac{dV}{dt} = \bar{V}\dot{\varepsilon} = 2\pi r^3 \dot{\varepsilon} = 2\pi r^3 K\sigma^m \tag{4.9}$$

Given that the stress is also dependent on the void area, the equation can be rewritten as the following differential equation:

$$\frac{(A_0 - N\pi r^2)^m}{r} dr = KP^m dt \tag{4.10}$$

where P is the applied force, K is a coefficient, σ is the true stress, and m is the stress exponent. Zhang *et al.*[99] recently developed a model for understanding the change in contact area due to this phenomenon using a rigorous contact mechanics-based approach. Their results show similar concave features that were used to closely match the data presented in Figure 4.4.

The third feature (3) depicts a transition from convexity to concavity, which suggests that initially the behavior is dominated by void growth by the applied current, but as the contact shrinks, the applied stress also increases and thus begins to suppress the continued growth of the voids. Once the two forces are balanced, a steady-state plateau is reached. This can be described by a combination of Equations 4.8 and 4.10.

The fourth feature (4) is a pressure-independent linear increase in the potential caused by impurity trapping as discussed in Chapter 4.2.3.3. In this case, the impedance growth is not attributed to the volumetric change in the interface voids, but rather the reduction of area due to non-conductive impurities. As previous discussed, the impurities found within the electrode bulk are pushed and trapped at the interface, forming a passivating layer, as described by Maslyn *et al.*[25]. The chance of encountering an impurity at a given time can be expressed as a probability density function related to the impurity concentration in the metal and the applied current:

$$P = P(I, c_i), \qquad 0 \leq P \leq 1 \tag{4.11}$$

Therefore, the decrease in area due to interface passivation is simply given by the equation:

$$A(t) = A_0 - \pi \overline{r_i}^2 \int P(I, c_i) dt \tag{4.12}$$

where $\overline{r_i}$ is the average impurity particle radius. Given that the concentration of impurities is low (significantly lower than the concentration of bulk metal), this would result in a gradual linear-like increase in the cell potential.

For each of these four scenarios, the resulting areas normalized by the original area ($A_n = A/A_0$) is plotted in Figure 4.15. The resulting analytical plots exhibit features resembling that of the experimentally observed potential changes. The resemblance between the analytical results and the experimental observations show that the basic models can be used to correlate physical phenomena with identification of these features in the experimental potential response of the solid-state battery. The models presented here are only a rudimentary description of the hypothesized phenomena. In order to completely match the data, a rigorous model that takes into account contact mechanics, realistic void geometries, frictional effects, metal elasticity, current focusing effects, void nucleation tendencies, and other intricacies would be necessary. However, development of such a model goes outside the scope of this work.

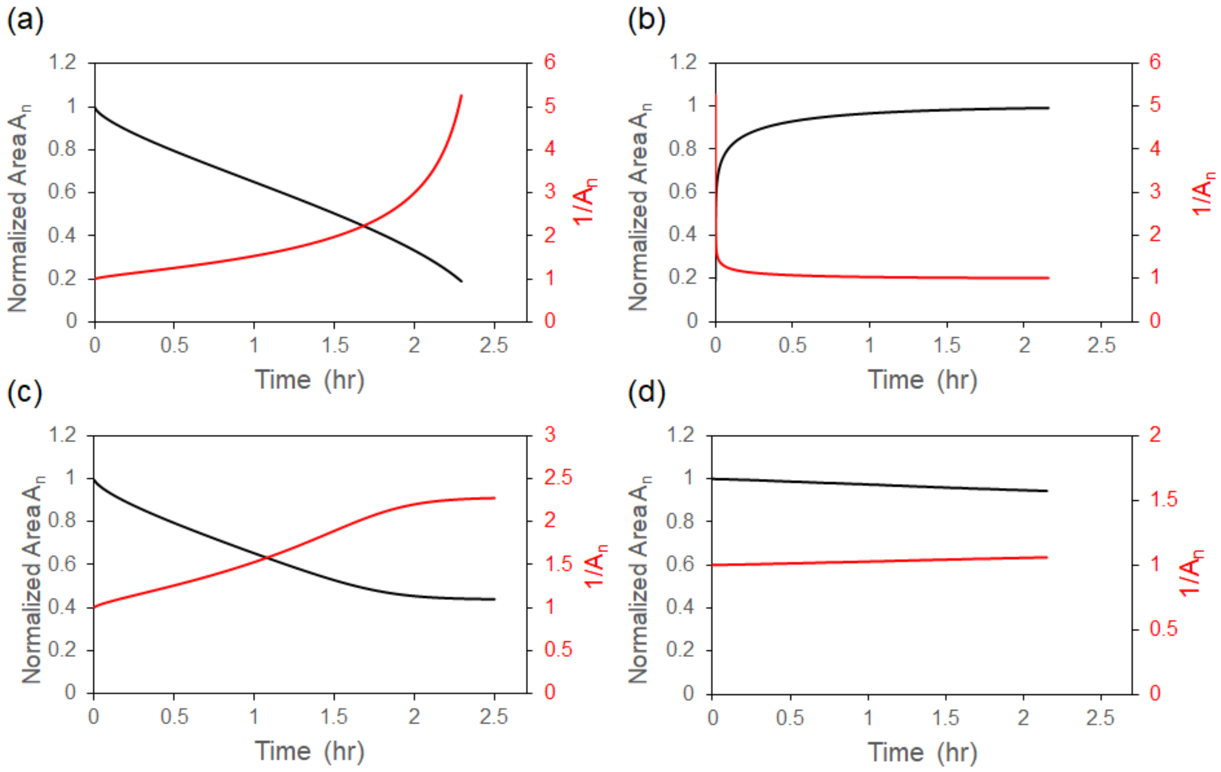

Figure 4.15: Examples of the predicted changes in area associated with Na metal stripping and its reciprocal for each of the features identified in Figure 4.12, corresponding to the following phenomena: a) current dominated void growth, b) creep dominated void closure, c) current and creep balancing, and d) impurity trapping

4.2.3.5 Implications for analyzing solid-state batteries

The demonstration that contact area between the electrode and electrolyte can decrease under higher stripping currents has major implications for the performance of solid-state batteries. These implications were discussed in Chapter 4.1.3.4 as well as by other recent works in the literature[30,31,62,63]. The primary implication is that the growth of voids can induce current focusing effects upon electroplating, which can prematurely short-circuit the cell and significantly shorten the lifespan of the battery. Additionally, the growth of the cell resistance increases the Ohmic losses which will lead to decreases in accessible battery capacity within safe voltage limits. It has been hypothesized that these limitations caused by void formation are dominated by the mechanical properties of the alkali metal electrode, and this work clearly demonstrates this to be the case. In the case of the Na metal electrode, due to the higher compliance compared to Li metal, it is easier to suppress the growth of voids under similar stack pressures. However, aside from the quantitative relationship between stack pressure and cell resistance between the two systems, both systems qualitatively show near identical potential responses to changing stack pressure, suggesting the phenomenon occurs regardless of cell chemistry. From this knowledge, several implications are present that may guide the design of solid-state batteries.

First, it is clearly demonstrated that the lower flow stress metal requires less stack pressure and/or can withstand higher current densities without increases in cell resistance. This suggests that the rate capabilities of the battery will be highly dependent on the mechanical properties of the metal anode. Therefore, there will exist a further trade-off between energy density and power density, where Li metal systems can provide higher energy densities but will be more limited in terms of power compared to Na metal. Additionally, while metallurgical approaches have been taken in the literature[100] to improve chemical stability of the electrode/electrolyte interface or to improve the safety of the metal anode, these approaches will also affect the rate capabilities of the system. In most cases, it is common for the addition of alloying elements to a pure metal to strengthen the metal, which in this case has detrimental effects to the rate capabilities and requires higher stack pressures to maintain contact.

Secondly, as previously suggested, because this phenomenon is independent of cell chemistry, this allows for a widely applicable method of battery diagnosis. As discussed, there exist signature features in the potential response as a function of stack pressure that can indicate how the interface morphology is evolving. Although the conditions at which these features appear will be dependent on cell operation and cell chemistry, the qualitative description of the features is independent. This means that identification of these features in the potential behavior as the cell is operated can possibly be used as a diagnostic tool for early detection of cell failure as well as post-mortem analysis.

Lastly, avoidance of significant void growth and/or early detection of void growth will be crucial for maintaining long lifetimes of solid-state batteries. As demonstrated in Chapter 4.2.3.2, there exists a significant hysteresis upon re-wetting the Na metal onto the NBA surface. It was shown that even after re-applying a high stack pressure, the Na metal does not completely re-wet the NBA surface. In the case of Li metal, where high temperatures are typically used to initially wet the electrode onto the electrolyte, this effect is only expected to be worse. Therefore, once a significant void is formed, removal of the void from the interface is not necessarily simple and will require additional methods, either by applying higher temperatures to facilitate faster creep or by electrochemically filling in the voids at low currents. In a real scenario, this would effectively kill the battery if a void forms and is not removed before the next usage.

4.2.4 Conclusions

Significant attention in recent years has focused on studying the electrodeposition process in solid-state batteries due to the widely known rate limitations caused by metal filament penetration. However, equally important phenomena upon metal stripping has also emerged as an equally important rate-limiting factor in the cycling of solid-state batteries. It was demonstrated that with Li metal electrodes, significant increases in cell potential caused by changes in the electrode/electrolyte contact area is related to the deformation of the Li metal via an applied stack pressure. In this work, it was demonstrated that the same behavior is observed in a Na based system, utilizing Na metal and the NBA electrolyte. While similar qualitative behavior was exhibited, showing dramatic increases in cell resistance at low stack pressures and/or high current densities, it was shown that the Na/NBA system could withstand higher current densities and lower stack pressures compared to Li metal when paired with a similar ceramic electrolyte. This is due to the higher mechanical compliance of Na metal compared to Li metal, allowing for easier suppression of void growth. While it was hypothesized that the Na metal should more easily re-wet the NBA surface upon reapplication of high stack pressures, it was demonstrated that this is not necessarily the case. However, it was shown that similar to the Li/LLZO system, small changes in the cell resistance are reversible at high stack pressures. Finally, by investigating key features in the potential response to changing stack pressure that can be seen in both the Li and Na systems, a simple model is proposed for describing the morphological evolution of voids at the electrode/electrolyte interface. Overall, the results presented in this work demonstrate a clear relationship between the electrochemical performance of a solid-state battery and the mechanical properties of the alkali metal electrode, motivating a further understanding for mechanics at this interface and providing further insight into the interface evolution.

Chapter 5 Li Electrodeposition at a Solid-Solid Interface

Until now, all of the topics discussed have revolved around the Li/LLZO and the Na/NBA interface. When considering electrodeposition onto the alkali metal, these electrodes are non-blocking to the ionic species. Therefore, under stable conditions, after an atom is deposited onto the metal electrode, it becomes a part of the bulk and can diffuse into the bulk or deform along with the surrounding material. In the case where the plated metal cannot diffuse into the bulk, as with a blocking electrode, it is still relatively unclear how the morphology of the interface would evolve as the plated metal is interposed between the electrode and the electrolyte. Presumably, deformation of the electrode would be necessary to accommodate the interposition of the plated metal, but once the metal has been plated, both the physical and chemical potential landscape of the interface has been changed. Understanding the behavior of this particular case would not only provide insight into the nucleation behavior of electrodeposited metals out of solid-electrolytes but may also provide new perspectives on the mechanisms for unstable metal penetration through ceramic electrolytes. Even beyond just fundamental understandings, demonstration of this one particular system has major implications in terms of high energy density battery architectures. If Li or Na metal could be electrodeposited through a solid-electrolyte onto a blocking electrode, such as a current collector, this would effectively enable the usage of an "anode-free" battery architecture.

As discussed in Chapter 1.3.2, one of the benefits of using alkali metal anodes over an intercalation anode, is the lack of excess mass associated with a host structure. However, given that conventional Li-ion cathode materials are lithiated, any pre-deposited Li in the battery is acting as excess mass and volume which will lower the energy density. Therefore, in order to achieve the maximum theoretical energy density of alkali metal solid-state batteries, an "anode-free" architecture is necessary. In this case, the alkali metal anode is formed upon the first charge cycle by electroplating the Li or Na contained within the cathode onto the current collector, such that no excess metal is used. However, in order for this to be feasible, stable electroplating onto the current collector needs to be demonstrated.

This chapter investigates the feasibility of alkali metal electroplating at the interface of a current collector and solid-electrolyte. Owing to the ability to adhere conventional Li-ion battery current collectors onto an LLZO surface and taking advantage of the maturity of Li-ion cathode materials, this chapter explores the nucleation behavior and morphological evolution of Li metal onto a blocking electrode and demonstrates the first "Li-free" all-solid-state battery with the LLZO electrolyte.

The following chapter sections are published in modified forms as:

I. Michael J. Wang, Eric Carmona, Arushi Gupta, Paul Albertus, & Jeff Sakamoto. Enabling "Li-free" Manufacturing of Pure Li Metal Solid-State Batteries Through *in situ* Plating. *Nat. Commun., accepted*, (2020).

5.1 Enabling "Li-free" Manufacturing of Pure Li Metal Solid-State Batteries Through *in situ* Plating

5.1.1 Introduction

Owing to the combination of high energy density and safety, solid-state batteries are a promising candidate to enable the widespread adoption of EVs. Along with the replacement of the flammable liquid electrolyte, solid-electrolytes may enable the replacement of graphite anodes with metallic Li, which allows for a dramatic (40-50%) increase in energy density[6,38,39,64,101]. Although advanced cathode chemistries would undoubtedly further improve the theoretical energy densities, it is believed that state-of-the-art cathodes (e.g.: NMC, NCA, LFP) are currently the most viable chemistries to achieve energy densities >1000 Wh L^{-1}, cycle life > 1000 cycles with $\leq$ 80% capacity fade, and current cost < \$100/kWh targets[102,103]. However, given that current state-of-the-art cathodes are typically manufactured in the fully lithiated state, any pre-deposited Li metal will add extraneous volume.

On the laboratory scale, Li metal solid-state cells are commonly constructed using thick (>200 μm) Li foils, although Li foils down to ~20 μm have been made. However, given the difficulty and cost of handling, free-standing Li foils may not be viable[104]. In addition to manufacturing, integration of the Li metal anode with a solid-electrolyte with relevant thickness, low interfacial resistance, high chemical purity, and using scalable processes still remains a major challenge. For these reasons, in both liquid and solid-state Li metal batteries, there is a growing interest in “Li-free” (or anode-free) manufacturing[105–108], in which the battery is fabricated in the discharged state, with a bare current collector replacing the conventional anode. The Li metal anode is then formed electrochemically on the first charge cycle by electroplating using Li contained within the cathode. In liquid based batteries, this concept has been demonstrated, but it’s feasibility is limited by the high reactivity of Li with traditional liquid electrolytes, leading to low cycling efficiency[105,106,108–110].

Lithium phosphorus oxynitride (LiPON) is one of the few stable solid electrolyte materials that demonstrate the ability to resist Li filament propagation, thereby enabling the fabrication of “Li-free” batteries[111]. Indeed, the pioneering development of thin film LiPON technology demonstrated the feasibility of Li metal solid-state secondary batteries, however, current approaches are pursuing bulk-scale manufacturing approaches to achieve cost parity with large format technologies such as Li-ion. One of the most promising solid-state electrolytes is $Li_7La_3Zr_2O_{12}$ (LLZO), which has high ionic conductivity and excellent stability against Li metal. However, unlike most LiPON systems, under certain conditions LLZO is susceptible to Li filament propagation and subsequent short-circuiting[29,35,36]. Recent studies have investigated the Li nucleation behavior at the interface of sputtered current collectors and LiPON or LLZO electrolytes, which allows for visualization of the plating process[17,18,112,113]. It was commonly observed that Li plating causes fracture of the current collector, leading to "dead Li" formation, low Coulombic efficiencies, and even short-circuiting in the case of LLZO. Thus, although "Li-free" manufacturing has been demonstrated in solid-state systems, the inability to plate significant capacities of Li without either electrolyte or current collector fracture severely limits the cycle life of the cell. These issues combined with the limited approaches for large scale LiPON manufacturing have prevented widespread adoption of "Li-free" solid-state batteries. In addition, it has been hypothesized that the interposition of a Ag-C (~10 µm) layer can reduce nucleation energy to enable Li metal plating using Li from an NMC cathode. While reduction in nucleation energy was not quantified, Li plating into and beneath the Ag-C interlayer was clearly demonstrated[114]. However, in principle, so long as physical and electrical contact can be maintained throughout the formation process and subsequent battery operation, the combination of "Li-free" architectures and a stable solid electrolyte is a rational strategy toward practical manufacturing of high-efficiency Li metal secondary batteries. Given the myriad of complex physical phenomena at play, a deeper understanding of the mechanics and electrochemistry is necessary to assess the feasibility of "Li-free" manufacturing of solid-state batteries.

This work investigates the potential for “Li-free” solid-state batteries using LLZO electrolytes. It is demonstrated that commercially-relevant capacities ($\geq$3 mAh cm^{-2}) of Li metal, comparable to current state-of-the-art Li-ion electrodes, can be both plated and stripped from an LLZO/current-collector. Based on the electrochemical results and plating behavior of the Li metal, a simple model involving interfacial forces is proposed for coupling the mechanics at the interface with the electrochemical nucleation behavior. Moreover, the work of adhesion between the current collector and the LLZO is measured to enable correlation between overpotential and nucleation energy. This mechanistic insight enables the demonstration of the holy grail anode; pure, *in situ* formed Li without reliance on interlayers. Finally, the performance of electrodeposited Li as a Li metal anode is evaluated in a symmetric cell as well as when coupled with a state-of-the-art cathode material. The results presented motivate further understanding of material interactions at solid-solid interfaces but also demonstrate the feasibility of manufacturing “Li-free” all-solid-state batteries.

5.1.2 Methods

5.1.2.1 Cell assembly

In this study, CC/LLZO/Li cells were fabricated using commercial metal foils, hot-pressed LLZO pellets, and Li foil. Li metal foil was used as the Li source primarily because it has been demonstrated in several other works that Li/LLZO interfaces can be reliably and consistently fabricated with low interfacial resistances without any intermediate coatings or modifications[33,62,89,115]. In comparison, there have not yet been many demonstrations of facile charge transport across cathode/LLZO interfaces which may induce artifacts in the nucleation behavior at the CC/LLZO interface. LLZO pellets of the composition $Li_{6.5}La_3Zr_{1.5}Ta_{0.5}O_{12}$ were synthesized by a solid-state synthesis method and then consolidated by rapid-induction hot-pressing as described by Taylor *et al.* and cut into pellets ~2 mm thick on a diamond saw[42]. Battery grade Ni (35 μm) and Cu (10 μm) foils were purchased from Targray and used as current collectors. In order to attach the current collectors to the LLZO surface, one side of the LLZO was polished with 1200 grit sandpaper and then the current collector was placed onto that surface. The current collector was then laminated to the LLZO by applying a pressure of 3-6 MPa at temperatures between 900-1100°C, depending on the current collector metal, for 5 min. After laminating, the opposite LLZO face was then polished using a variety of sandpapers and diamond pastes to a final polish of 0.1 μm. As previously described, the CC/LLZO was then heat-treated at 400°C in Ar to remove resistive surface layers and then 750 μm Li foil (Alfa Aesar) was pressed onto the polished surface at elevated temperatures[18].

Full cells were fabricated by first laminating a Cu current collector (10 μm) to the LLZO pellet and heat-treating at 700°C in Ar. A composite cathode was composed of a polyethylene oxide/lithium bis(triflouromethanesulfonyl)imide (PEO-LiTFSI) catholyte and a commercially cast state-of-the-art NCA electrode for conventional Li-ion batteries (University of Michigan Battery Lab). The NCA electrode was cast with an active loading of ~3 mAh cm^{-2} and an approximate porosity of 35%. The PEO-LiTFSI catholyte was synthesized as described by Gupta *et al*.[30] and then infiltrated into the cathode porosity by heating the PEO and uniaxially pressing into the cathode against the heat-treated LLZO surface under a pressure of 4.2 MPa and held for several hours at a temperature of 80°C.

5.1.2.2 Electrochemical methods

Electrochemical experiments were performed using a Bio-logic VMP-300 galvanostat/potentiostat. After fabricating the CC/LLZO/Li cells, Li was plated onto the current collector by applying a constant current such that Li^+ was transported from the Li metal source toward the current collector. Low current densities in the range of 0.05-0.1 mA cm^{-2} were used for in situ plating under a stack pressure of ~4 MPa. A temperature of 25°C is used for all cycling tests. Electrochemical impedance spectroscopy (EIS) was used to monitor the state-of-health of the cell and to confirm the presence of Li metal at the CC/LLZO interface. EIS was conducted using a 5 mV perturbation voltage at frequencies between 500 mHz and 7 MHz. Li stripping experiments were performed by applying a constant current density in the range of 0.05-0.3 mA cm^{-2} with the opposite polarity, such that Li^{+} was transported away from the CC/LLZO interface toward the Li foil source.

After assembly of the Cu/LLZO/PEO-NCA full cells, the Li metal anode was formed by plating the Li from the NCA onto the Cu at a constant 0.05 mA cm^{-2} at 80°C. After formation of the Li metal anode, the cells were cycled at 60°C with a constant current, constant voltage (CCCV) scheme at a C/10 rate (0.27 mA cm^{-2}) between 4.2 V and 3.0 V, with a 1 hr constant voltage hold at 4.2 V. EIS was performed after every tenth charge cycle with a 5 mV perturbation voltage between 500 mHz and 7 MHz.

5.1.2.3 Materials characterization

In order to visualize CC/LLZO interfaces, cross-sections were cut using focused ion beam (FIB) milling, imaged, and analyzed under EDS using a Thermo Fisher Helios G4 Plasma FIB UXe. Surface analysis was done using a Hitachi S3500N scanning electron microscope. Just prior to evacuation of the SEM chamber, the current collector was peeled off the LLZO surface to reveal the plated Li. Although there is some exposure to air, the removal of the current collector was done as quickly as possible to minimize the exposure.

To measure the work of adhesion of the laminated current collectors on the LLZO surface, peel tests were conducted using a TA.XTplus Textra Analyzer with a 90° Degree Peel

Rig. Peel tests were conducted based on a modified version of the ASTM D6862 - 11(2016) method[7]. Ni and Cu foils cut to a width of 4 mm and length of 12 mm were laminated onto the LLZO under the conditions described in Section 5.1.2.1. Peel tests were conducted at a rate of 10 mm min^{-1} until complete delamination of the current collector. The work of adhesion could be estimated based on the following equation[116–119]:

$$\Gamma = P(1 - cos\varphi) - Q \tag{5.1}$$

Where P is the average peel force per width, φ is the peel angle, Q is the work required to deform the current collector, and Γ is the work of adhesion. The peel force is measured from the steady state regime, after the initial transient region and before fracture of the interface. Although a 90° peel rig was used, the actual peel angles were measured to be 45° for the Ni current collectors and 81° for the Cu current collectors. While an exact value for Q is difficult to obtain due to its dependence on several variables, based on ideal models[117–119], its value can be estimated by the following relationship:

$$Q = \frac{\sigma_Y^2 t}{2E}\left(2\sqrt{\frac{6EP}{\sigma_Y^2 t}(1-\cos(\varphi'))} - 5 + \frac{10}{3\sqrt{\frac{6EP}{\sigma_Y^2 t}(1-\cos(\varphi'))}}\right) \tag{5.2}$$

Where σ_Y, t, and E are the yield strength, thickness, and elastic modulus of the current collector, and ϕ’ is the effective peel angle accounting for curvature near the interface. In this case it is assumed that the effective peel angle and the measured peel angle are identical. It should be noted that due to the ideality of the model along with other forces that may exist at the CC/LLZO interface, the estimated work of adhesions represents an upper bound of the true values.

5.1.3 Results & Discussion

5.1.3.1 Demonstration of in situ plating of Li

Figure 5.1 shows the typical electrochemical response of a “Li-free” cell from open circuit voltage (OCV) through electrodeposition. The OCV begins at ~1.8 V and then upon application of a constant current density of 0.05 mA cm^{-2}, the potential quickly drops to 0 V followed by a negative potential, which indicates the onset of sustained electrodeposition of Li. After the initial drop in potential below 0V, the potential reaches a minimum value of ~25 mV within the first few minutes (~3 μAh cm^{-2}) of plating before asymptotically approaching a fixed steady-state value of ~20 mV within the first hour of deposition; Motoyama *et al.*[112] and Krauskopf *et al.*[18] also observed the potential passing through a minimum. It has been hypothesized that this behavior is representative of the overpotential required to nucleate Li onto the current collector (CC)[18,112]. Based on the electrochemical impedance spectroscopy (EIS) analysis shown in Figure 5.1c, the total ionic impedance of the cell is ~350 **Ω** cm^2, which corresponds to a total DC polarization of ~17.5 mV at a 0.05 mA cm^{-2} current density, which is reasonably consistent with the steady-state plating potential. Hence, both the galvanostatic results and the EIS spectra indicate a resistance dominated by that of the LLZO pellet after the onset of nucleation. However, as seen in Figure 5.1b, the magnitude of the nucleation overpotential is significantly (~10x) smaller than the values reported by Motoyama *et al.*[112] and Krauskopf *et al.*[18], which is discussed in later sections. It was also suggested by Lee *et al.*[114] that the reduction in nucleation overpotential caused by a Ag-C interlayer enabled stable deposition of Li onto a current collector, however, the nucleation and electrochemical behavior in alloying interlayers is not well understood. After overcoming the nucleation overpotential, the potential is relatively constant for the duration of the ~100 h of plating. It is demonstrated in

Figure 5.1b that ~5 mAh cm^{-2} of Li, corresponding to ~25 μm of plated Li (assuming uniform deposition), can be plated without changes in the potential response. Identical tests were performed on current collectors of different metals with similar results, demonstrating this capability regardless of interface chemistry. To further study the stability and kinetics of the Li/LLZO interface during *in situ* plating, EIS was periodically performed as Li was plated and is also shown in Figure 5.1c. Initially, before any Li has been plated, the impedance spectrum exhibits capacitive behavior at low frequencies (<10 Hz) due to the blocking nature of the Ni current collector to Li^+. After Li deposition, the low frequency regime is dominated by charge-transfer, due to the non-blocking nature of Li. This is indicated by the semi-circular feature at low frequencies (0.5-5 Hz). Based on the diameter of the semi-circle, the interfacial resistance of the electrodeposited Li against the LLZO surface is <10 Ω cm^2, which is in good agreement with previous results in which a conventional Li anode was used (e.g. foil)[29,33,89]. Furthermore, it can be seen that after the Li is initially electrodeposited, there is no change in the impedance spectra after 5 mAh cm^{-2} of Li has been plated. This confirms that no Li filaments have nucleated in the LLZO. The value of 5 mAh cm^{-2} was chosen as a relevant amount of Li commensurate with the expected areal loading of advanced cathodes. However, based on these results it is likely that significantly more Li can be plated without degradation of the LLZO at these current densities. Identical electrodeposition experiments were conducted at increasingly high current densities, but it was found that short-circuiting from Li filament propagation was consistently observed at current densities of 0.09 mA cm^{-2} and above. It is interesting to note that this value is approximately 10x lower than reported values of the critical current density in symmetric Li/LLZO/Li cells[29]. This may support recent hypotheses which suggest that the combination of inhomogeneous Li plating and slow diffusivity and deformation of electroplated Li can result in regions of high pressure and act as nucleation sites for Li filaments[18,23,29,37].

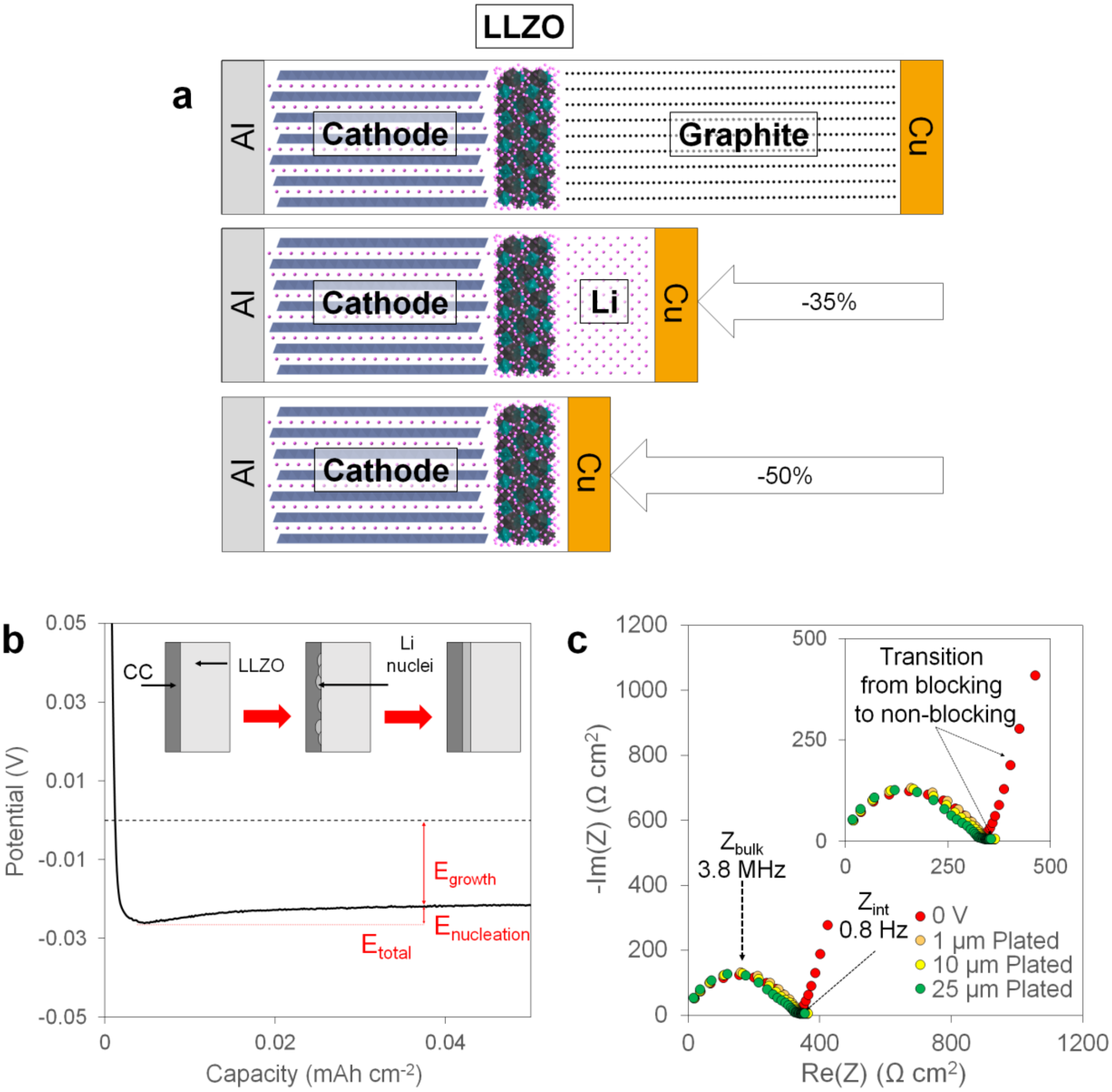

Figure 5.1: Schematic of a “Li-free” cell configuration and analysis of electrodeposition of Li onto a current collector at a constant current of 0.05 mA cm^{-2} at 25°C. (a) Schematic of a discharged “Li-free” configuration in comparison to state-of-the-art Li-ion and a solid-state Li metal battery with pre-deposited Li metal. Here, the current collector material is assumed to be Cu. (b) The potential response upon the initial application of a constant cathodic current, plating Li metal onto a Ni current collector. (c) The impedance spectra at several points upon the Li plating process.

It is demonstrated in Figure 5.2 that not only is it possible to electrodeposit Li at the solid-solid interface, but it is also reversible. This aspect is vital since the extent of reversibility is directly linked with the need for excess Li capacity from the cathode, if any. Similar to the potential response upon electrodeposition, a relatively constant potential is maintained upon steady-state Li stripping with the magnitude of the potential matching that upon Li plating. As the electrodeposited Li is nearly depleted, the potential dramatically increases, which is a combination of the increase in resistance associated with contact loss and the change in the OCV when transforming from a symmetric Li/Li cell back to a Li/Ni cell. Based on the amount of Li that was originally plated, it is shown that ~99% of the Li can be returned to the source, which includes a 2 hr constant voltage hold at 1.8 V. Figure 5.2b shows the Coulombic efficiency of Li stripping as a function of cycle number. Each cycle, the Li is plated at 0.05 mA cm^{-2}, while the Li is stripped first at 0.05 mA cm^{-2} for three cycles, then at 0.1 mA cm^{-2}, 0.2 mA cm^{-2}, and 0.3 mA cm^{-2}, each for three cycles. It can be seen that the efficiency is relatively stable above 99% over the 12 cycles. Unlike in liquid electrolytes where the loss in Coulombic efficiency is due to passivation and formation of “dead Li”, the 1% irretrievable Li observed in these experiments is more likely due to contact loss with either the LLZO or the current collector. The impedance spectra before and after Li plating and stripping are shown in Figure 5.2c. As demonstrated in Figure 5.1, initially, the low frequency regime (representing the Li-LLZO impedance: $Z_{\text{Li-LLZO}}$) undergoes a transition from blocking to non-blocking behavior after the onset of Li electrodeposition. After stripping of the electrodeposited Li, the $Z_{\text{Li-LLZO}}$ instead transitions from a non-blocking behavior to blocking behavior. Furthermore, the high frequency portion of the spectra (representing the LLZO ohmic impedance: Z_{LLZO}) significantly increases, which can be attributed to the expected high degree of contact loss that occurs after removal of the interposed

Li. After Li is re-plated on the subsequent cycle, not only does the low frequency behavior return to non-blocking behavior, but the Z_{LLZO} also decreases and returns to its original value and shape. This is due to the electrodeposition of new Li which fills the gap left by the electroplated Li from the previous cycle, therefore restoring the original contact and contact area between LLZO, current collector, and Li.

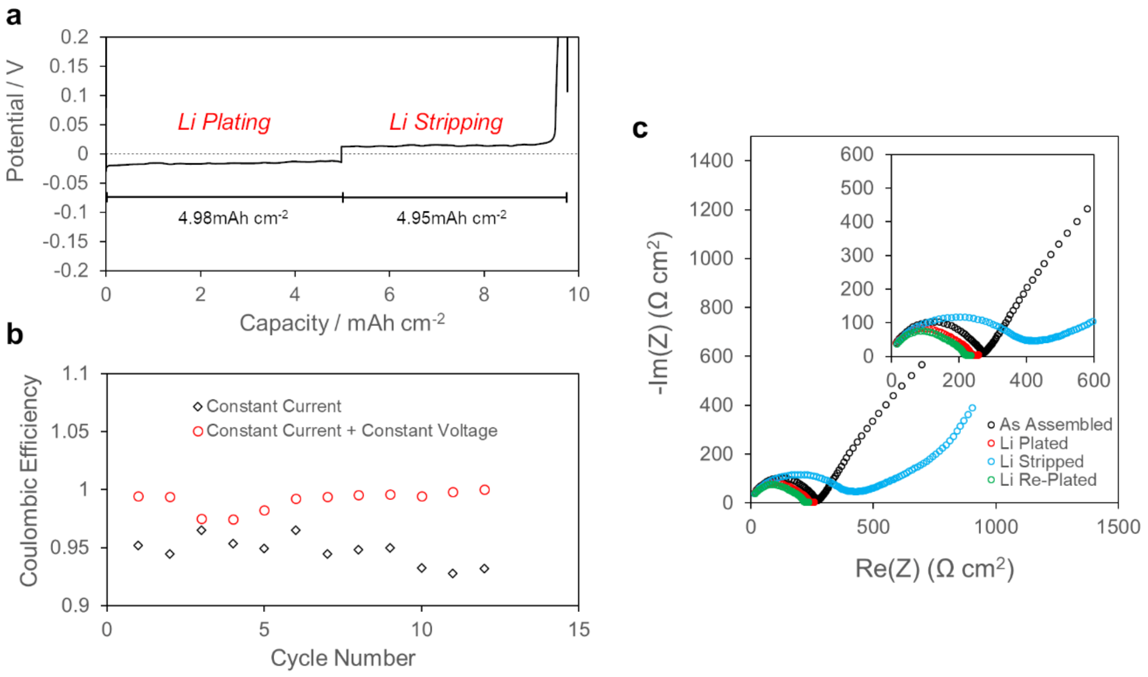

Figure 5.2: Electrochemical behavior upon Li plating and stripping at 25°C. (a) Potential response upon plating 5 mAh cm^{-2} of Li onto a Cu current collector at 0.05 mA cm^{-2} and then subsequently stripping at 0.05 mA cm^{-2}. (b) The Coulombic efficiency of Li plating and stripping of 3 mAh cm^{-2} of Li as a function of cycle number. The potential profiles are shown in Figure 5.3. (c) A comparison of the impedance spectra before and after the first Li plating and stripping cycle.

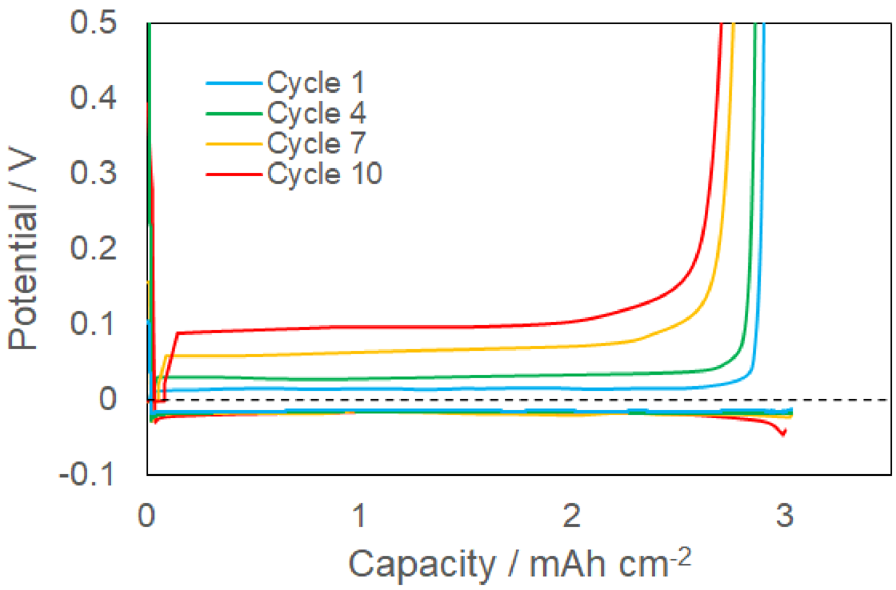

Figure 5.3: Potential profiles over several plating and stripping cycles at different current densities corresponding to the data plotted in Figure 5.2b.

5.1.3.2 Mechanics and nucleation of Li at the CC/LLZO interface

Figure 5.4 shows cross-sectional SEM images of the cell assembly. The pristine cell (Figure 4a) shows minimal gaps between the Cu current collector and LLZO, which is replaced by the plated Li in Figure 5.4b. Figure 5.4b depicts the interface after 5 mAh cm^{-2} of Li has been plated, which shows the appearance of an intermediate phase which can be identified as elemental Li since it is unidentifiable under EDS. Assuming uniform Li deposition, 5 mAh cm^{-2} would correspond to ~25 μm of plated Li, but the observed layer is 33 μm, suggesting some non-uniformity in the Li deposition. Finally, after stripping of the 5 mAh cm^{-2} of Li, the intermediate phase disappears (Figure 4c) and is replace with a 5-10 μm gap, which is consistent with the increased impedance due to contact lost shown in Figure 5.2c. It should be noted that the observed gap in Figure 5.4c is likely less prominent under application of stack pressure and enough contact is maintained in other areas of the interface (Figure 5.5) to maintain electrical contact.

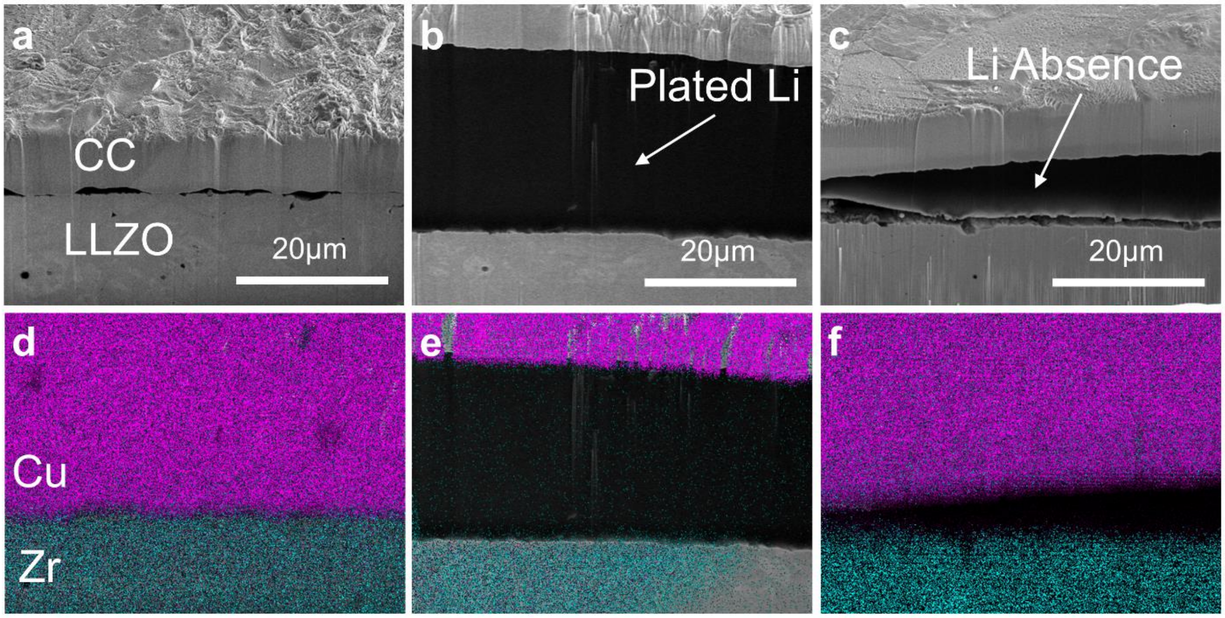

Figure 5.4: Cross-sectional SEM-FIB analysis of the LLZO and the current collector interface. SEM (a) as assembled, (b) after plating 5 mAh cm^{-2} of Li, and (c) after plating and then stripping of 5 mAh cm^{-2} of Li. Elemental maps for Cu and Zr at the interface (d) as assembled, (e) after plating, and (f) after plating and stripping. Metallic Li is observed under secondary electrons in between the Cu and LLZO layer in (b) but cannot be detected since the characteristic x-ray energy falls outside of the detection range of EDS.

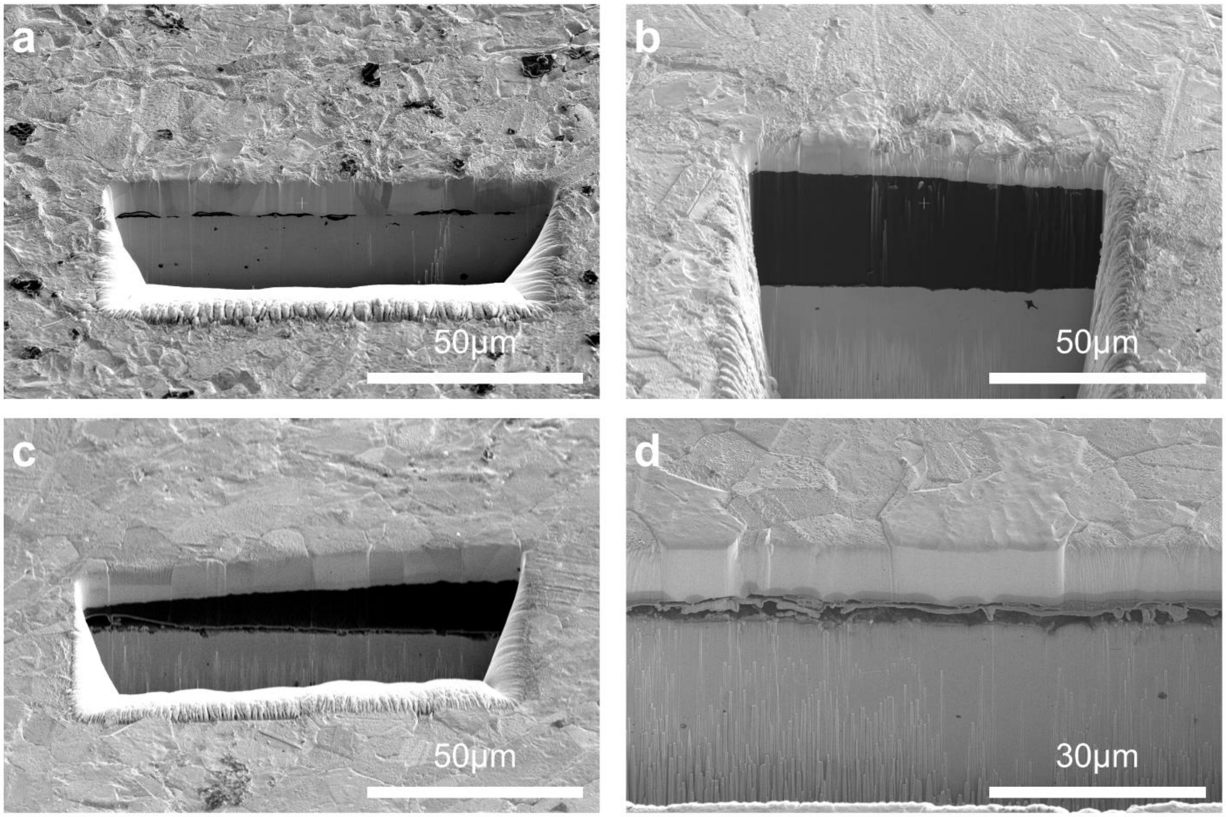

Figure 5.5: Low magnification SEM of FIB-milled Cross-Sections from Figure 5.4. (a) Cu current collector as laminated onto LLZO, (b) after 5 mAh cm^{-2} of Li is plated, and (c) after 5 mAh cm^{-2} of Li is plated and stripped. The intermediate Li layer in between the Cu and the LLZO in (b) more clearly shows textural features at lower magnifications which indicates the presence of an intermediate phase rather than empty space, despite the high color contrast. Not all regions of the interface after stripping 5 mAh cm^{-2} of the plated Li exhibit such a prominent separation between Cu and LLZO that is observed in (c). One such region of a less pronounced separation is shown in (d), which exhibits a smaller gap between Cu and LLZO but is still more pronounced than in (a) and shows a similar residue between Cu and LLZO that is also observed in (c).

The presence of metallic Li can also be confirmed visually after peeling the current collector off the surface after electroplating. *ex situ* SEM was conducted on the LLZO surface after removal of the current collector as a function of plated capacity. The morphology of the surface after deposition of 4, 30, 200, 620, 1000, and 1600 μAh cm^{-2}of Li is shown in Figure 5.6. It has been previously demonstrated that at these low interfacial resistances, strong adhesion between the Li metal and LLZO is expected[89]. Therefore, while the peeling of the current collector is expected to damage the Li metal itself (evidenced by the cup-cone fracture morphologies), the spatial distribution, the positions, and the dimensions of the plated Li are expected to be preserved. While it is difficult to identify Li growths after 4 μAh cm^{-2} (5 min) of plating, after 30 μAh cm^{-2} clear patches (~100 μm diameter) appear that cover ~15% of the LLZO surface. Smaller Li structures are also observed which may indicate nucleation sites that did not subsequently grow. After 200 μAh cm^{-2} of Li is plated, the Li patches are observed to both increase in number and grow laterally until they begin to coalesce into a relatively uniform film after ~1000 μAh cm^{-2}. After coalescence into a uniform layer, the Li seems to grow vertically rather than laterally which results in more height and topography of the Li film after plating 1.6 mAh cm^{-2}. Overall, the SEM images clearly suggest that within the first 30 μAh cm^{-2} (38 min) of plating, some but not all of the LLZO surface has Li deposition. It should also be noted that apparently pristine LLZO interface remains after ~12 h of plating (Figure 6d), indicating that some regions of the LLZO surface are more resistive (perhaps due to surface chemistry), some regions of the LLZO/CC interface have a higher work of adhesion and hence are harder to open, or the LLZO/CC interface could be opened at locations adjacent to Li deposits, forming gaps that cut off current flow until nearby Li is deformed or further plated in the planar direction. After 12 hours and ~50% coverage of Li, the average height of deposited Li would be~6 μm lending plausibility to gap formation (i.e., 6 μm is a substantial separation distance compared to the expected surface roughness of the LLZO/CC interface). On the other hand, the cells are under 4 MPa of pressure, which may cause Li to plastically flow into portions of the CC-LLZO interface as electrodeposition occurs.

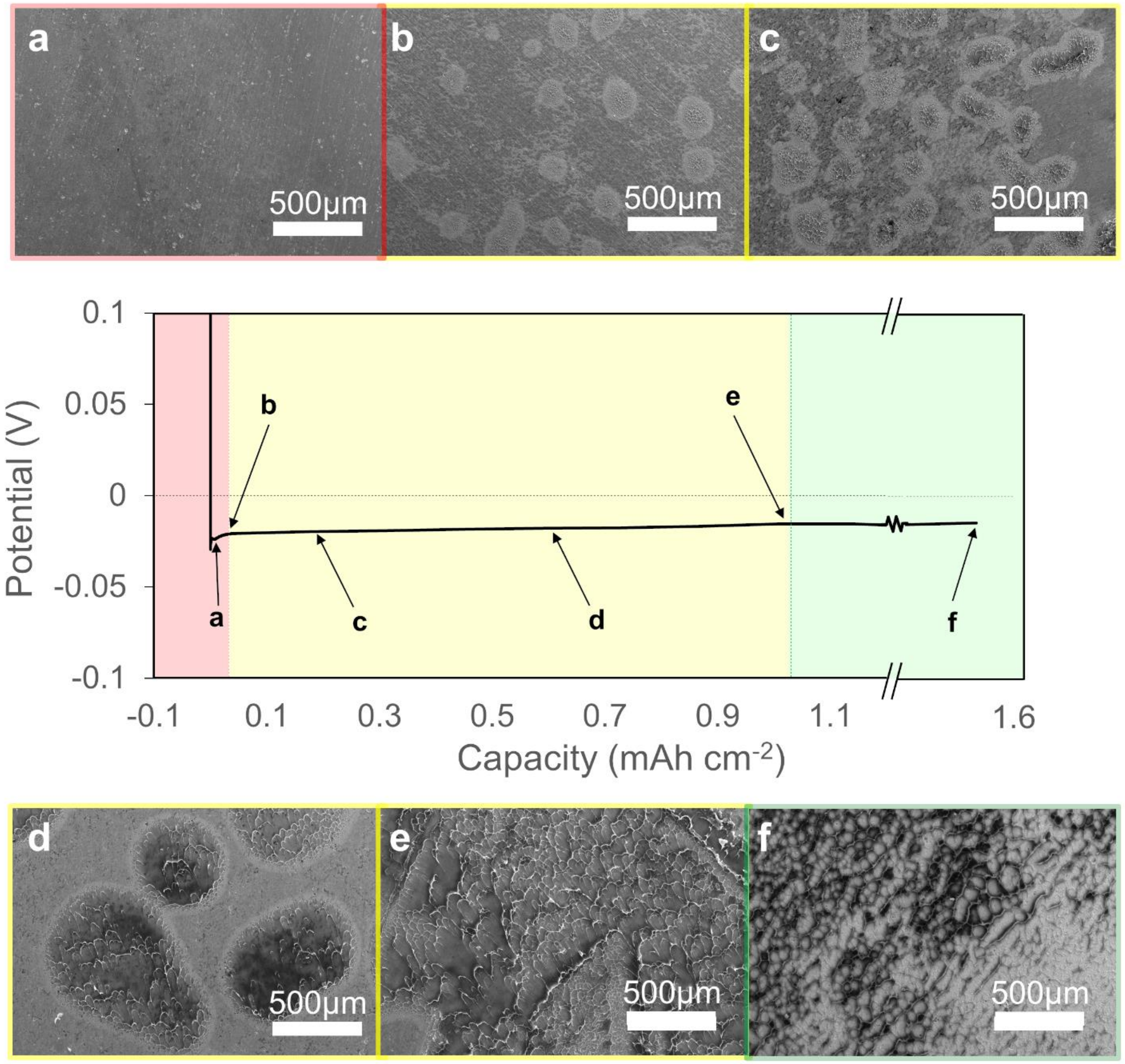

Figure 5.6: *ex situ* SEM of the LLZO surface after removal of the current collector. LLZO surface after plating (a) 4 µAh cm^{-2}, (b) 30 µAh cm^{-2}, (c) 200 µAh cm^{-2}, (d) 620 µAh cm^{-2}, (e) 1.0 mAh cm^{-2}and (f) 1.6 mAh cm^{-2} of Li. The SEM images are correlated to a typical potential profile upon plating, showing three distinct regimes: 1) Li nucleation, 2) lateral growth of the Li nuclei, and 3) coalescence of the nuclei and subsequent vertical growth of the coalesced Li film.

Figure 5.7 envisions how the nucleation and growth process may occur. Plating likely begins with small nucleates (Figure 5.7a), while subsequent growth may occur by vertical growth of Li columns (Figure 5.7c), plating at the nucleate sites with horizontal plastic flow of Li to open new CC/LLZO interface (Figure 5.7d, Li has a yield strength of <1 MPa and hence flows under relatively low stresses, although its plastic deformation under compression depends on boundary conditions[52]), or direct plating of Li into additional CC/LLZO interface (Figure 5.7e). Both Li nucleation and growth require the delamination of the CC-LLZO interface and the formation of new Li-LLZO and Li-CC interfaces. The work associated with this process (in J m^{-2}) can be estimated from the adhesion work (also in J m^{-2}) of the individual contacts:

$$W_{CC\cdot Li\cdot LLZO} = W_{adh,CC\cdot LLZO} - W_{adh,Li\cdot CC} - W_{adh\ Li\cdot LLZO} \tag{5.3}$$

This equation assumes that new Li-LLZO and Li-CC interfaces completely fill the opened CC-LLZO interface. Also note that the Li plating work and interfacial energies in equation (5.3) include all of the mechanisms that can contribute to the adhesion of two interfaces[120]. Peel tests were conducted to experimentally estimate the works of adhesion of the current collector on the LLZO, which is described in the experimental section (Figure 5.8). The experimental measurements of $W_{adh,CC\cdot LLZO}$ provide estimates on the order of 1-10 J m^{-2} (for Cu and Ni), which is higher than surface energy estimates, which only consider the bonding energy at atomically smooth interfaces[24]. Reducing this value may be of practical importance in optimizing anode-free cell manufacturing. To provide a quantitative framework for step (1) (the creation of the first Li nucleates) the critical radius (i.e., the radius at which continued growth is favored thermodynamically) for a spherical nucleate of Li can be determined using the Gibbs free energy of formation of the nucleate:

$$\Delta G_{total} = -\frac{4}{3}\pi r^3 \Delta G_{Li} + 4\pi r^2 W_{CC\cdot Li\cdot LLZO} \tag{5.4}$$

Here, $\Delta G_{Li}$is the energy associated with Li deposition, and $W_{CC\cdot Li\cdot LLZO}$ is the work associated with opening the CC-LLZO interface, as given by equation (5.3). Here, ΔG_{Li} is for the reaction $Li^+ + e^- \rightarrow Li$, and we can also use $\Delta G_{Li} = -F\eta_{nuc}$ where F is Faraday's constant and η_{nuc} is the Li nucleation overpotential. The critical radius – below which no Li should nucleate - can be determined by:

$$r_0 = -\frac{2W_{CC\cdot Li\cdot LLZO}\bar{V}_{Li}}{F\eta_{nuc}} \tag{5.5}$$

$\bar{V}_{Li}$ the molar volume of Li. Figure 5.7b illustrates the critical radius as a function of η_{nuc} for several values of $W_{CC\cdot Li\cdot LLZO}$. Here, the value of η_{nuc} can be thought of as the additional potential that needs to be supplied to do the work required to first open the CC-LLZO interface. As shown in Figure 5.7b, assuming a value of ~1 J m^{-2}, and assuming that both $W_{adh,Li\cdot CC}$ and $W_{adh,Li\cdot LLZO}$ are negligible, critical radii are in the micron range for several mV of overpotential. The assumption that $W_{adh,Li\cdot CC}$ and $W_{adh,Li\cdot LLZO}$ are negligible is justified if the adhesion mechanisms for the diffusion bonded interface (~1-10 J m^{-2}) are much stronger than the adhesion mechanisms for the new interfaces of CC and LLZO with Li metal (which, if similar to calculated surface energies, are <1 J m^{-2})[33]. In other words, 10 s of J m^{-2} of work to open the diffusion bonded CC/LLZO interface corresponds to several mV of potential driving force to create the first Li nucleates, and the potential profile at short times in Figure 5.1b may reflect the nucleation process.

During step (2) (the subsequent growth of Li nucleates), work is required to continue opening the CC-LLZO interface, with possible mechanisms for that opening shown in shown in Figure 5.7c-e. For any of these mechanisms, the overpotential required to open the CC-LLZO interface is given by:

$$\eta_{CC\cdot Li\cdot LLZO} = \left(W_{CC\cdot Li\cdot LLZO}\frac{dA}{dt}\right)/I \tag{5.6}$$

I (in A) is the applied current, and dA/dt (in m^2/s) is the rate of CC/LLZO interface opening. The SEM images in Figure 5.6 suggest the rate of opening of the CC/LLZO interface (i.e., dA/dt)) may be nonlinear, such than the overpotential for interface opening during Li growth varies with time. The overpotential described in equation (4) may also contribute to the potential profile seen in Figures 5.1 and 5.6. We also note that if the nucleate is subjected to an applied pressure, that would further increase the potential driving force required to drive the nucleation and growth process. An order of magnitude estimate for the additional potential is given by $\eta \approx \frac{\bar{V}_{Li}}{F} p$, where p is the pressure in the nucleate. An applied pressure of 4 MPa therefore results in an additional $\eta \approx 0.5$ mV. Future research can clarify which mechanisms shown in Figure 5.7c-e are most important, and how they depend on boundary conditions such as applied pressure and current density.

An obvious limitation of this analysis is that it neglects the nm-scale processes associated with Li plating, including at polycrystalline LLZO grains of various orientations and with surface roughness. The results shown in Figure 5.7 should therefore be considered as an initial framework for how the relatively high work of adhesion, measured in this study, may influence the overpotentials for nucleation and growth. It should also be emphasized that the observations made in the SEM analysis – that a small number (Figure 5.6 shows ~10 nucleates per mm^{-2}) of nucleates appear to grow large (Figure 5.6b shows a diameter of ~100 μm by 1 h), rather than many small nucleates forming and quickly merging – is a strong indication of surface heterogeneity. However, we acknowledge that although present experiments have not identified which surface heterogeneity(ies) (e.g., in $W_{CC \cdot Li \cdot LLZO}$, interfacial LLZO kinetics, CC surface properties, etc) are most important. The proposed model applies to the initial Li plating cycle into the pristine diffusion bonded CC-LLZO interface, subsequent stripping and plating cycles require further analysis.

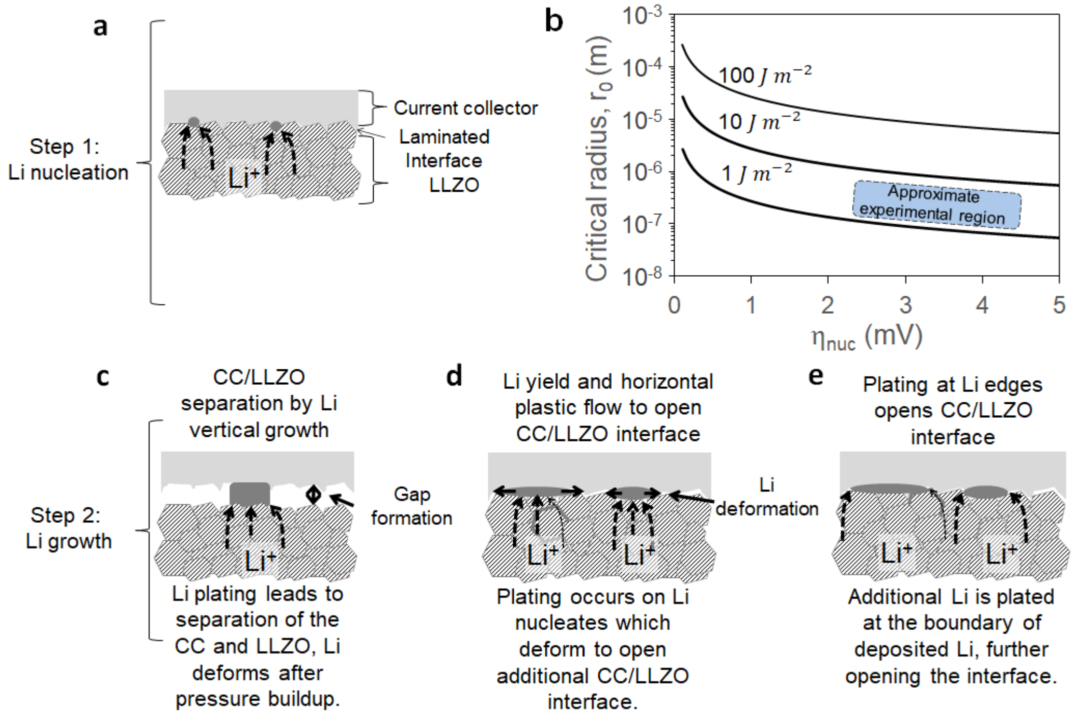

Figure 5.7: Schematic of nucleation and growth process. (a) shows the layers present and Li nucleates (treated as spherical in the nucleation model) and (b) shows the critical nucleate radius as a function of nucleation overpotential. c-e show three possible mechanisms for nucleate growth, including (c) deposition on the nucleate leading to vertical growth and separation of the adjacent CC/LLZO interface, (d) continued deposition at the nucleate center, with mechanical forces at the interfaces and Li's low yield strength leading to horizontal plastic flow of Li, or (e) deposition at the nucleate edges.

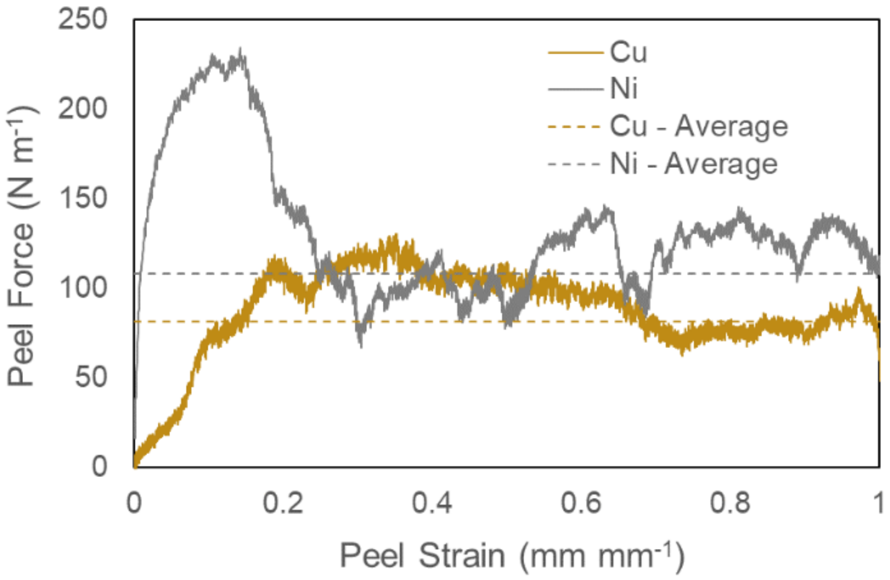

Figure 5.8: Peel Tests for Measuring Macro-scale Work of Adhesion. 90° Peel tests to measure the work of adhesion of the laminated current collectors on the LLZO surface. The dashed lines indicate the average peel force for each current collector type for three different samples each. The average peel force is measured from the average force over the steady-state region (~0.4 – 1.0 peel strains). The average work of adhesions for Cu and Ni are estimated to be within the range of 1-10 J m^{-2}.

Motoyama *et al.* has also measured and proposed one of the first models for Li plating into a CC/solid-electrolyte interface, modeling the potential evolution at the start of plating in a thin-film battery, with a LiPON solid electrolyte and a PLD or sputter deposited metal current collector with a thickness of 30 to 90 nm or 1 μm[112]. These authors could optically observe, for the thinner current collectors for which Li beneath them was easily visible, lithium nucleation and growth and, in some cases, fracture of the lithium through the current collector. They observed a voltage rise of ~30 mV (for the 90 nm current collector) to ~50 mV (for the 30 nm current collector), while for the 1 μm current collector the voltage rise was, as in our experiments, <10 mV. They developed a hoop stress model for pressure buildup in the lithium nucleates to account for the potential profile, assuming a fixed 0.2% strain in the region of current collector adjacent to the nucleate, and setting the hoop radius to fit the data. Their model does not account for work of adhesion or interfacial energies between the phases, including during the growth of lithium nucleates, and requires the interfaces to be in full contact as GPa-level pressures are generated within the Li nucleate. The mechanical properties are assumed to be those of the bulk metals, which may not be the case, especially for the <100 nm PLD-deposited metal films. In addition, their model does not address why Li nucleates form and grow with tens of mV of overpotential while substantial areas of the current collector receive no Li plating. In our view, this fact is clear evidence of the need to consider more closely spatial variations in interfacial resistance, and to identify the contributing mechanisms, for Li nucleation into a current collector / solid electrolyte interface.

5.1.3.3 Performance of an in situ plated Li metal anode

The results presented thus far have demonstrated the capability of electrochemically forming thick Li metal films at the interface of the LLZO electrolyte and current collector. To evaluate the performance of the *in situ* formed Li metal anode with a relevant model cathode, a Li-metal/LLZO/NCA all-solid-state cell was fabricated. In order to avoid the need for small quantities of liquid electrolyte to improve the NCA/LLZO interface charge transfer kinetics, an all-solid-state PEO/NCA composite cathode was used, since it has been demonstrated that the PEO/LLZO interface resistance can be reduced to relatively low values (<200 Ω cm^2 at room temperature)[121]. However, because the bulk conductivity of PEO-LiTFSI polymers is low at room temperature (~1×10^{-6} S cm^{-1}), the cell was operated at 60°C. After assembly of the Cu current collector, LLZO, and PEO/NCA cathode, the cell undergoes a single formation cycle, which plates the Li metal anode at 0.05 mA cm^{-2} from the Li contained within the NCA. Of the available 3 mAh cm^{-2} cathode capacity, 2.7 mAh cm^{-2} (~13.5 μm) was plated upon formation and used as the Li metal anode. Figure 5.10 shows the charge/discharge behavior, cycling at 60°C (±3°C) at a C/10 rate (0.27 mA cm^{-2}), following the formation cycle. Prior to full cell testing, the critical current density (CCD) was measured (Figure 5.9) in a symmetric cell at room temperature. It was observed that the CCD at room temperature of a 25 μm *in situ* formed Li anode (0.3 mA cm^{-2}) was notably lower than reported values using Li foil (~1 mA cm^{-2}), which may suggest the presence of length-scale-dependent phenomena that impact Li filament initiation.

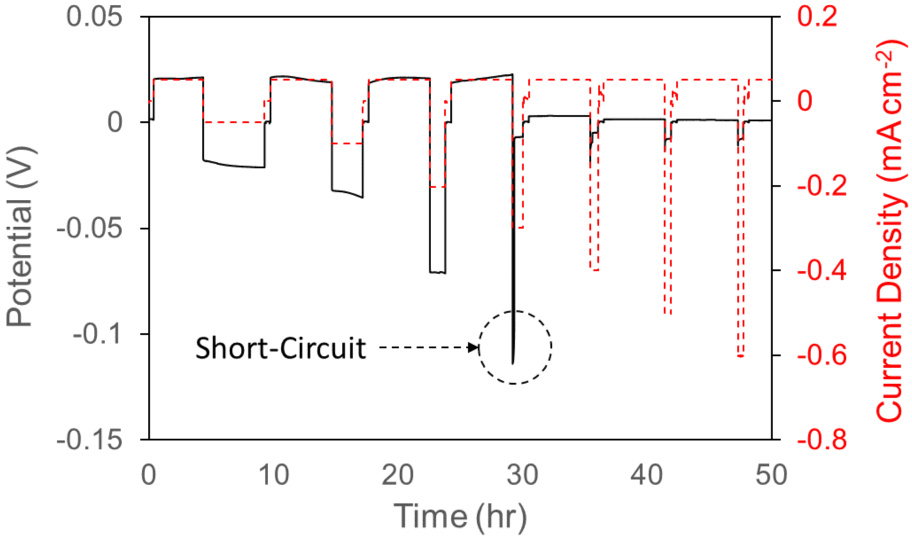

Figure 5.9: Critical Current Density Measurement of 25 μm *in situ* Plated Li

It is seen in Figure 5.10a the cell undergoes a typical potential response upon charging and discharging and achieves a capacity of 0.75 mAh cm^{-2} on the first cycle. Although some first-cycle capacity loss is expected for NCA following the formation cycle, it is believed that the lack of an optimized PEO-composite cathode prevents the majority of the capacity from being accessed at a C/10 rate. A cell was also cycled at 80°C at the same current density as the formation cycle (0.05 mA cm^{-2}), and it was shown that significantly higher capacities (~2.4 mAh cm^{-2}), closer to the capacity of the formation cycle, can be achieved (Figure 5.11). Figure 5.10b shows the capacity over 50 cycles along with the Coulombic efficiency. Coulombic efficiencies above 100% are observed which is not impossible in this case, since less Li is cycled (<0.8 mAh cm^{-2}) than what was originally plated (2.7 mAh cm^{-2}) and therefore for any given discharge cycle, there may be more accessible Li than what was previously plated upon charging. Moreover, because LLZO is stable against Li, the absence of side reactions should, in principle, enable 100% Coulombic efficiency; a paradigm shift in Li battery operation. Despite a few outlying cycles, the Coulombic efficiencies remain near 100% throughout the 50 cycles. Even with the high efficiencies, a ~25% capacity fade is observed after 50 cycles, which can be attributed to the increase in cell impedance. Figure 5.10c shows an increase in the total cell impedance from ~90 Ω cm^2 on the 1st cycle to ~200 Ω cm^2 on the 50th cycle. Since the change is isolated to low frequencies, the impedance growth is solely due to changes at an internal interface. Because the capacity of the *in situ* formed Li anode is known to be 2.7 mAh cm^{-2} based on the formation cycle, and less than 0.8 mAh cm^{-2} is being cycled, the anode/electrolyte interface is that of excess Li/LLZO, which was seen in the earlier results to be unchanging under these depths of discharges. Therefore, the cause is more likely related to cycling-induced degradation and worsening charge transfer kinetics of the PEO/LLZO or PEO/NCA interface, rather than degradation of the Li/LLZO interface. Although the oxidative stability of solid-polymer electrolytes is dependent on a number of factors like salt concentration, it is possible that degradation of the PEO above ~3.8-4.0 V may be the cause of the impedance growth and subsequent capacity fade observed in Figure 5.10 and Figure 5.11[13,122–126]. To confirm this, a Cu/LLZO/Li-foil cell was cycled under identical conditions and no increase in cell impedance nor capacity or Coulombic efficiency fade was observed (Figure 5.12). This strongly suggests that the observed capacity fade is limited by the cathode/catholyte interface rather than the *in situ* plated Li anode, further highlighting the need for continued development of stable, high-rate, and compatible composite cathodes.

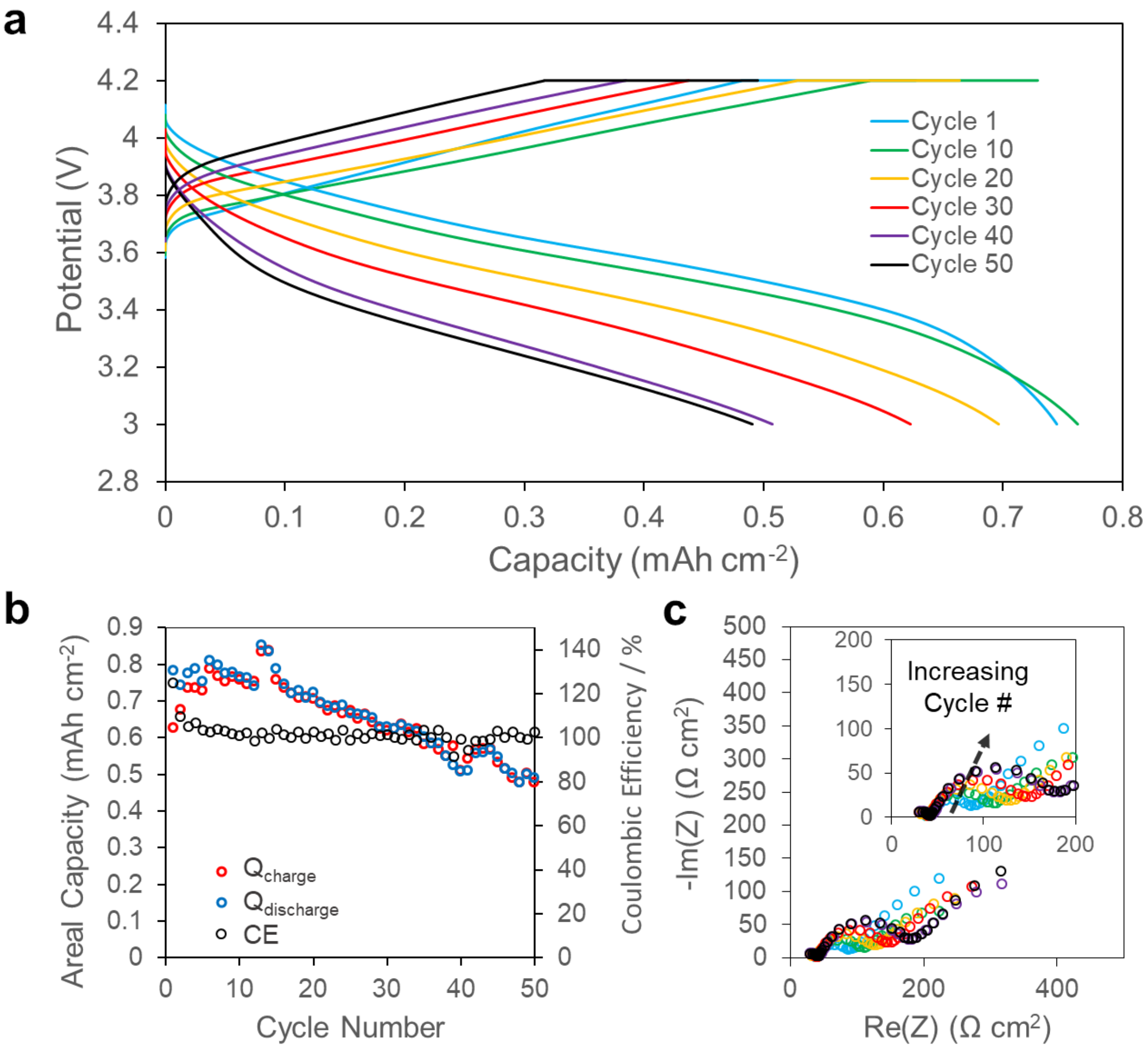

Figure 5.10: Cycling behavior of a Li metal battery composed of an NCA/PEO composite cathode, LLZO, and *in situ* plated Li metal anode cycling at 60°C. (a) Representative charge/discharge curves cycling at a C/10 rate. (b) The areal capacity and Coulombic efficiency as a function of cycle number. (c) The impedance spectra measured after every ten cycles.

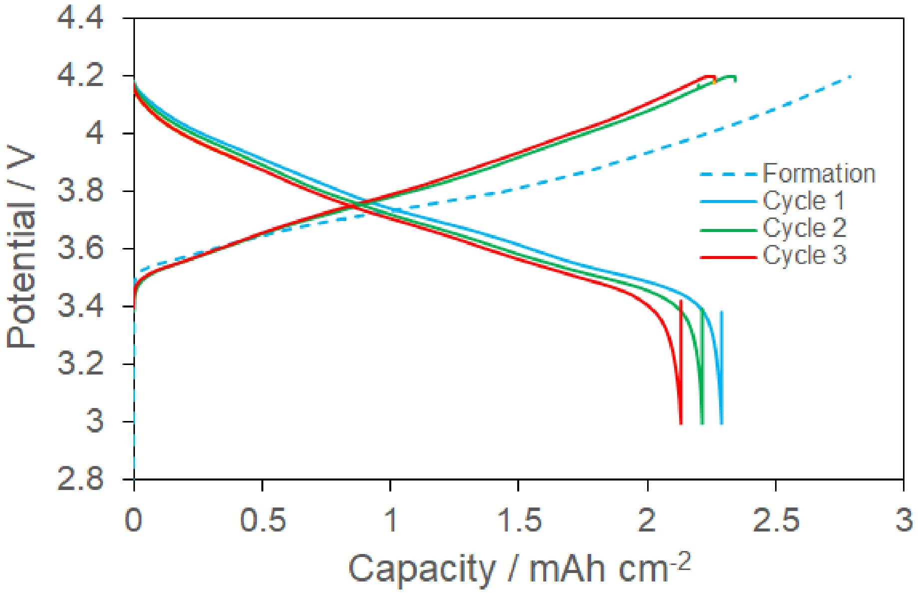

Figure 5.11: Cycling behavior of a Li metal battery composed of an NCA/PEO composite cathode, LLZO, and *in situ* plated Li metal anode cycling at 80°C.

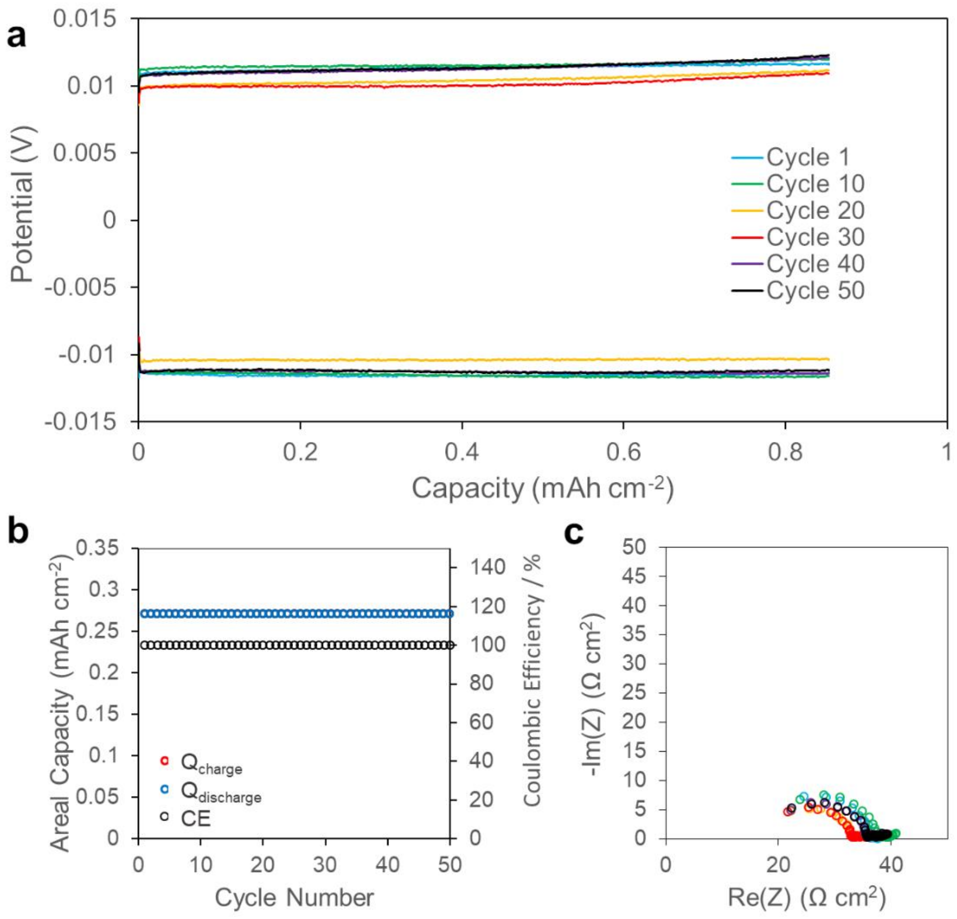

Figure 5.12: Cycling behavior of a Li metal battery composed of a Li metal foil, LLZO, and *in situ* plated Li metal anode cycling under identical conditions as in Figure 6. The *in situ* anode is formed with a capacity of 2.7 mAh cm^{-2} with 0.85 mAh cm^{-2} (corresponding to the maximum capacity value in Figure 6b) being cycled at 60°C . (a) Representative charge/discharge curves cycling at a C/10 rate. (b) The areal capacity and Coulombic efficiency as a function of cycle number. (c) The impedance spectra measured after every ten cycles.

5.1.4 Conclusion

"Li-free" manufacturing enabled through *in situ* plated Li metal anodes could dramatically impact the feasibility of solid-state batteries for vehicle electrification. The ability to electrochemically form the Li metal anode not only eliminates the processing costs and challenges of working with bulk or vapor deposited Li metal, but may also enable the usage of commercially available Li-ion cathode materials without the volumetric and gravimetric penalty of having pre-deposited Li. In this work, it has been demonstrated that significant capacities (5 mAh cm^{-2}) of Li metal can be both electrodeposited and depleted at the interface of LLZO and a current collector without any LLZO degradation, without the need for an interlayer, and with high efficiencies. Based on the morphology and distribution of plated Li as a function of plated capacity, a simple model based on interfacial forces was proposed to describe the nucleation and lateral growth of isolated Li regions into a coalesced uniform film. Finally, a prototypical all-solid-state battery was fabricated by *in situ* plating the Li from a PEO/NCA composite cathode, through the LLZO and onto a Cu current collector. The Li/LLZO/PEO-NCA cell was cycled for 50 cycles at a C/10 rate, exhibiting capacities of 0.8 mAh cm^{-2} upon the first few cycles and near 100% Coulombic efficiencies. Although capacity fade was observed after 50 cycles, the lack of efficiency fade suggests that the cell is limited by the composite cathode performance, providing further motivation for solid-state battery cathode development. The results presented here not only demonstrate the first “Li-free” solid-state battery based on garnet electrolytes, but also highlights the need for further investigation of how mechanics, electrochemistry, and spatial variations in interfacial properties affect Li electrodeposition at solid-solid interfaces.

Chapter 6 Conclusions and Future Work

6.1 Summary

Interfaces within a solid-state battery are a constantly changing landscape as the battery is charged and discharged. This leads to unique challenges for designing batteries with high energy densities, fast rate capabilities, and long lifetimes. In an effort to better understand these challenges, this dissertation investigates the coupled electrochemical and mechanical phenomena that occur at the interface between ceramic solid-state electrolytes and alkali metal anodes. This work revolves around two relevant model systems: Li metal anodes coupled with the $Li_7La_3Zr_2O_{12}$ (LLZO) electrolyte and Na metal anodes coupled with the Na-β”-alumina (NBA) electrolyte.

Using these two systems, two major phenomena that limit the power density and lifetime upon both charging and discharging of the solid-state battery were identified and investigated. First in Chapter 3, the widely known phenomenon of alkali metal penetration through the solid-electrolyte was investigated. Upon electroplating above a critical current density (CCD), it is widely observed that electroplated alkali metals, both Li and Na, can fracture and propagate through the solid-electrolyte and create an internal short-circuit. This effectively limits the charging rate of the battery. Using the CCD as a metric, the effects of temperature on unstable Li metal plating was explored by measuring the CCD at a variety of temperatures. It was demonstrated that the CCD of the Li/LLZO system increases exponentially with temperature, increasing from 0.9 mA cm^{-2} at room temperature to 6.7 mA cm^{-2} at 100°C. Based on comparisons of the temperature dependent transport properties of the LLZO and the temperature dependent self-diffusion rates in Li metal, it was hypothesized that similar to the unstable growth of metal dendrites in liquid electrolytes, a similar transport limitation results in the growth of metal filaments in solid electrolytes. In this case, the transport limitation exists as relatively slow transport of electroplated Li away from the Li/LLZO interface, resulting in the build-up of electrical "hot-spots" and/or localized regions of pressure resulting in Li filament penetration. To further investigate this phenomenon, the analogous mechanism of Na metal penetration through ceramic Na^+ conductors was also investigated. Owing to a newly developed method for decreasing the interface resistance of the Na/NBA interface by heat-treating, identical CCD measurements could then be conducted using the Na/NBA system. Similar to the Li/LLZO case, the CCD of the Na/NBA system showed an exponential increase with temperature, increasing from 12 mA cm^{-2} at room temperature to 19 mA cm^{-2} at 60°C. From the comparison of the two systems, a theoretical model was proposed to explain the origin of the CCD. By modeling the flow of electroplated metal out of a surface defect, a mechanical pressure within a surface defect can be calculated and related to the fracture toughness of the ceramic electrolyte. The proposed model showed good agreement with the experimental CCD values, while also highlighting the importance of electrolyte conductivity and fracture toughness, which also play a key role in filament initiation and propagation.

In Chapter 4, a relatively new phenomenon of void formation upon alkali metal stripping was identified. Using the Li/LLZO system, it was determined that at low stack pressures, significant polarization occurs when cycling at a constant current density. This dramatic polarization was demonstrated to be dependent on the current density, creating a coupling between cell resistance, current density, and stack pressure. By incorporating a reference electrode, this polarization was shown to be completely isolated to the Li stripping electrode. Because the polarization is coupled to both current density and stack pressure, it was proposed that the origin of this polarization is the formation of voids at the interface that reduce the electrode/electrolyte contact area and thus lead to increases in cell resistance. Conducting identical measurements with the Na/NBA system, it was observed that the Na/NBA system qualitatively exhibits the same behavior, although similar to the electroplating case in Chapter 3, the Na metal system can withstand higher current densities and lower stack pressures. This points to a similar mechanism which governs void formation, which is an imbalance between an incoming flux of alkali metal and the outgoing flux that is dissolving into the electrolyte. If the metal is dissolved faster than can be replenished by the stack pressure, then voids begin to form and contact is lost, thus creating the coupling between stack pressure, current density, and cell resistance. This work identifies void formation as a major limiting factor in the discharge rate of the solid-state battery but presents stack pressure as a potential method of mitigating this issue.

Finally, Chapter 5 looked to investigate the unique scenario of electrodeposition onto a blocking surface, using the Li/LLZO system. It was demonstrated that at low current densities, significant amounts of Li metal could be electrochemically interposed between the LLZO and a blocking electrode. Furthermore, the Li metal could be electrochemically stripped with high Coulombic efficiencies. By examining the Li morphology as a function of Li plated it was revealed that the nucleation of Li onto the blocking electrode does not occur by a uniform deposition process, but rather a nucleation and growth mechanism. To explain this behavior, a mathematical framework that correlates interfacial forces, electrochemistry, and nucleation kinetic parameters is proposed to corroborate the experimental observations. This relationship provides the foundation to better understand Li nucleation onto a blocking surface, which can enable “Li-free” manufacturing of solid-state batteries. By using a current collector as the blocking electrode, the results of this work demonstrate the feasibility of electrochemically forming thick (>25 μm) Li metal anodes onto a current collector in a “Li-free” configuration, which can be a novel and practical method of low-cost manufacturing of solid-state batteries near their theoretical energy density limits. To demonstrate this, this work provides the first prototype of a functional “Li-free” all solid-state battery using the LLZO electrolyte.

6.2 Future Directions

This dissertation has identified and explored various aspects of electrochemistry and mechanics at the interface between state-of-the-art ceramic electrolytes and alkali metal electrodes. However, in order to better assess the commercial viability of solid-state batteries in the current energy storage market, the behavior of these systems needs to be further evaluated using more realistic designs and under more realistic operating conditions. The following sections present possibilities for future directions based on the findings of this dissertation.

6.2.1 Modeling of Electrochemo-Mechanical Phenomena for Optimizing Battery Design

This dissertation discusses several relationships between battery performance and certain external variables. While these relationships were studied predominantly through experimental methods, computational models could be developed to more accurately describe these phenomena. Not only could these models be used to better understand the experimental results, but also provide a modular framework for guided optimization of certain battery design parameters. One particular example of this would be modeling of void nucleation under stripping currents. While the hemispherical void model presented in Chapter 4.2 presents a mathematically simple method of describing the relationship between stack pressure and stripping current, a computational model using finite element methods would be able to more accurately describe the stability of that interface. This would not only provide better estimates for the required stack pressure, but could also allow for a better understanding of the driving factors for void growth, given that initial conditions like interface roughness and initial void radii are significantly easier to control computationally than they are experimentally. Similarly, in the case of Li deposition onto a current collector, there are several variables that are extremely difficult to control experimentally that could be systematically studied using computational models. The distribution of Li nuclei and therefore the nucleation overpotential is likely dependent on plating current density, external temperature and pressure, and surface heterogeneities due to surface chemistry or interface contact. Thus, the development of a computational model to minimize the number of potential variables would greatly aid in further understanding this phenomenon and would provide guidelines for designing systematic sets of experiments to compliment the model. This type of model could be used to optimize the formation cycle of the "Li-free" battery for formation current density, temperature, stack pressure, and interface morphology.

6.2.2 Alkali Metal Stripping and Plating Behavior at the Thin Film Scale

Currently state-of-the-art oxide electrolytes manufactured on the laboratory scale are typically hundreds of microns to millimeters in thickness while typical alkali metal electrodes are cold-rolled foils, several tens to hundreds of microns thick. While this is tremendously helpful and convenient for studying these systems in the laboratory, practical solid-state batteries with energy densities comparable to Li-ion batteries will require both electrolytes and metal electrodes with thicknesses of ~10-50 µm. At these length scales, both the electrochemical and mechanical conditions at these internal interfaces may have distinct differences that affect the interface evolution and overall performance of the battery. For example, as illustrated in Figure

6.1, physical heterogeneities at the interface can easily induce bending moments and deflection of the thin film ceramic electrolyte, which can compromise the mechanical integrity. Upon electroplating these additional stresses in the electrolyte may greatly impact the effective fracture toughness and therefore the CCD upon plating. Likewise, the formation of voids at the interface may also greatly impact the stress distribution of the cell under stack pressure and introduce heterogeneities that could cause electrolyte deflection. Furthermore, as demonstrated in Chapter 5, the nucleation of the electrodeposited metal occurs via a nucleation and growth process rather than a uniform deposition, which suggests that inhomogeneities upon plating will be inevitable, especially at deep-discharge states, when the electrode layer is almost completely depleted. Therefore, while the mechanisms of alkali metal penetration upon electroplating and void formation upon metal stripping should manifest in similar ways, the mechanical boundary conditions are slightly different. These differences may lead to additional failure criteria that will need to be evaluated and accounted for. For these reasons, additional analysis of both alkali metal plating and stripping at the interfaces of thin film electrodes and electrolytes will be necessary. These analyses should investigate the thin film mechanics of the electrolyte under cycling conditions and how internal stresses in the electrolyte affect the mechanical integrity and electrochemical performance.

Additionally, continued work should focus on systematically studying the effects of surface heterogeneities on the metal plating and stripping reactions. Using scalable and cost-effective manufacturing conditions, it is very unlikely that heterogeneities can be completely eliminated at these interfaces, be it chemical, physical, or microstructural. Therefore, in order to better understand the behavior of realistic systems under realistic operating conditions, the effects of surface heterogeneities should be understood. Using a surface engineering approach, inhomogeneous electrode/electrolyte interfaces can be manufactured. Deposition processes can be used to introduce artificial surface contaminants (chemical heterogeneities), impression molds can be used to create metal electrodes that unevenly distribute stack pressure (physical heterogeneities), and micromachining like focused-ion beam or microbead patterning can be used to introduce artificial defects in the electrolyte (microstructural heterogeneities). By systematically studying how these heterogeneities affect the nucleation behavior of both plated metal and interface voids, rather than minimize the amount of heterogeneities themselves, rational design choices can be made to instead minimize the effects of heterogeneities. For example, the introduction of coatings on the electrode or electrolyte, control over external variables like temperature and pressure, and/or the usage of thin layers of excess electrode material.

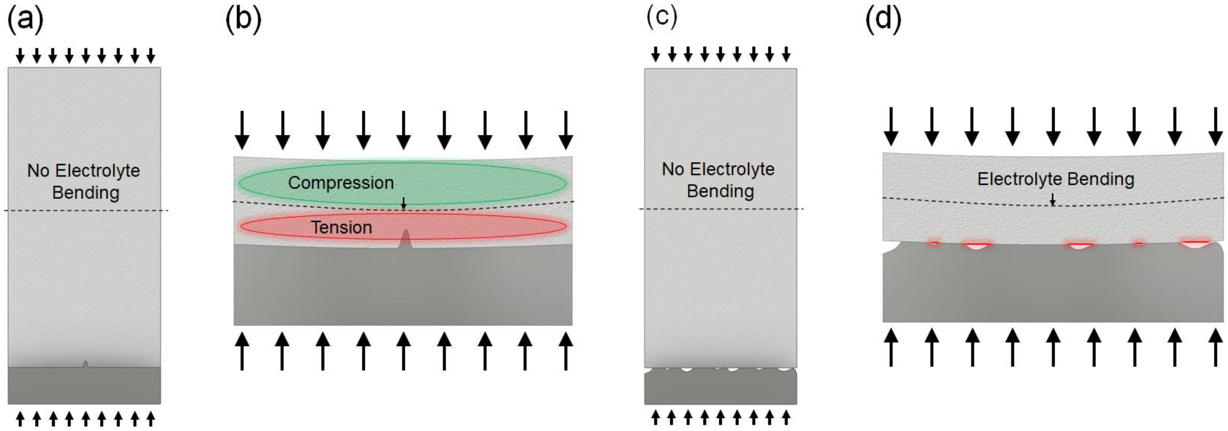

Figure 6.1: Schematic of the different mechanical environments at the interface between the alkali metal anode and a thick (~1 mm) ceramic electrolyte and a thin (≤100 µm) ceramic electrolyte. The effects of bending moments on defects in the ceramic electrolyte is shown for a) thick and b) thin membranes. The effects of voids in the alkali metal electrode is shown for c) thick and b) thin membranes.

6.2.3 Effects of Prolonged Cycling on Interface Morphology

Another requirement for solid-state batteries to compete against state-of-the-art Li-ion batteries is to have comparable lifetimes. While in principle, due to the chemical stability of the electrolyte compared to conventional liquid electrolytes, solid-state batteries can attain unprecedented efficiencies, several of the phenomenon discussed in this dissertation can either worsen the efficiency of the battery and/or can completely kill the battery early in its lifetime. Therefore, it will be necessary to further investigate how the electrode/electrolyte interfaces evolve over a number of cycles that more accurately represents the anticipated lifetime of a solid-state battery. Even under relatively benign cycling conditions, small inhomogeneities upon plating and stripping of the alkali metal electrode could significantly amplified over the course of several cycles, which can prematurely create an interface that is more susceptible to the failure mechanisms described in this dissertation. One particular example that may be important based on the results presented in Chapter 4.2.3.2, is the de-wetting and re-wetting behavior of the alkali metal upon stripping and plating, respectively. If the electrode does not completely re-wet the electrolyte surface, it may create an inactive area at the interface, which can continue to grow over the course of many cycles. Therefore, analysis of how these critical defects evolve using representative cycling parameters over a large number of cycles is crucial. As mentioned in Chapter 6.2.1, the effects and/or benefits of including an excess layer of electrode material should be examined in this analysis. If a detailed understanding of the morphological evolution of the interface can be correlated to the electrochemical behavior while cycling, precise diagnostic tools can be developed to identify early signs of degradation mechanisms without the need to cycle the battery for thousands of cycles.

6.2.4 Effects of Plating Current Density and Relaxation Times on Interface Evolution

Throughout this dissertation, interface phenomena have been studied under steady-state current conditions. However, in many realistic applications, the current draw is often not a steady constant current, but rather intermittent, inconsistent, and/or periodic in both the length of time of the applied current and the magnitude. This dissertation highlighted many time and current-dependent processes that occur at these interfaces like creep, void formation, or growth of electrodeposits. With an intermittent current profile, the balances between mechanical and electrochemical deformation will also change accordingly, which may have beneficial or detrimental effects on the interface evolution. One example can be presented in the case of electrodeposition upon a current collector as discussed in Chapter 5. If small amounts of Li metal are electrodeposited by a series of periodic constant current pulses separated by zero-current segments, the plated Li metal may have more time to deform and flatten before subsequent Li is deposited, as illustrated in Figure 6.2. Additionally, the magnitude of the current pulses may impact the nuclei density and the spatial distribution of critical nuclei. Therefore, it is likely that these types of current schemes may allow for higher degrees of uniformity of the plated Li films. Similarly, these types of current schemes may allow for higher CCDs to be achieved based on the relaxation times for the metal anode. Alternatively, upon alkali metal stripping as discussed in Chapter 4, if the stripping current is applied periodically with rest periods in between, the formation of voids may be impeded due to the additional time for the alkali metal to creep and maintain contact. The magnitude of the current density may also similarly affect the number density and distribution of the electrochemically formed voids. Therefore, understanding the electrochemical and mechanical responses of these systems under intermittent and/or transient current schemes may provide a better understanding of the expected battery performance under realistic operating conditions and may provide novel methods of designing the battery or developing operating criteria to improve battery performance. To better understand these implications, the effects of transient and/or intermittent conditions should be studied on the phenomena discussed in this dissertation. This should include how it may impact both the CCD and the "critical stack pressure" as well as how it may affect the morphological evolution of Li plated onto a current collector.

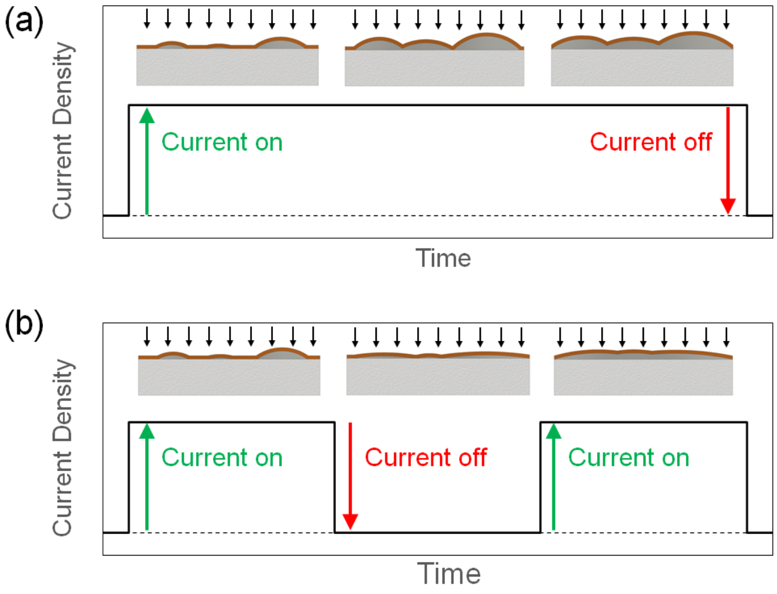

Figure 6.2: The possible evolution of electroplated Li metal under two different current schemes. The hypothetical interface evolution of Li plating onto a blocking electrode under a) a DC current and b) a pulsed current, allowing for relaxation of the plated Li

6.3 Conclusions

Solid-state batteries have the potential to deliver unprecedented energy and power densities, safety, and efficiencies and usher in a new generation of electrified technology. While a tremendous amount of progress has been made in the area of solid-state batteries in the past few years, many key challenges still lie ahead, waiting to be addressed. However, the development of solid-state batteries will inevitably be guided by our understanding of the materials science behind these systems. Motivated by these efforts, this dissertation has sought to better understand the coupled electrochemo-mechanical phenomena that occur at the electrode/electrolyte interface. It was shown that several aspects of battery performance are governed by both solid mechanics and solid-state electrochemistry at these interfaces. Understanding these mechanisms are critical for the development of strategies to mitigate performance limitations and to implement improved methods of battery operation and manufacturing. Ultimately, the success of solid-state batteries will hinge on the continued efforts to understand these fundamental mechanisms that govern their operation, failure, and construction. The knowledge gained through these efforts will undoubtedly form a *solid* foundation for the design and manufacturing of future energy storage technology.

Bibliography

[1] U.S. Energy Information Administration, **2019**, 3.

[2] U.S. Energy Information Administration, **2019**, 8.

[3] S. Sripad, V. Viswanathan, *ACS Energy Lett.* **2017**, *2*, 1669.

[4] D. Linden, T. B. Reddy, *Handbook of Batteries,* McGraw-Hill, New York, **2002**.

[5] R. Huggins, *Advanced Batteries - Materials Science Aspects | Robert Huggins | Springer,* **n.d.**

[6] Z. Zhang, Y. Shao, B. Lotsch, Y.-S. Hu, H. Li, J. Janek, L. F. Nazar, C.-W. Nan, J. Maier, M. Armand, L. Chen, *Energy Environ. Sci.* **2018**, *11*, 1945.

[7] J. R. Nair, L. Imholt, G. Brunklaus, M. Winter, *Electrochem. Soc. Interface* **2019**, *28,* 55.

[8] F. Zheng, M. Kotobuki, S. Song, M. O. Lai, L. Lu, *Journal of Power Sources* **2018**, *389*, 198.

[9] Y. Lu, L. Li, Q. Zhang, Z. Niu, J. Chen, *Joule* **2018**, *2*, 1747.

[10] Y. Zhu, X. He, Y. Mo, *J. Mater. Chem. A* **2016**, *4*, 3253.

[11] V. Lacivita, Y. Wang, S.-H. Bo, G. Ceder, *J. Mater. Chem. A* **2019**, *7*, 8144.

[12] L. Chen, S. Venkatram, C. Kim, R. Batra, A. Chandrasekaran, R. Ramprasad, *Chem. Mater.* **2019**, *31*, 4598.

[13] Y. Xia, T. Fujieda, K. Tatsumi, P. P. Prosini, T. Sakai, *Journal of Power Sources* **2001**, *92*, 234.

[14] A. J. Samson, K. Hofstetter, S. Bag, V. Thangadurai, *Energy Environ. Sci.* **2019**, 10.1039.C9EE01548E.

[15] M. Winter, B. Barnett, K. Xu, *Chem. Rev.* **2018**, *118*, 11433.

[16] J. T. S. Irvine, D. C. Sinclair, A. R. West, *Adv. Mater.* **1990**, *2*, 132.

[17] S. Kim, C. Jung, H. Kim, K. E. Thomas-Alyea, G. Yoon, B. Kim, M. E. Badding, Z. Song, J. Chang, J. Kim, D. Im, K. Kang, *Advanced Energy Materials* **n.d.**, *n/a*, 1903993.

[18] T. Krauskopf, R. Dippel, H. Hartmann, K. Peppler, B. Mogwitz, F. H. Richter, W. G. Zeier, J. Janek, *Joule* **2019**, S2542435119303010.

[19] E. Kazyak, R. Garcia-Mendez, W. S. LePage, A. Sharafi, A. L. Davis, A. J. Sanchez, K.-H. Chen, C. Haslam, J. Sakamoto, N. P. Dasgupta, *Matter* **2020**, S2590238520300709.

[20] E. J. Cheng, A. Sharafi, J. Sakamoto, *Electrochimica Acta* **2017**, *223*, 85.

[21] Y. Ren, Y. Shen, Y. Lin, C.-W. Nan, *Electrochemistry Communications* **2015**, *57*, 27.

[22] F. Shen, M. B. Dixit, X. Xiao, K. B. Hatzell, *ACS Energy Lett.* **2018**, *3*, 1056.

[23] L. Porz, T. Swamy, B. W. Sheldon, D. Rettenwander, T. Frömling, H. L. Thaman, S. Berendts, R. Uecker, W. C. Carter, Y.-M. Chiang, *Advanced Energy Materials* **2017**, *7*, 1701003.

[24] A. Gupta, E. Kazyak, N. Craig, J. Christensen, N. P. Dasgupta, J. Sakamoto, *Journal of The Electrochemical Society* **2018**, *165*, A2801.

[25] J. A. Maslyn, L. Frenck, W. S. Loo, D. Y. Parkinson, N. P. Balsara, *ACS Appl. Energy Mater.* **2019**, *2*, 8197.

[26] L. Frenck, J. A. Maslyn, W. S. Loo, D. Y. Parkinson, N. P. Balsara, *ACS Appl. Mater. Interfaces* **2019**, *11*, 47878.

[27] A. Sharafi, H. M. Meyer, J. Nanda, J. Wolfenstine, J. Sakamoto, *Journal of Power Sources* **2016**, *302*, 135.

[28] R. Inada, S. Yasuda, H. Hosokawa, M. Saito, T. Tojo, Y. Sakurai, *Batteries* **2018**, *4*, 26.

[29] M. Wang, J. B. Wolfenstine, J. Sakamoto, *Electrochimica Acta* **2019**, *296*, 842.

[30] J. Kasemchainan, S. Zekoll, D. Spencer Jolly, Z. Ning, G. O. Hartley, J. Marrow, P. G. Bruce, *Nat. Mater.* **2019**, *18*, 1105.

[31] D. Spencer Jolly, Z. Ning, J. E. Darnbrough, J. Kasemchainan, G. O. Hartley, P. Adamson, D. Armstrong, J. Marrow, P. G. Bruce, *ACS Appl. Mater. Interfaces* **2019**, acsami.9b17786.

[32] A. Sharafi, C. G. Haslam, R. D. Kerns, J. Wolfenstine, J. Sakamoto, *J. Mater. Chem. A* **2017**, *5*, 21491.

[33] A. Sharafi, E. Kazyak, A. L. Davis, S. Yu, T. Thompson, D. J. Siegel, N. P. Dasgupta, J. Sakamoto, *Chemistry of Materials* **2017**, DOI 10.1021/acs.chemmater.7b03002.

[34] T. Swamy, R. Park, B. W. Sheldon, D. Rettenwander, L. Porz, S. Berendts, R. Uecker, W. C. Carter, Y.-M. Chiang, *arXiv:1808.02105 [cond-mat]* **2018**.

[35] C.-L. Tsai, V. Roddatis, C. V. Chandran, Q. Ma, S. Uhlenbruck, M. Bram, P. Heitjans, O. Guillon, *ACS Appl Mater Interfaces* **2016**, *8*, 10617.

[36] R. H. Basappa, T. Ito, H. Yamada, *Journal of The Electrochemical Society* **2017**, *164*, A666.

[37] M. Bay, M. Wang, R. Grissa, M. V. F. Heinz, J. Sakamoto, C. Battaglia, *Adv. Energy Mater.* **2020**, *10*, 1902899.

[38] J.-M. Tarascon, M. Armand, *Nature* **2001**, *414*, 359.

[39] J. B. Goodenough, Y. Kim, *Chemistry of Materials* **2010**, *22*, 587.

[40] C. Monroe, J. Newman, *Journal of The Electrochemical Society* **2005**, *152*, A396.

[41] L. Cheng, W. Chen, M. Kunz, K. Persson, N. Tamura, G. Chen, M. Doeff, *ACS Applied Materials & Interfaces* **2015**, *7*, 2073.

[42] N. J. Taylor, S. Stangeland-Molo, C. G. Haslam, A. Sharafi, T. Thompson, M. Wang, R. Garcia-Mendez, J. Sakamoto, *Journal of Power Sources* **2018**, *396*, 314.

[43] P. Albertus, **2016**.

[44] R. A. Huggins, *Ionics* **2002**, *8*, 300.

[45] H. Koshikawa, S. Matsuda, K. Kamiya, M. Miyayama, Y. Kubo, K. Uosaki, K. Hashimoto, S. Nakanishi, *Journal of Power Sources* **2018**, *376*, 147.

[46] B. Xu, W. Li, H. Duan, H. Wang, Y. Guo, H. Li, H. Liu, *Journal of Power Sources* **2017**, *354*, 68.

[47] E. G. Herbert, S. A. Hackney, V. Thole, N. J. Dudney, P. S. Phani, *Journal of Materials Research* **2018**, *33*, 1347.

[48] T. A. Witten, L. M. Sander, *Phys. Rev. Lett.* **1981**, *47*, 1400.

[49] J. S. Langer, *Rev. Mod. Phys.* **1980**, *52*, 1.

[50] T. R. Jow, C. C. Liang, **n.d.**, 4.

[51] A. Lodding, J. N. Mundy, A. Ott, *phys. stat. sol. (b)* **1970**, *38*, 559.

[52] A. Masias, N. Felten, R. Garcia-Mendez, J. Wolfenstine, J. Sakamoto, *Journal of Materials Science* **2019**, *54*, 2585.

[53] N. H. Nachtrieb, J. A. Weil, E. Catalano, A. W. Lawson, *The Journal of Chemical Physics* **1952**, *20*, 1189.

[54] A. Ott, A. Nordén-Ott, *Journal of Applied Physics* **1971**, *42*, 3745.

[55] M. Kleitz, J. Dupuy, Eds. , *Electrode Processes in Solid State Ionics: Theory and Application to Energy Conversion and Storage Proceedings of the NATO Advanced Study Institute Held at Ajaccio (Corsica), 28 August-9 September 1975*, Springer Netherlands, **1976**.

[56] R. 0. Ansell, *Journal of Materials Science* **1986**, *21*, 365.

[57] L. C. De Jonghe, L. Feldman, A. Beuchele, *J Mater Sci* **1981**, *16*, 780.

[58] D. Lin, Y. Liu, Y. Cui, *Nature Nanotechnology; London* **2017**, *12*, 194.

[59] R. Murugan, V. Thangadurai, W. Weppner, *Angewandte Chemie International Edition* **2007**, *46*, 7778.

[60] V. Thangadurai, S. Narayanan, D. Pinzaru, *Chem. Soc. Rev.* **2014**, *43*, 4714.

[61] W. Luo, Y. Gong, Y. Zhu, Y. Li, Y. Yao, Y. Zhang, K. (Kelvin) Fu, G. Pastel, C.-F. Lin, Y. Mo, E. D. Wachsman, L. Hu, *Advanced Materials* **2017**, *29*, 1606042.

[62] T. Krauskopf, H. Hartmann, W. G. Zeier, J. Janek, *ACS Applied Materials & Interfaces* **2019**, acsami.9b02537.

[63] M. J. Wang, R. Choudhury, J. Sakamoto, *Joule* **2019**, *3*, 2165.

[64] P. Albertus, S. Babinec, S. Litzelman, A. Newman, *Nature Energy* **2018**, *3*, 16.

[65] C.-H. Dustmann, *Journal of Power Sources* **2004**, *127*, 85.

[66] J. L. Sudworth, *Journal of Power Sources* **1984**, *11*, 143.

[67] J. L. Sudworth, *Journal of Power Sources* **2001**, *100*, 149.

[68] M.-C. Bay, M. V. F. Heinz, R. Figi, C. Schreiner, D. Basso, N. Zanon, U. F. Vogt, C. Battaglia, *ACS Appl. Energy Mater.* **2019**, *2*, 687.

[69] J. Zähr, S. Oswald, M. Türpe, H. J. Ullrich, U. Füssel, *Vacuum* **2012**, *86*, 1216.

[70] S. Hüfner, S. Schmidt, F. Reinert, *Nuclear Instruments and Methods in Physics Research Section A: Accelerators, Spectrometers, Detectors and Associated Equipment* **2005**, *547*, 8.

[71] L. Viswanathan, A. V. Virkar, *J Mater Sci* **1982**, *17*, 753.

[72] F. Han, A. S. Westover, J. Yue, X. Fan, F. Wang, M. Chi, D. N. Leonard, N. J. Dudney, H. Wang, C. Wang, *Nature Energy* **2019**, *4*, 187.

[73] M. Fritz, M. R. Barbosa, G. Staikov, W. J. Lorenz, M. Steinbrück, R. Knödler, *Solid State Ionics* **1993**, *62*, 273.

[74] R. Furuya, N. Tachikawa, K. Yoshii, Y. Katayama, T. Miura, *J. Electrochem. Soc.* **2015**, *162*, H634.

[75] J. B. Bates, N. J. Dudney, B. Neudecker, A. Ueda, C. D. Evans, *Solid State Ionics* **2000**, *135*, 33.

[76] W. S. LePage, Y. Chen, E. Kazyak, K.-H. Chen, A. J. Sanchez, A. Poli, E. M. Arruda, M. D. Thouless, N. P. Dasgupta, *Journal of The Electrochemical Society* **2019**, *166*, A89.

[77] L. Barroso-Luque, Q. Tu, G. Ceder, *J. Electrochem. Soc.* **2020**, *167*, 020534.

[78] R. D. Armstrong, T. Dickinson, J. Turner, *Electrochimica Acta* **1974**, *19*, 187.

[79] G. Han, B. Kinzer, R. Garcia-Mendez, H. Choe, J. Wolfenstine, J. Sakamoto, *Journal of the European Ceramic Society* **2019**, S0955221919308982.

[80] M.-C. Bay, M. V. F. Heinz, C. Linte, A. German, G. Blugan, C. Battaglia, U. F. Vogt, *Materials Today Communications* **2020**, 101118.

[81] C. D. Fincher, D. Ojeda, Y. Zhang, G. M. Pharr, M. Pharr, *Acta Materialia* **2019**, S1359645419308754.

[82] C. D. Fincher, Y. Zhang, G. M. Pharr, M. Pharr, *ACS Appl. Energy Mater.* **2020**, acsaem.9b02225.

[83] M. J. Wang, J.-Y. Chang, J. B. Wolfenstine, J. Sakamoto, *Materialia* **2020**, *12*, 100792.

[84] X. Lu, G. Xia, J. P. Lemmon, Z. Yang, *Journal of Power Sources* **2010**, *195*, 2431.

[85] R. Choudhury, M. Wang, J. Sakamoto, *submitted* **n.d.**

[86] J. Janek, S. Majoni, *Berichte der Bunsengesellschaft für physikalische Chemie* **1995**, *99*, 14.

[87] J. Yue, M. Yan, Y.-X. Yin, Y.-G. Guo, *Advanced Functional Materials* **2018**, *28*, 1707533.

[88] X. Fan, X. Ji, F. Han, J. Yue, J. Chen, L. Chen, T. Deng, J. Jiang, C. Wang, *Science Advances* **2018**, *4*, eaau9245.

[89] M. Wang, J. Sakamoto, *Journal of Power Sources* **2018**, *377*, 7.

[90] A. Sharafi, S. Yu, M. Naguib, M. Lee, C. Ma, H. M. Meyer, J. Nanda, M. Chi, D. J. Siegel, J. Sakamoto, *J. Mater. Chem. A* **2017**, *5*, 13475.

[91] J. Janek, *Solid State Ionics* **2000**, *131*, 129.

[92] A. Schröder, J. Fleig, D. Gryaznov, J. Maier, W. Sitte, *The Journal of Physical Chemistry B* **2006**, *110*, 12274.

[93] K. Yan, Z. Lu, H.-W. Lee, F. Xiong, P.-C. Hsu, Y. Li, J. Zhao, S. Chu, Y. Cui, *Nature Energy* **2016**, *1*, 16010.

[94] R. Garcia-Mendez, J. Sakamoto, **n.d.**

[95] W. Manalastas, J. Rikarte, R. J. Chater, R. Brugge, A. Aguadero, L. Buannic, A. Llordés, F. Aguesse, J. Kilner, *Journal of Power Sources* **2019**, *412*, 287.

[96] K. (Kelvin) Fu, Y. Gong, B. Liu, Y. Zhu, S. Xu, Y. Yao, W. Luo, C. Wang, S. D. Lacey, J. Dai, Y. Chen, Y. Mo, E. Wachsman, L. Hu, *Science Advances* **2017**, *3*, e1601659.

[97] J. Cannarella, C. B. Arnold, *Journal of Power Sources* **2014**, *245*, 745.

[98] P. Bonnick, J. R. Dahn, *J. Electrochem. Soc.* **2012**, *159*, A981.

[99] X. Zhang, Q. J. Wang, K. L. Harrison, S. A. Roberts, S. J. Harris, *Cell Reports Physical Science* **2020**, 100012.

[100] T. Krauskopf, B. Mogwitz, C. Rosenbach, W. G. Zeier, J. Janek, *Advanced Energy Materials* **n.d.**, *0*, 1902568.

[101] J. Janek, W. G. Zeier, *Nat Energy* **2016**, *1*, 16141.

[102] R. Schmuch, R. Wagner, G. Hörpel, T. Placke, M. Winter, *Nat Energy* **2018**, *3*, 267.

[103] A. Manthiram, X. Yu, S. Wang, *Nat Rev Mater* **2017**, *2*, 16103.

[104] J. Becking, A. Gröbmeyer, M. Kolek, U. Rodehorst, S. Schulze, M. Winter, P. Bieker, M. C. Stan, *Advanced Materials Interfaces* **2017**, *4*, 1700166.

[105] R. Weber, M. Genovese, A. J. Louli, S. Hames, C. Martin, I. G. Hill, J. R. Dahn, *Nat Energy* **2019**, *4*, 683.

[106] A. A. Assegie, J.-H. Cheng, L.-M. Kuo, W.-N. Su, B.-J. Hwang, *Nanoscale* **2018**, *10*, 6125.

[107] A. P. Cohn, N. Muralidharan, R. Carter, K. Share, C. L. Pint, *Nano Lett.* **2017**, *17*, 1296.

[108] J. Qian, B. D. Adams, J. Zheng, W. Xu, W. A. Henderson, J. Wang, M. E. Bowden, S. Xu, J. Hu, J.-G. Zhang, *Advanced Functional Materials* **2016**, *26*, 7094.

[109] W. Chang, J. H. Park, D. A. Steingart, *Nano Lett.* **2018**, *18*, 7066.

[110] J.-J. Woo, V. A. Maroni, G. Liu, J. T. Vaughey, D. J. Gosztola, K. Amine, Z. Zhang, *J. Electrochem. Soc.* **2014**, *161*, A827.

[111] B. J. Neudecker, N. J. Dudney, J. B. Bates, *J. Electrochem. Soc.* **2000**, *147*, 517.

[112] M. Motoyama, M. Ejiri, Y. Iriyama, *Journal of The Electrochemical Society* **2015**, *162*, A7067.

[113] M. Motoyama, M. Ejiri, Y. Iriyama, *Electrochemistry* **2014**, *82*, 364.

[114] Y.-G. Lee, S. Fujiki, C. Jung, N. Suzuki, N. Yashiro, R. Omoda, D.-S. Ko, T. Shiratsuchi, T. Sugimoto, S. Ryu, J. H. Ku, T. Watanabe, Y. Park, Y. Aihara, D. Im, I. T. Han, *Nat Energy* **2020**, DOI 10.1038/s41560-020-0575-z.

[115] L. Cheng, M. Liu, A. Mehta, H. Xin, F. Lin, K. Persson, G. Chen, E. J. Crumlin, M. Doeff, *ACS Appl. Energy Mater.* **2018**, *1*, 7244.

[116] Y. Wei, J. W. Hutchinson, in *Recent Advances in Fracture Mechanics* (Eds.: W.G. Knauss, R.A. Schapery), Springer Netherlands, Dordrecht, **1998**, pp. 315–333.

[117] J. Kim, K. S. Kim, Y. H. Kim, *Journal of Adhesion Science and Technology* **1989**, *3*, 175.

[118] E. Simlissi, M. Martiny, S. Mercier, S. Bahi, L. Bodin, *Int J Fract* **2019**, *220*, 1.

[119] N. Aravas, K.-S. Kim, M. J. Loukis, *Materials Science and Engineering: A* **1989**, *107*, 159.

[120] J. N. Israelachvili, *Intermolecular and Surface Forces*, Elsevier, Academic Press, Amsterdam, **2011**.

[121] A. Gupta, J. Sakamoto, *Electrochem. Soc. Interface* **2019**, *28*, 63.

[122] S. Seki, Y. Kobayashi, H. Miyashiro, A. Yamanaka, Y. Mita, T. Iwahori, *Journal of Power Sources* **2005**, *146*, 741.

[123] Q. Yang, J. Huang, Y. Li, Y. Wang, J. Qiu, J. Zhang, H. Yu, X. Yu, H. Li, L. Chen, *Journal of Power Sources* **2018**, *388*, 65.

[124] H. Cheng, C. Zhu, B. Huang, M. Lu, Y. Yang, *Electrochimica Acta* **2007**, *52*, 5789.

[125] Y. H. Kim, G. Cheruvally, J. W. Choi, J. H. Ahn, K. W. Kim, H. J. Ahn, D. S. Choi, C. E. Song, *Macromolecular Symposia* **2007**, *249–250*, 183.

[126] L. Chen, Y. Li, S.-P. Li, L.-Z. Fan, C.-W. Nan, J. B. Goodenough, *Nano Energy* **2018**, *46*, 176.